Scintillating Fiber Detector for the Mu3e Experiment

Dissertation

zur

Erlangung der naturwissenschaftlichen Doktorwürde
(Dr. sc. nat.)

vorgelegt der

Mathematisch-naturwissenschaftlichen Fakultät

der

Universität Zürich

von

Roman Gredig

von

Schwändi GL und Safien GR

Promotionskomitee
Prof. Dr. Ulrich Straumann (Vorsitz)
Prof. Dr. Gino Isidori
Dr. Peter Robmann
Dr. Olaf Steinkamp

Zürich, 2016

ABSTRACT

Mu3e is a proposed experiment to be built at the Paul Scherrer Institute searching for the charged lepton flavor violating decay $\mu^+ \to e^+e^-e^+$ with a sensitivity of $\mathcal{B} < 10^{-16}$, four orders of magnitudes lower than its predecessor SINDRUM. The experiment is built in a modular principle consisting of silicon pixel sensors for the vertex and momentum measurement and of scintillator fibers and tiles that deliver accurate time information.

This thesis presents a detailed study of a scintillator fiber detector playing a crucial role in the background suppression. A dedicated simulation of the fiber light yield and of the temporal distribution of the photons generated by the scintillation light is developed and integrated to simulation that covers the whole experiment. The simulation evaluates the light yield of single 250 µm thick fibers. The performance of 16 mm wide module consisting of several layers of glued fibers were also simulated. First prototypes of fibers that are built in the same way as they are intended to be used in the experiment. These prototypes are exposed to electrons from a ^{90}Sr source and from a testbeam at the Paul Scherrer Institute.

A data acquisition system using silicon photomultipliers and custom made signal amplifiers has been developed focusing on very high light sensitivity and a time resolution below 1 ns. With this setup detailed studies of the light yield, optical crosstalk, efficiencies and the time resolution have been performed. The results show a good agreement with the simulation and discuss the feasibility to build of building such a detector for the Mu3e experiment.

ZUSAMMENFASSUNG

Mu3e ist ein geplantes Experiment, welches am Paul Scherrer Institut nach dem Leptonflavor verletzenden Zerfall $\mu^+ \rightarrow e^+e^-e^+$ sucht. Die geplante Sensitivität soll den Zerfall bei einem Branching ratio von $\mathcal{B} < 10^{-16}$ entdecken können. Somit wäre dieses Experiment vier Grössenordungen empfindlicher als dessen Vorgänger, das SINDRUM Experiment. Geplant ist ist ein modularer Aufbau von verschiedenen Sensoren wie Silizium Pixelsensoren, welche den Vertex und Impuls messen sollen und szintillierenden Fibern und Kacheln, welche zusätzlich sehr genaue Zeitinformationen liefern sollen.

In dieser Arbeit wird eine detaillierte Studie der szintillierenden Fibern vorgestellt, welche eine wichtige Rolle spielen bei der Unterdrückung des Untergrundes. Eine eigene Simulation der Lichtausbeute der Fibern, sowie der zeitlichen Verteilung der Photonen, welche in den Fibern entstehen, wurde entwickelt. Die Resultate wurden in eine zweite Simulation, welche den ganzen Detektor simuliert, integriert. Einzelne Fibern mit einer Dicke von 250 µm wurden evaluiert, sowie die Performance von Fibermodulen, welche aus zusammengeklebten Fibern bestehen. Diese Module beinhalten mehreren Ebenen von Fibern und erreichen eine Breite von 16 mm. Prototypen von solchen Modulen, so wie sie im Experiment verbaut werden sollen, wurden entwickelt. Diese Module wurden mit Elektronen von sowohl einer ^{90}Sr-Quelle als auch aus einem Teststrahl am Paul Scherrer Institut bestrahlt.

Für die Vermessung der Fibern wurden ein Messsystem entwickelt, welches das Licht mittels Silizium Photonenvervielfachern aufzeichnet. Dafür wurde ein eigens für dieses Experiment optimierter elektrischer Signalverstärker entwickelt und getestet. Das Messsystem wurde mit dem Ziel entwickelt, möglichst lichtempfindlich zu sein und dabei eine Zeitauflösung besser als eine Nanosekunde zu erzielen. Die Fibermodule und das Messsystem zusammen wurden verwendet um die Fibermodule zu vermessen. Die Fibern wurden auf Lichtausbeute, optisches Übersprechen, Effizienz und Zeitauflösung getestet. Es zeigte sich, dass die Resultate gut mit der Simulation übereinstimmen und die Tauglichkeit der Fibern für das Experiment wird besprochen.

Contents

To someone

Acknowledgments

I would like to thank Ueli Straumann for letting me realize my PhD thesis in his group. His generosity, the freedom and trust he gave me made it only possible to gain so much knowledge and experience in realizing a project. Peter Robmann supported my a lot realizing this thesis. Thank you very much for all the help, inspiring discussions and the KaKü.

A great thank you goes to Arno Gadola. His calm and smart way to analyze problems helped me so often to step back when I thought there was no solution anymore to solve a problem. Our singing talents will be legendary one day. Thanks to Simon Corrodi who helped me so often with his smart and quick comprehension to answer questions and prevented me to look in the wrong direction. I am still impressed by your driving skills after having taken data for 18 hours in the dark and loud counting house. A merci beaucoup goes to the Geneva Group Antoaneta Damyanova and Sandro Bravar for providing me glued fiber ribbons and for all the adventures in Geneva: "The last chance in physics". For answering all the questions concerning data-analysis I thank Christian Elsasser and Marco Tresch. The convolution of arbitrary PDFs will always be a little bit of witchcraft for me. Every time I got stuck with a computer problem Nicola Chiapolini helped me to figure out how solve it. Thank you very much. For the critical comments on my writing skills I would like to thank Gaudenz Kessler. I will never again ignore the error outputs on LaTeX. Thank you Andries van der Schaaf for the challenging and very enlightening discussions. You pointed out a lot of things that did improve my work.

Thank you very much, Stefan Steiner, for all the hours of discussion about mechanical engineering. I learned a lot about how to build experiments that will even work at the end. I still impress people with my knowledge about self-locking threads. It was Achim Vollhardt that showed me the first time how to realize my own electronic project. Thank you very much for all the teaching and support to change my amplifiers from accidental sine generators to working devices.

There is a lot of staff at the Department of Physics that makes science possible in a first place. Thank you Kurt Bösiger, Reto Maier, Silvio Scherr, Bruno Lussi and Marcel Schaffner for all the mechanical support and for teaching me how to do it at my own. I will never show you my first attempt to drill a thread. Thank you, Lucien Pauli, for accepting my very own interpretation of the radiation safety rules. For all the patience of Roland Bernet with my experiments of "how to bring the departments computer network to its limit" I would like to thank. One day I will get the root-password. The administrative staff, Carmelina Genovese, Ruth Halter and Monika Röllin helped me so often to deal with the administrative hurdles of an university. Please apologize for having never filled in the order form.

I would also like to thank to the staff from PSI. The uncomplicated and extremely efficient ways all the people helped me was extraordinary. A special thank there goes to Konrad Deiters who let me sneak in on free times at the πM1 test-beam area. I will also never forget the discussion with the security officer about the pros and cons of having a Mercedes E class when you have more than ten dogs. I appreciate the spontaneous offer of Gallus Merki to help me setting up my equipment for a test-beam series. The group of Prof. Osterwalder let me use their laser setup and Matthias Hengsberger supported me with the measurements. Thank you very much.

A thank you goes to all the people calling our office with all possible questions concerning everyday life. It was a very welcome change to the hard daily work as a physicist to think about questions like: how does a car key work, whether Kevin Costner will safe the oceans, discussing a machine that can find arbitrary small amounts of gold or the daily problems of corn storage.

During my time as a PhD student I was also involved in several teaching and outreach duties. I would like to thank my students for all the inspiring questions and discussions that showed me new perspectives to a problem. A cordial thank you is owed to all my friends and in particular to Tove for all the emotional support. I would have been starved by now without all the nice dinners I was invited to. My deepest gratitude goes to my mother who always supported me and made it possible in first place to become a physicist.

— Roman —

Figure 1: Solar eclipse observation with the Straumann group 2015.

Du musst versuchen,
es zu akzeptieren

Andries van der Schaaf

1

Introduction

1.1 The Standard Model of Particle Physics

What is the world made of? What are the fundamental rules that dictate every reaction happening in the world? Such general questions seem to be unmanageable to answer because of their huge variety. These questions include a description of the world at a microscopic scale as well as in the dimension of the universe. Physics as a science tries to answer these questions in a way that the rules are valid on all scales. Even though it seems impossible to find an answer coping so many magnitudes in size and complexity, the *Standard Model* (SM) answers a lot of these questions with a remarkable precision. With the discovery of the Higgs boson [1, 2] at the Large Hadron Collider (LHC) the Standard Model could be completed by its last missing particle. The SM includes the physics of elementary particles and its interaction being a modular design principle. The building blocks of the modular design are the fermions divided in quark and leptons. In fact the everyday world as we experience is made of only the first generation of the fermions, being the up- and down-quark, the electron (e^-) and the electron-neutrino ν_e. With the first generation's quarks the proton and neutron can be build and, with the electron, atoms and higher complex molecules. Two additional generations exists with increasing masses. The second generation is made of the charm- and strange-quark with the muon (μ) and muon neutrino (ν_μ). In the third generation are the heaviest fermions, the top- and bottom-quark with the tau (τ) and the tau neutrino (ν_τ).

As we experience in every day life there are forces interacting between particles. We distinguish between four different forces:

- The *strong force* that tight quarks together to form *hadrons* as protons, neutrons and its related particles.
- The *electromagnetic force* being responsible that electrons stick to atomic nuclei.
- The *weak force* mediating decays from heavy particles to their lighter parters from another generation.
- *Gravity* that acts on massive objects. The most experienced force in everyday life.

The SM describes forces in Quantum Field Theory (QFT) with the help of force carriers, the *bosons*. An interaction between particles can be described by an exchange of these force carriers. The strong force is therefore mediated by *gluons* g, the electromagnetic force by *photons* γ, being the smallest quantum of light and the W and Z boson being responsible for the radioactive decay. Gravity is not incorporated in the SM. There is no force carrier like a *graviton*.

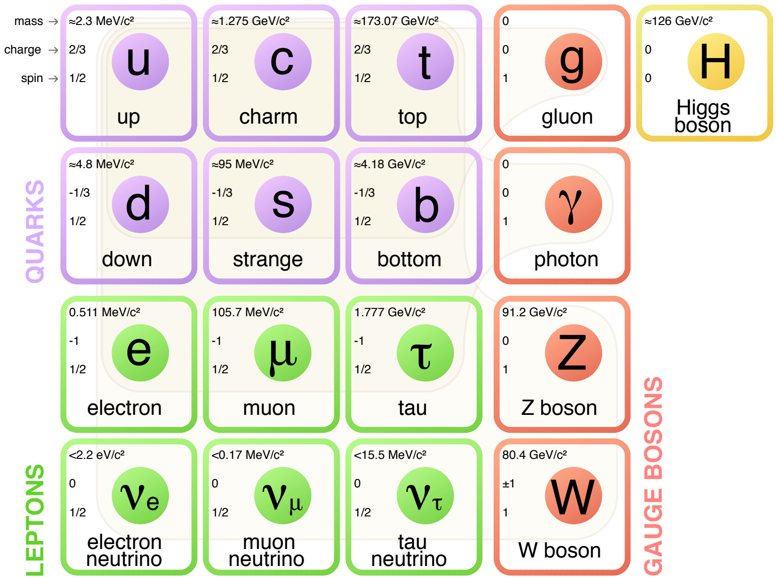

Figure 1.1: The Standard Model of particle physics with the matter particles leptons and quarks, the gauge bosons which mediate the electric, weak and strong force, and the Higgs particle. [3]

Even though the SM has been tested with great success over the last decades it is not a complete theory. The SM can not explain phenomena such as:

Neutrino Masses As discussed in more detail in section 1.2 lepton flavour is a conserved quantity in the Standard Model. Neutrino oscillation experiments disproof the conservation of the lepton flavour for neutrinos and implies that neutrinos have a mass different from zero.

Dark Matter and Dark Energy Only about 5 % of the of the energy in the universe can be explained by ordinary matter as described by the SM. 26 % are believed to be dark matter as postulated by Fritz Zwicky [4] and the remaining 69 % as dark energy.

Matter–antimatter asymmetry The absence of an equal amount of antimatter as matter in the universe can not be explained by the SM as it would predict a production of an equal amount of both in the universe.

1.2 LEPTON FLAVOUR VIOLATION

Summary of [5–7]. An nice overview focusing on the history of experiments is given in [8]. For the leptons there exists a quantum number, the lepton flavour L_l, where l is defined by the lepton generation as e, μ and τ. The lepton flavour L_l is equal to 1 for the corresponding lepton generation and 0 otherwise (table 1.1).

Table 1.1: Summary of the lepton flavours for the three lepton generations.

particle	L_e	L_μ	L_τ	particle	L_e	L_μ	L_τ	particle	L_e	L_μ	L_τ
e^-	1	0	0	μ^-	0	1	0	τ^-	0	0	1
ν_e	1	0	0	ν_μ	0	1	0	ν_τ	0	0	1
e^+	-1	0	0	μ^+	0	-1	0	τ^+	0	0	-1
$\overline{\nu_e}$	-1	0	0	$\overline{\nu_\mu}$	0	-1	0	$\overline{\nu_\tau}$	0	0	-1

In the standard model lepton flavour is conserved at tree level. The observation of neutrino oscillations by experiments such as SuperKamiokande [9], SNO [10], and KamLAND [11] is, however, a direct proof of lepton flavour violation (LFV). In the extended standard model neutrinos have a mass different from zero and the lepton flavour violation in the oscillation is explained by neutrino mixing. Charged LFV (CLFV) would lead to $\mu \to e$ and $\tau \to \mu$ transitions without neutrinos in the final state. However, in the extended standard model CLFV is strongly suppressed even though the mixing angles in the neutrino matrix have been measured to be large. As an example branching ratio in the $\mathcal{B}(\mu \to e)$ channel is [7]

$$\mathcal{B} \propto \left| \Sigma_{i=2,3} U^*_{\mu i} U_{ei} \frac{\Delta {m_{i1}}^2}{{m_W}^2} \right|^2 < 10^{-54} \tag{1.1}$$

where $U_{\alpha i}$ are the elements of the neutrino mixing matrix, the $\Delta m_{i1}{}^2$ the squared neutrino mass differences and m_W the W-boson mass. The mass difference between the neutrinos ($<$2 eV and the W-boson 80 MeV) heavily suppresses CLFV in the neutrino mixing channel (cf. fig. 1.2). The resulting branching ratios are way beyond the experimental sensitivity. An observation of CLFV would therefore directly signal physics beyond the standard model. Introducing new heavy particles can increase the branching ratio by orders of magnitudes. Two examples are shown in fig. 1.2 as well. There are many extensions of the SM like unified models [12–14], supersymmetric models [15], left-right symmetric models [16–18] and models with an extended Higgs sector [19]. Experiments looking for CLFV are therefore ideal candidates to search for physics beyond the standard model.

Muon number violation has already been investigated in different channels (see table 1.2 and fig. 1.3, right). When these processes would be observed, their relative strengths would guide the attempts to identify the underlying mechanism.

Table 1.2: Experimental upper limits on the branching ratios $\mathcal{B}$ of LFV muon decays

Decay channel	Experiment	$\mathcal{B}$ upper limit	Ref.
$\mu \to e\gamma$	MEGA	1.2×10^{-11}	[20]
	MEG	2.4×10^{-12}	[21]
	MEG	5.7×10^{-13}	[22]
$\mu \to eee$	SINDRUM	1.0×10^{-12}	[23]
$\mu^-\mathrm{Au} \to e^-\mathrm{Au}$	SINDRUM II	7×10^{-13}	[24]

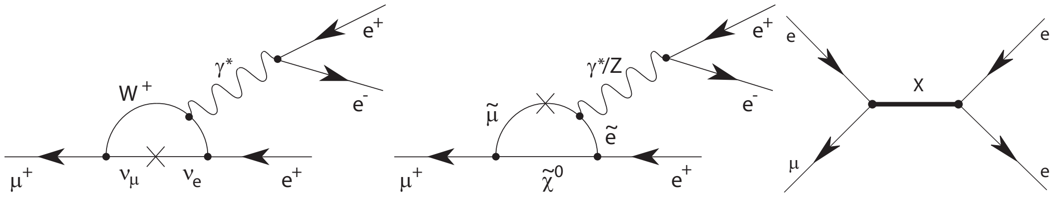

Figure 1.2: Possible $\mu^+ \to e^+e^-e^+$ mechanisms. From the left: neutrino mixing allowed within the extended standard model, a supersymmetric contribution, and LVF at tree level.

1.3 The Decay $\mu^+ \to e^+e^-e^+$

The decay $\mu^+ \to e^+e^-e^+$, or written in its short form $\mu \to eee$, is a LFV decay mediated via loops or at tree level by introducing new particles. The most general Lagrangian of this decay writes as [25]

$$
\begin{aligned}
\mathcal{L}_{\mu\rightarrow eee} \;=\; & -\frac{4G_F}{\sqrt{2}}\Big[m_\mu A_R\,\overline{\mu_R}\sigma^{\mu\nu}e_L F_{\mu\nu} + m_\mu A_L\,\overline{\mu_L}\sigma^{\mu\nu}e_R F_{\mu\nu} \\
& + g_1\left(\overline{\mu_R}e_L\right)\left(\overline{e_R}e_L\right) + g_2\left(\overline{\mu_L}e_R\right)\left(\overline{e_L}e_R\right) \\
& + g_3\left(\overline{\mu_R}\gamma^\mu e_R\right)\left(\overline{e_R}\gamma_\mu e_R\right) + g_4\left(\overline{\mu_L}\gamma^\mu e_L\right)\left(\overline{e_L}\gamma_\mu e_L\right) \\
& + g_5\left(\overline{\mu_R}\gamma^\mu e_R\right)\left(\overline{e_L}\gamma_\mu e_L\right) + g_6\left(\overline{\mu_L}\gamma^\mu e_L\right)\left(\overline{e_R}\gamma_\mu e_R\right) + \text{h.c.}\Big]
\end{aligned}
\tag{1.2}
$$

where the first two terms, the tensor type couplings with the form factors $A_{R,L}$, are mainly described by loop and box diagrams. The tree diagram contributes in leading order to the scalartype $g_{1,2}$ and vectortype g_{3-6} form factors, regarded as four fermion contact interactions [5].

To compare μ → eee with μ → eγ where with the latter physics beyond the SM is only tested by photon penguin diagrams, a simplified Lagrangian is introduced with a common mass scale Λ where only the photon penguin diagram and the tree are the relevant contributions [5]:

$$
\mathcal{L}_{\mathrm{LFV}} = \left[\frac{m_\mu}{(\kappa+1)\Lambda^2}\overline{\mu_R}\sigma^{\mu\nu}e_L F_{\mu\nu}\right]_{\gamma\text{-penguin}} + \left[\frac{\kappa}{(\kappa+1)\Lambda^2}\left(\overline{\mu_L}\gamma^\mu e_L\right)\left(\overline{e_L}\gamma_\mu e_L\right)\right]_{\text{tree}}
\tag{1.3}
$$

For the contact term the left-left vector coupling is chosen as an example. The ratio of the amplitudes of the tree over the γ-penguin term is parametrized as κ. The limits of the mass scale is shown as a function of κ in fig. 1.3. They are derived from data of the MEG 2011 [21] result, the MEG 2013 [22] result and the SINDRUM experiment [23] as well as for the proposed 10^{-16} sensitivity for the μ → eee experiment [5] (see next chapter). For low values of κ the μ → eγ experiments constrain Λ the best, while μ → eee experiments reveals constraints at high κ values.

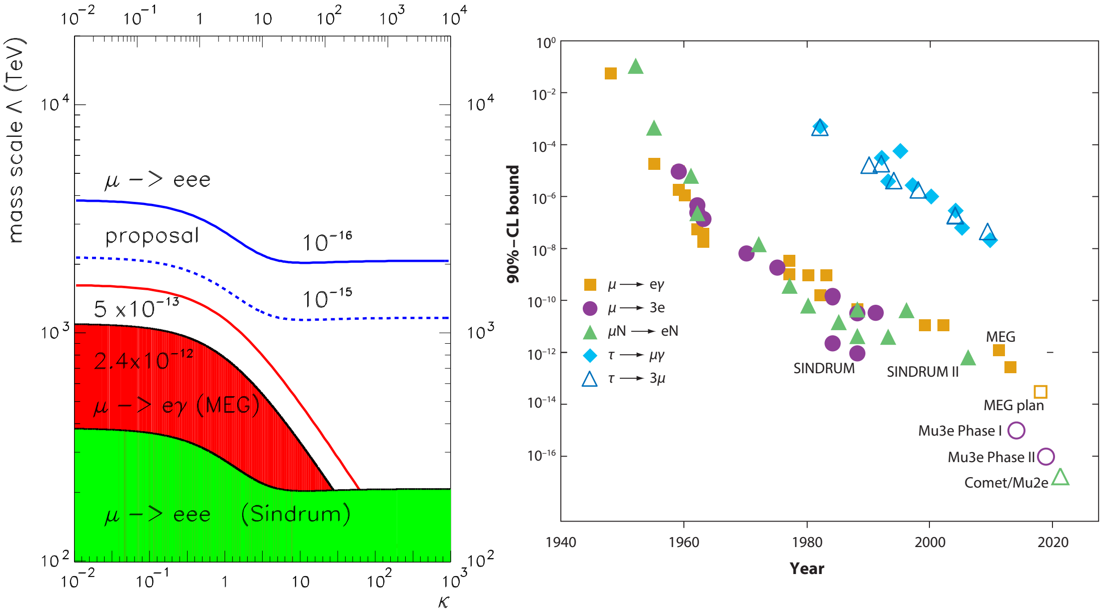

Figure 1.3: Left: experimental limits and projected limits on the LFV mass scale Λ as a function of the parameter κ as described in eq. (1.3). Adapted picture from [7] and updated from [5]. Right: sensitivity history of LFV experiments with the proposed sensitivity for the $\mu \to eee$ experiment. Updated from [26].

2

The Mu3e detector

2.1 Goal of the Experiment

The Mu3e experiment is a dedicated experiment designed to detect the LFV decay $\mu^+ \rightarrow e^+e^-e^+$ with a branching ratio $\mathcal{B} < 10^{-16}$ or to exclude it at 90 % certainty level [5]. To achieve this in a reasonable time, a decay rate of up to 10^9 muon decays per second is aimed. It is planned to achieve this goal within two phases. In phase I only a subset of the detector is running and a sensitivity down to a branching ratio of $\mathcal{B} = 10^{-15}$ is aimed. Phase II will increase momentum resolution and the detectors acceptance leading to the final sensitivity of 10^{-16}. The experiment aims at an energy coverage for the electrons higher than 10 MeV that will lead to an acceptance for about 50 % for all present known models beyond the SM. A signal event in Mu3e is the detection of two positrons and one electron with a common vertex and a vanishing sum of their momenta $\Sigma\vec{p}_i = 0$. The total energy of the electrons has to be the mass of a muon, stopped in the target.

2.2 Background Rates

The main challenge in this experiment is the background suppression. The major irreducible background is generated by the internal conversion (IC) $\mu \rightarrow ee e\nu\nu$ with a branching ratio of $\mathcal{B} = 3.4 \cdot 10^{-5}$ [27]. The signal of the IC can be distinguished from $\mu \rightarrow eee$ by detecting the missing momentum and energy that is carried away by the neutrinos. An excellent momentum resolution of less than 0.5 MeV/c is required to reach a sensitivity of 10^{-16} (fig. 2.1).

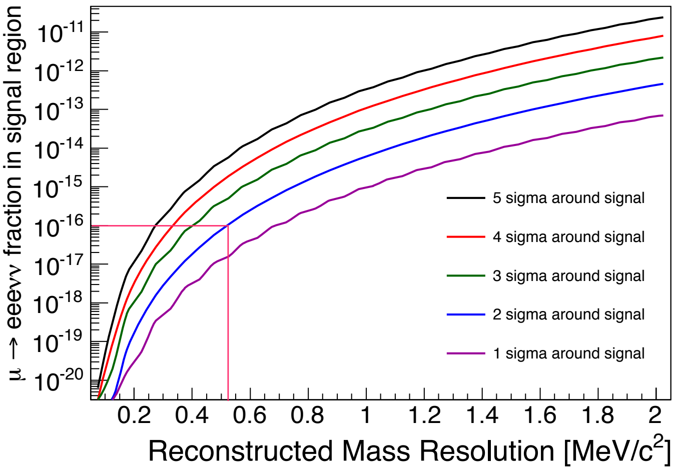

Figure 2.1: Contamination of the signal region with internal conversion events [5].

A second source of background is the combinatorial background. Expecially since there is no correlation in time from the incoming muons and their decay (discussed in more detail in sections 2.3.2 and 2.3.3). In this form of background the source is a mismatch of uncorrelated electrons. Possible combinations are:

- One Michel decay positron and an additional electron/positron pair
- Two Michel decay positrons with an additional electron

The electron positron pair can be produced by Bhabha scattering in the detector material, which is the dominant source actually. Another source is the pair production from a photon within the detector. The photon itself can originate from Bremsstrahlung or via the $\mu^+ \rightarrow e^+\gamma\nu\nu$ radiative muon decay. Combinatorial background of two Michel decays and a third electron, for example from photon conversion, needs to be suppressed. The background rates are summarized in table 2.1. An excellent vertex locator with a resolution of about 200 μm, precise timing of 100 ps and a momentum measurement with a precision down to 0.5 MeV c^{-1} are essential for the background suppression. Additional scintillator timing detectors are foreseen to suppress combinatorial background.

The low momenta of the electrons ($p < 53\,\mathrm{MeV}/c$) results in large multiple scattering effects and thus the material in the active area should be reduced to a minimum. Therefore the detector will be operated in a gaseous helium atmosphere. There will be a helium flow of about 3 m s^{-1} to cool active components. In particular the silicon

Table 2.1: Background rate per muon decay as expected in the different phases of the experiment [28, 29]. The phases are explained in section 2.3.

Background Process	Phase Ia	Phase Ib	Phase II
Bhabha scattering + 1 Michel	$3 \cdot 10^{-15}$	$5 \cdot 10^{-16}$	$6 \cdot 10^{-16}$
Bhabha scattering + 2 Michel	$2 \cdot 10^{-16}$	$1 \cdot 10^{-18}$	$3 \cdot 10^{-17}$
Radiative decay + 1 Michel	$1 \cdot 10^{-16}$	$2 \cdot 10^{-17}$	$2 \cdot 10^{-17}$
Radiative decay + 2 Michel	$3 \cdot 10^{-18}$	$2 \cdot 10^{-20}$	$5 \cdot 10^{-19}$
Compton + 2 Michel	$6 \cdot 10^{-18}$	$4 \cdot 10^{-20}$	$9 \cdot 10^{-19}$
Internal conversion + 1 Michel	$4 \cdot 10^{-18}$	$6 \cdot 10^{-19}$	$7 \cdot 10^{-19}$
Internal conversion + 2 Michel	$1 \cdot 10^{-18}$	$8 \cdot 10^{-21}$	$8 \cdot 10^{-20}$

pixel sensors are cooled by gaseous helium. The readout electronics and timing detectors will be cooled by an additional liquid water cooling system outside the active area.

2.3 Detection Concept

The design of the detector is a barrel concept that consists of several concentric layers with different sensors. In the middle of the detector a Mylar double cone target will be placed that stops the muons. Several radial layers of thin silicon pixel sensors measure the momentum and determine the vertex of the decay particles. Scintillation detectors will complement the pixel sensors with very precise time information. The detector will be operated in a magnetic field of 1 T. The momentum measurement is crucial to suppress the internal conversion background. The detector aims to have a momentum resolution as high as possible while the momentum acceptance is still wide (fig. 2.2). In a momentum range of $p = 15 - 53\,\mathrm{MeV}/c$ the resolution is dominated by multiple scattering. In first order approximation the resolution in a homogeneous magnetic field is

$$\frac{\sigma_p}{p} \propto \frac{\Theta_{\mathrm{MS}}}{\Omega} \tag{2.1}$$

where Θ_{MS} is the multiple scattering angle and Ω the lever arm (i.e. the bending angle). Equation (2.1) shows that placing the tracking station at higher radii increases the momentum resolution. Such a configuration would on the other hand lead to a decrease of the momentum acceptance by cutting on lower momenta. Therefore the detector is designed to measure so called *re-curlers* providing a large acceptance and a high lever arm. Additionally in such a configuration the lever arm Ω comes closer to a half turn where multiple scattering effects cancel out at first order.

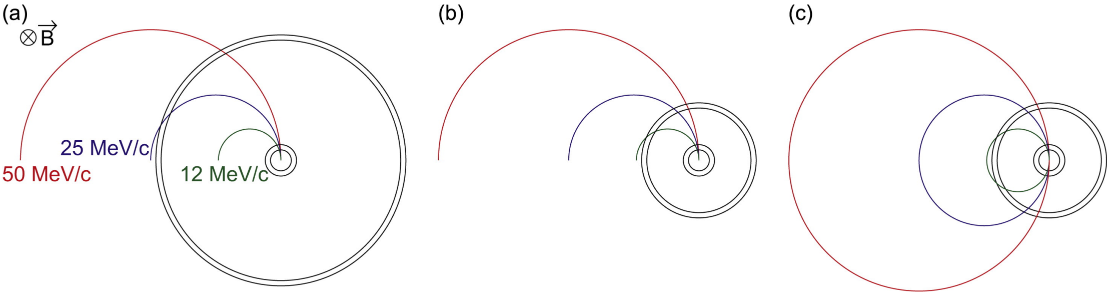

Figure 2.2: *a)* detector optimized for large lever-arms: low momenta particles are not tracked anymore. *b)* detector optimized for high acceptance: momentum resolution reduced due to small lever-arm. *c)* recurling principle: high detector acceptance and large lever-arm due to detecting particles again after recurling [30].

2.3.1 THE MODULAR BUILDING PRINCIPLE

PHASE I DETECTOR

The design of the Mu3e detector is realized in a modular principle. In phase Ia only the center module will be built (fig. 2.3). This configuration consists of the stopping target, four layers of silicon pixel sensors and a magnet providing a homogeneous 1 T magnetic field. In this starting configuration a muon stopping rate of $1 \cdot 10^7$ μ^+/s is planned. Each module will have a length of 36 cm. The first tracking layers of the central module are at a radius of 12 cm and the outer layers at 17 cm.

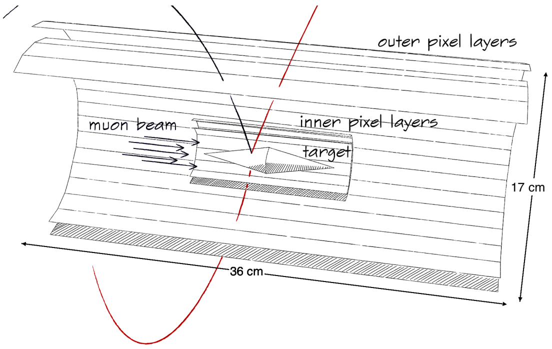

Figure 2.3: Schematic of the Mu3e detector for phase Ia. The muon stopping target and four coaxial Si pixel sensors are shown. The station has a diameter of 17 cm and a length of 36 cm [30].

In phase Ib (fig. 2.4) the muon stopping rate will be increased to a rate of $1 \cdot 10^8$ μ^+/s. The central module will be extended with three layers of 250 µm thick scintillator fibers. Two additional *recurl* modules including pixel sensors and scintillator tiles will significantly increase the momentum resolution to ∼0.5 MeV/c and provide a timing resolution below 1 ns.

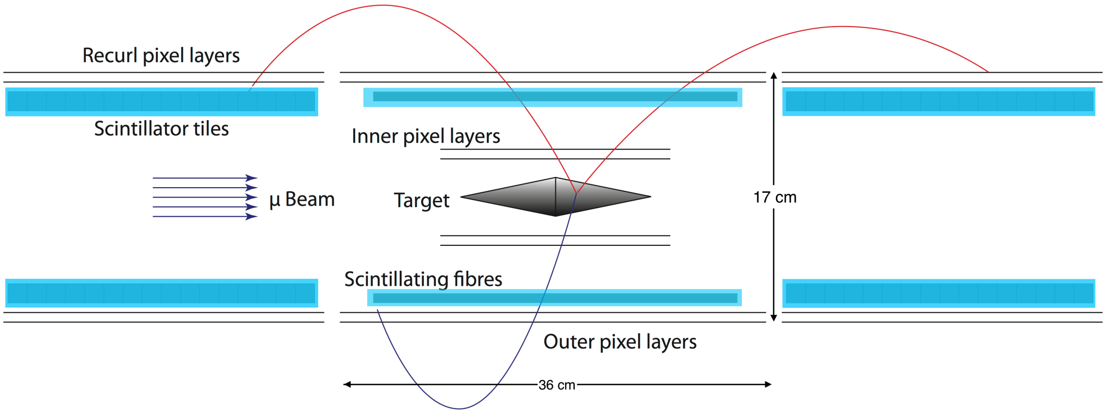

Figure 2.4: Schematic of the Mu3e detector for phase Ib. For a better overview only a cut is shown. The blue layer in the central module shows the 250 μm fibers attached at the inside of the outer pixel sensors. In the two stations to the side the blue layer visualizes the position of the scintillator tiles [30].

PHASE II DETECTOR

The final detector in phase II will be extended by two additional recurl stations (fig. 2.5) that are identical to the recurl station introduced in phase Ib. The additional modules will increase the acceptance of the recurlers to the same level as defined by the central module. Only in this stage the final muon stopping rate of $1 \cdot 10^{9}\ \mu^{+}/\mathrm{s}$ is introduced to reach the final sensitivity of 10^{-16}.

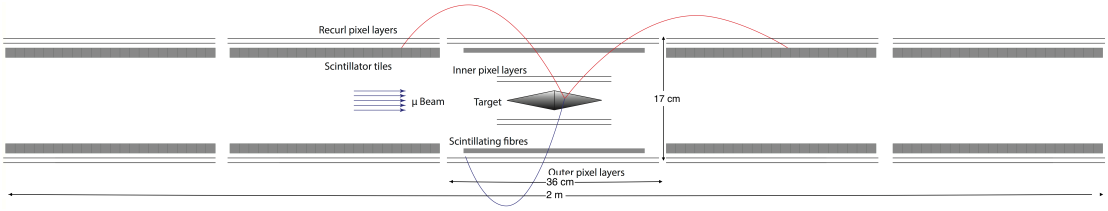

Figure 2.5: Schematic of the Mu3e detector for phase II. The final detector in phase II consists of two more stations that are identical to the two stations on the side. The overall length of the final detector will be about 2 m [30].

2.3.2 MUON BEAM AT THE PAUL SCHERRER INSTITUTE

The Paul Scherrer Institute (PSI) in Switzerland already provides the most intense DC muon beam in the world. First a proton beam is accelerated with a Cockcroft-Walton column to 870 keV/c. In a second step the protons are accelerated to 72 MeV/c in a cyclotron. Finally, the protons are accelerated to 590 MeV/c in an eight-sector ring cyclotron. Proton currents up to 2 mA are possible [31]. The muons originate from the decay of pions produced by the interaction of the proton beam with the nuclei of two different carbon targets, the target M with a thickness of 5 mm and the target E at a thickness of 40 mm to 60 mm (section 6.2 for more details).

For the Mu3e experiment two new beamlines are under investigation. The experiment's phase I requires 10^8 muon stops per second. It has already been proofed that the πE5 beamline can provide $\sim 10^8$ 28 MeV/c muons per second [32]. For the phase II of the experiment a new beamline needs to be designed. Feasibility studies are currently ongoing at the PSI [33].

2.3.3 Stopping Target

The design of the stopping target is driven by the requirement for a maximum possible stopping power and a minimal material thickness to avoid a deterioration of the momentum resolution by multiple scattering. Spreading out the stopped muons to a big area helps to reduce accidental background. The current design is similar to the SINDRUM [23] target, a Mylar hollow double cone with a thickness of 75 µm upstream and 85 µm downstream (fig. 2.6). It is produced gluing Mylar foils of a thickness between 24 µm and 50 µm with an epoxy resin. The target has a central diameter of 38 mm and a total length of 100 mm. The half opening angle of the target cone of 20.8° leads to an effective thickness of 211 µm at the front part and 239 µm at the back. Overall this leads to a radiation length of 0.16 %.

With the help of nylon fishing lines the target is mounted in the center of the detector. The total heating power by stopping 10^9 muons per second is smaller than 1 mW and can be cooled easily by the gaseous helium flow. This does not contribute significantly to the total heating power compared to the active sensors (cf. section 2.3.5).

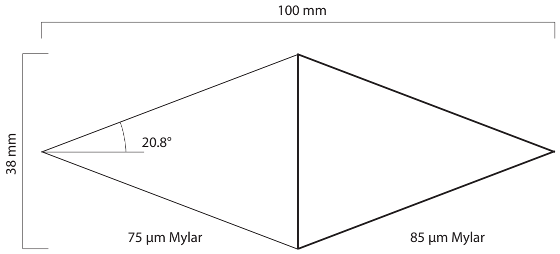

Figure 2.6: Schematic of the muon stopping target. The thickness of the foil is not to scale. Updated from [34].

2.3.4 MAGNET

The electron momenta are intended to be measured in a homogeneous 1 T solenoidal magnetic field. The cylindrical bore has a diameter of 1 m and a length of more than 2 m. The magnet is not only used for the momentum measurement but it also is a beam optical element guiding the muons to the stopping target. With a nominal field strength of 1 T the field can be varied from 0.5 T to 2 T for systematic studies and for a reuse of the magnet for further experiments in the future. The minimal diameter of the bore is given by the maximum momentum of 53 MeV/c of the particles and a minimal field strength of 0.8 T where the measurement of recurling particles is still intended to be measured. For the field homogeneity a longer magnet would be preferable. But due to the tight space constraints, the outer length of the magnet cannot be longer than 3.2 m (fig. 2.7). A field drop up to 50 % at the magnet ends needs to be compensated with two additional coils. A field stability in time is achieved by monitoring the magnetic field strength inside the experiment and by controlling the power supplies of the magnet.

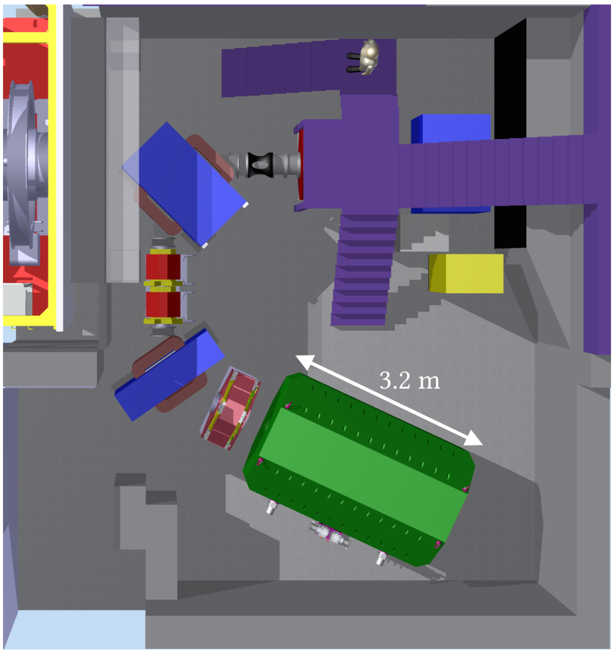

Figure 2.7: CAD model of the phase I experiment in the πE5 area at PSI. The length of the magnet (green) is constrained by the tight space in the area [30].

The magnet will have a shielding outside. Shielding is needed to not disturb other experiments or equipment in the experimental hall. It is also useful for the experiment itself as it improves the homogeneity of the field and it shields the experiment from external disturbances and helps therefore to keep the field constant over time. The parameters of the magnet are summarized in table 2.2.

Table 2.2: Magnet parameters for Mu3e. Updated from [5].

parameter	value	parameter	value
field for experiment	1 T	field stability $\Delta B/B$ (100 days)	$\leq 10^{-4}$
field range	0.5 T to 2 T	outer length	< 3.2 m
bore diameter	1 m	outer width	< 2 m
bore length	2.7 m	outer height	< 3 m
field description $\Delta B/B$	$\leq 10^{-4}$		

2.3.5 PIXEL DETECTOR

With the Mu3e experiment a new pixel sensor technology will be introduced, the High Voltage Monolithic Active Pixel Sensor (HV-MAPS) [35]. The sensor consists of a depleted area biased with $\sim$ 70 V enabling a fast $\mathcal{O}(1\,\text{ns})$ charge collection via drift (fig. 2.8, left). The digitization and the serial driver to write out the (zero suppressed) data are part of the sensor itself. The data that is written out consists of the hit pixel address and a timestamp.

Each sensormodule consists of an active area of $20 \times 20\,\text{mm}^2$ with an individual pixel size of $80 \times 80\,\mu\text{m}^2$. The sensor thickness will be less than 50 µm. Together with a Kapton support structure of 25 µm and flex-print cables that provide supply voltage and readout data lines, the thickness corresponds to about 1 permille radiation length X_0 (fig. 2.8, right). In the current prototype design (version 7) the chip already reaches a time resolution of $\sim$ 11 ns with a pixel efficiency of $> 99\,\%$ [36]. Using such small pixels the tracking resolution is dominated by multiple scattering. Therefore a smaller pixel size does not help to improve the detector resolution. The HV-MAPS are produced by commercial CMOS technology as it is widely used in industrial processes leading to a rather cheap production. The current pixel R&D achieved a working chip at a still smaller active area of $2.9 \times 3.2\,\text{mm}^2$. A new series of chips is under commissioning that will have the proposed size of the active area.

2.3.6 TILES

The plastic scintillator tiles that are placed at the outer detector modules have a size of $7.5 \times 7.5 \times 5\,\text{mm}^3$. Each station of the detector will have 3360 tiles where each of them is read out individually by a single silicon photomultiplier (SiPM). 32 tiles

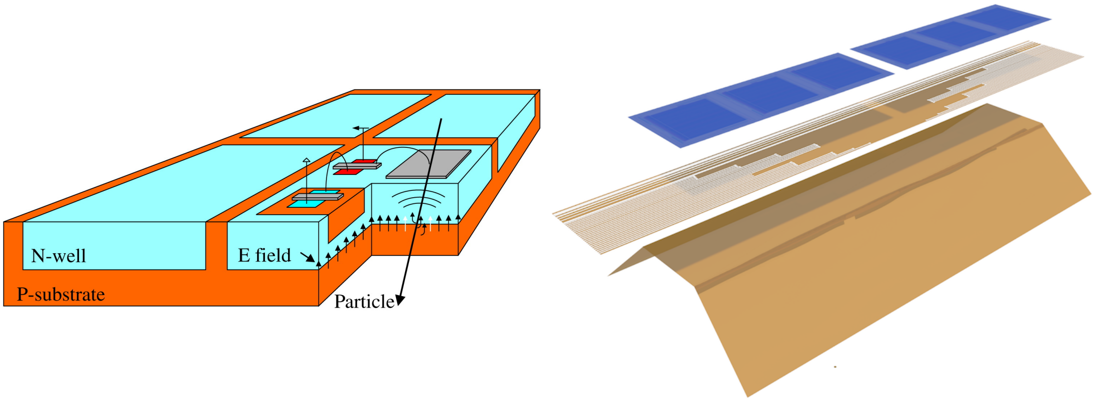

Figure 2.8: Left: Schematic view of HV-MAPS showing four pixels [35]. Right: Support structure with the HV-MAPS on top, flexprint cables in the middle and Kapton at the bottom.

will be combined to submodules, as shown in fig. 2.9 left, with two 4 × 4 tile arrays. 15 submodules together form a module of 480 channels. These modules are placed around the beam pipe (fig. 2.9, right) covering one station. For the tiles the required time resolution of better than 100 ps has already been demonstrated in several test-beam measurements [28].

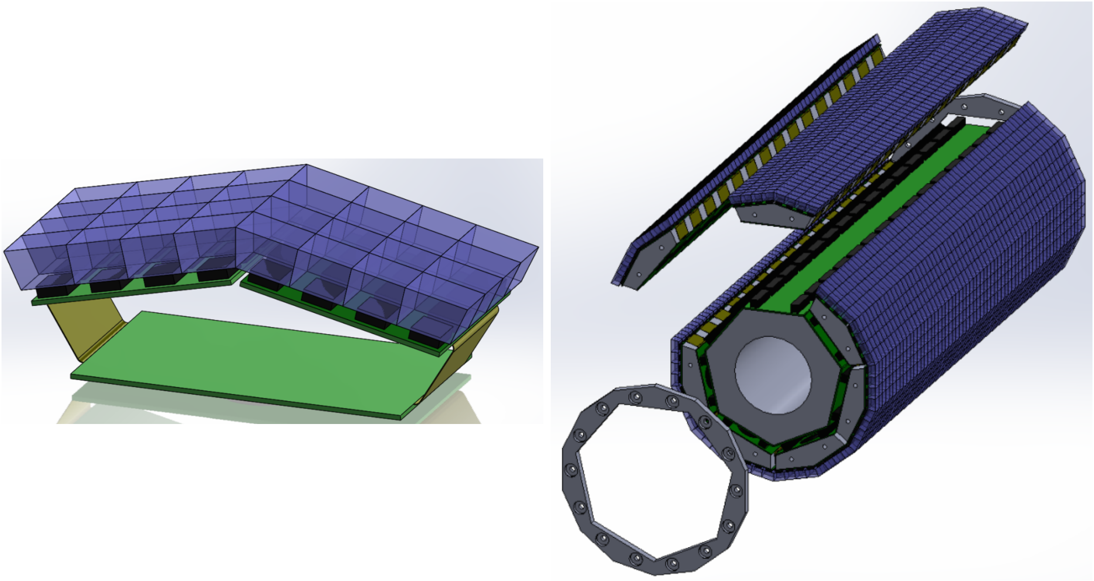

Figure 2.9: Left: Submodule of the tile detector. Right: Explode view of an fully equipped detector station with seven modules [28].

2.3.7 The Mu3e fiber Detector

The time of flight detector

In the central module a cylindrical time of flight detector complements the central pixel tracker. It consists of a scintillator fiber hodoscope at a radius of 6 cm with a length of 30 cm. The time resolution goal of this detector is below 1 ns assuming a Gaussian distribution. This detector will provide a precise time information to the pixel hit position in order to suppress accidental background and contributes to the identification of recurling electrons.

The baseline design are three layers of round double cladding fibers with a diameter of 250 μm each. With an additional titanium oxide coating the light yield is expected to be improved to reach a detection efficiency above 95 %. In phase I the fibers are read out column wise at both fiber ends with SiPMs. SiPMs are the detector of choice because of their small size compared to photomultiplier tubes and they can easily be operated in high magnetic fields. For phase II the fibers need to be fan out for an individual readout per fiber. They are designed to work to particle rates up to several MHz.

The fibers are glued together with an epoxy resin to 16 mm wide modules called ribbons that are self supporting, i.e. they need no further support structure. Prototypes of such modules have already been produced (fig. 2.10 and fig. 2.11).

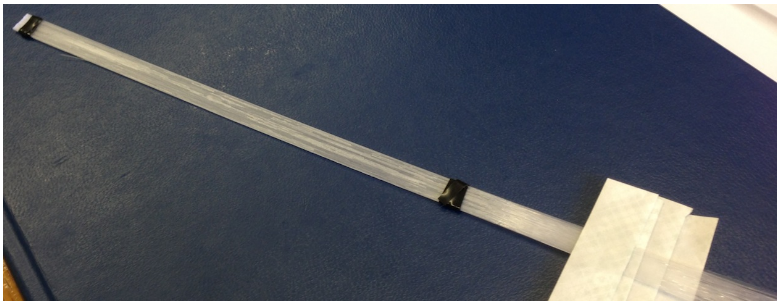

Figure 2.10: Early prototype of a fiber ribbon. This model has only a width of 8 cm.

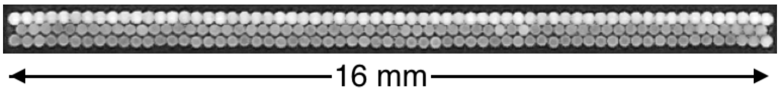

Figure 2.11: Front view of the first fiber ribbon prototype with the full width.

The effect of the fibers for the background suppression is shown in fig. 2.12. In this simulation for the phase I of the experiment a three layer fiber detector is assumed with a column wise readout. The time resolution is assumed to be 500 ps for the fiber tracker. On the target a stopping rate of 10^8 muons per second is assumed. For the tiles a time resolution of 60 ps is assumed. The fiber system achieves a background suppression at one order of magnitude.

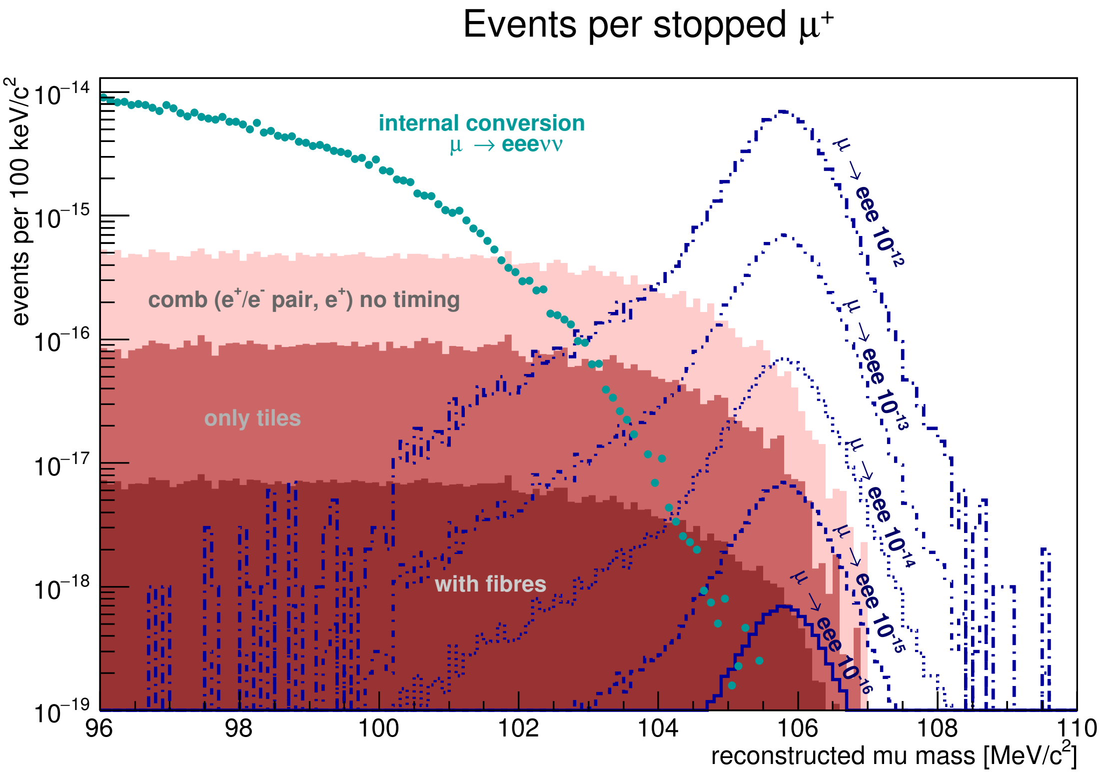

Figure 2.12: Preliminary background estimation for the phase I of the experiment showing the improvement by using only the tiles (red) and by the combination of tiles and fibers (dark red). The expected background using the pixel sensors only is shown in pink. In this simulation 10^8 muons/s are stopped. The fiber time resolution is simulated as 500 ps per layer [37].

MECHANICAL INTEGRATION

The mechanical integration of the fibers within the detector is currently still at R&D stage. Therefore the following section is considered to be preliminary. Similar to the scintillator tiles, the fiber detector is based on a modular principle. One module consists of four fiber ribbons each. Six modules together form the whole fiber detector (fig. 2.13). The space available inside the detector is highly limited. To fit all the ribbons with the readout sensors and its electronics in the dense area neighboring ribbons will have a radial offset of about 2 mm to 5 mm. This way the fiber ribbons can be made wide enough to minimize the dead area between the ribbons even though the readout electronics and the cables need more space and are therefore wider than 16 mm (fig. 2.14).

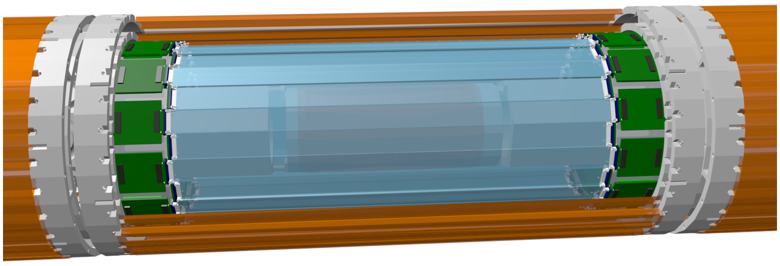

Figure 2.13: Rendering of the fiber modules (blue) within the central part of the detector. The electronic readout printed circuit boards (PCB) for the fibers are shown in green. The pixel detectors are shown in orange [37].

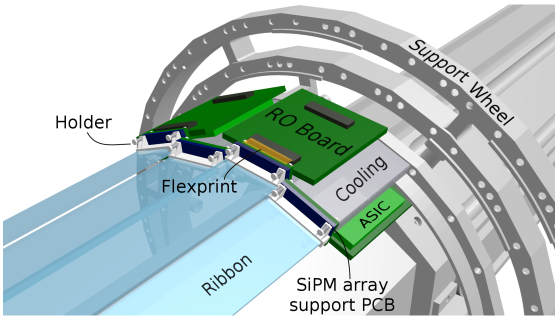

Figure 2.14: Zoom to the end of the fiber ribbon showing the connection to the SiPMs and electronic PCBs. A radial offset between two ribbons is mandatory to fit in all the readout electronics and its cooling [37].

Fiber Readout

The baseline design uses the SiPM Timing Chip (STiC) [38] and a successor, the MuSTiC, a dedicated development for Mu3e. It will be used to read out the fibers and the tiles. The STiC chip is a mixed mode ASIC containing the analogue and digital part. For the analogue input two thresholds are used. The lower threshold specifies the timestamp of the input signal while the second threshold specifies the charge of the input signal measuring the time over threshold. The intrinsic STiC time resolution has been measured being $\sigma_{\text{STiC}} < 30\,\text{ps}$ [39]. The STiC chip allows to vary the bias voltage within a window of 0.7 V. This allows to compensate the variations of the optimal SiPM bias voltage between different channels.

The STiC chip has been designed for positron emission tomography (PET) applications with lutetium-yttrium oxyorthosilicate scintillator crystals where thousands of photons are expected. Therefore it can directly be used for the tile detector. For the fibers the STiC needs to operate with a few photons only. As SiPMs have high dark rates at low thresholds the main development for MuSTiC is to speed up the serial link[1] to write out the data.

Alternative Options

Complementary to the system mentioned above an alternative of squared double cladding fibers is tested at the PSI. The squared fibers provide more light and therefore a better time resolution is expected. The disadvantage is that the construction of a ribbon with squared fibers is much more difficult.

2.4 Data Acquisition

The Mu3e experiment produces overall several $\text{Tbit}\,\text{s}^{-1}$ zero-suppressed data. Fig. 2.15 shows the readout of the experiment. The STiC chips from the tiles and fibers and the HV-MAPS pixel sensors provide digital differential LVDS links to the front-end FPGAs placed close to the detector. The front-end FPGAs merge and buffer data from the LVDS links and send them via optical links to the counting house. The optical links are not only needed to provide high enough bandwidth to transfer the data to the counting house but it also decouples the detector galvanically from the counting house electronics. The data is sent to the counting house by time slices to four different readout board groups (group A to D as shown in fig. 2.15) of the event filter farm in sequence. Each group consists of eight readout boards that are driven by FPGAs. The

---

[1] The STiC and the MuSTiC use low voltage differential signaling (LVDS) for data transmission

switching network is needed to distribute the load between different sub-farm computers. It is built such that all front-end FPGAs switch simultaneously so that each sub-farm gets all data from a specific time-slice. The sub-farm FPGAs are connected to 12 computers for each sub-farm. In each computer is a third FPGA that rejects already tracks that are not coinciding in time. The rest of the data is sent to a graphics processing unit to reduce combinatorial background by reconstructing the muon vertex position. At the end the data written to tape will be reduced to less than $100\,\mathrm{MB\,s^{-1}}$ [40].

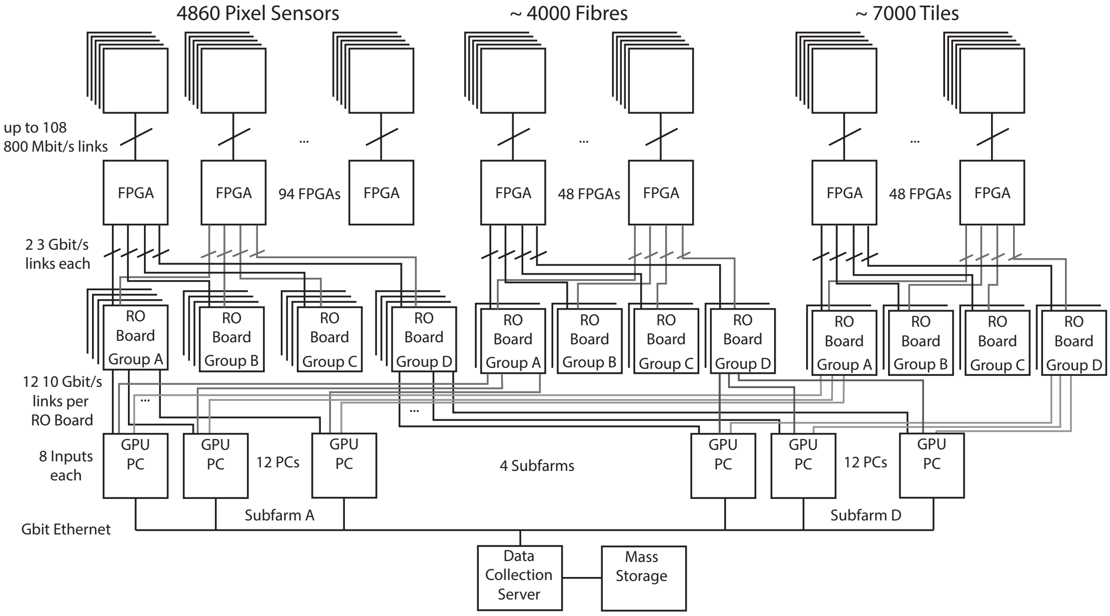

Figure 2.15: Three staged readout scheme for Mu3e [40]. The data from the fibers, tiles and pixel sensors is sent via LVDS links to the first front-end FPGAs. Optical fibers send the data from the front-end FPGAs to the counting-house FPGAs. From there the data is distributed to all the computers.

3

Scintillator Detectors

The present thesis focuses on the scintillating fiber detector of the Mu3e experiment. In this chapter the a detailed overview on the scintillation mechanism of organic scintillators is discussed and the working principle of semiconductor based photon detectors is introduced. The physics of scintillator detectors needs to be understood in detail to provide an accurate simulation as discussed in chapter 4 and to understand the results in chapter 6.

3.1 SCINTILLATORS

The emission of photons due to the deposition of energy in a material is called luminescence. The energy deposit can be from different origins as by light (photoluminescence), sound (sonoluminescence) [41], electrical energy (electroluminescence) [42] or even by mechanical deformation (triboluminescence) [43]. Chemical reactions can also produce light (chemoluminescence) as nicely seen in particular as bioluminescence in warm summer nights by fireflies.

The emission of photons due to an energy deposit from particles via ionization and from γ-particles is called *scintillation*. One of the first scintillating detectors was probably used by Sir William Crookes (1903) by using a zinc sulphide screen where light has been detected by eye when it got struck by α-particles. With the combination of the scintillator with a photon multiplier tube in 1944 the first scintillating detector was born that could be used with an electrical readout. Since then scintillating detectors are used in a big variety in tracking detectors, trigger systems and also for building calorimeters. Nowadays scintillators are used in physics, chemistry as well as in imaging methods in medicine such as but not only PET scanners and x-ray computed tomography (CT) [44, 45].

The amount of light produced in scintillators is almost linear to the deposited energy. Deviations due to quenching effects between neighboring molecules are empirically described by the *Birk's law* by the light yield per path length [46, 47] as

$$\frac{\mathrm{d}L}{\mathrm{d}x} = L_0 \frac{\frac{\mathrm{d}E}{\mathrm{d}x}}{1 + kB\frac{\mathrm{d}E}{\mathrm{d}x}} \tag{3.1}$$

with L_0 the light yield, $\mathrm{d}E/\mathrm{d}x$ the energy loss of the particle per path length and kB the Birk's constant measured as $0.126\,\mathrm{mm\,MeV^{-1}}$ [48] for polystyrene based scintillators. The emission of photons in a scintillator can be approximated the simplest way by an exponential decay

$$N(t) = \frac{N_0}{\tau} \exp\left(\frac{-t}{\tau}\right) \tag{3.2}$$

with $N(t)$ the number of photons emitted at the time t, τ the decay time of the scintillator and N_0 the total number of emitted photons. But in general a scintillator has a fast (prompt) and a slow (delayed) component, leading to a more complex model

$$N(t) = A \exp\left(\frac{-t}{\tau_f}\right) + B \exp\left(\frac{-t}{\tau_s}\right) \tag{3.3}$$

with the fast component τ_f and the slow component τ_s. The ratio between A and B varies between different scintillators where the fast component usually dominates. The origin of the two constants is discussed in section 3.1.1. Also in the model of eq. (3.3) the rise time has been neglected as it is much shorter than the fast decay time.

A lot of different scintillator materials exist like organic and anorganic crystals, organic liquids, organic plastics and noble gases. For the Mu3e experiment the scintillators used in the fiber tracker and the tile system are organic plastic scintillators that are therefore explained more in detail in the following section.

This section is a brief summary from [28, 46, 49–52] and the lecture slides of [53].

3.1.1 Organic Plastic Scintillators

Organic scintillators are made of aromatic hydrocarbon compounds consisting of benzene ring molecules with the chemical formula C_6H_6. These are fast scintillators with decay times of $\mathcal{O}(\mathrm{ns})$ or even below 1 ns. The only three bonds per carbon atom in the benzene molecule is described by sp^2 hybridized molecular orbitals. The six carbon atom form a covalent σ bond with the hydrogen atom and also two σ bonds with the neighboring carbon atoms. The remaining p orbitals that are not part of the hybridization are the important ones for the scintillation process. Their electrons form a π-bond (fig. 3.1). These electrons in the π-bond cannot be assigned to a specific atom and are therefore called *delocalized*.

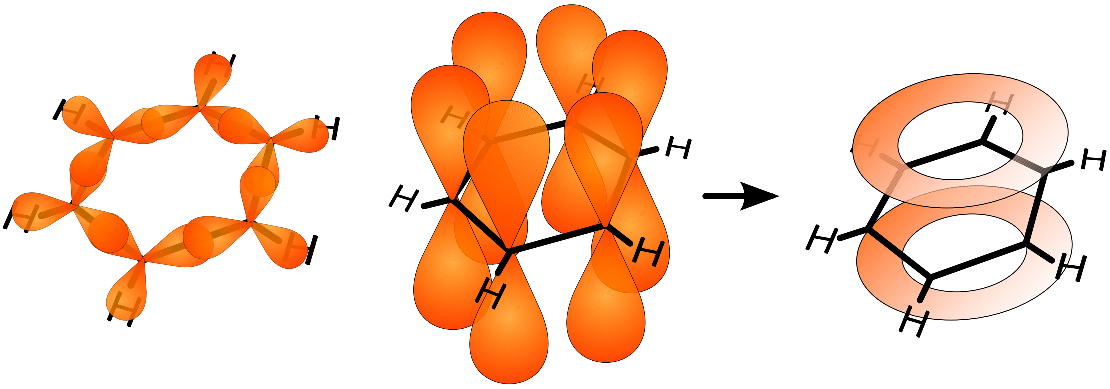

Figure 3.1: The benzene molecule (black) with its molecular orbitals (orange). The σ bonds from the sp^2 hybridized orbitals are shown left. Where the remaining p-orbitals (middle) form a π-bond with delocalized electrons (right). Picture adapted from [54].

The scintillation mechanism arises from these delocalized electrons. The energy levels are visualized in fig. 3.2. The singlet state is called S_0 whereas exited single states are S^*, S^{**}, etc. For the triplet states the ground state is T_0, and the excited states T^*, T^{**}, etc. Each energy state has additional energetic sub levels due to excited vibrational states of the molecule. The energy level between different electron levels is in $\mathcal{O}(\mathrm{eV})$ whereas the energy difference in vibrational states is $\mathcal{O}(1/10\,\mathrm{eV})$. An energy deposit from a charged particle through ionization usually results in excitation of electron and vibrational states. Electron states at levels higher than S^* decay to the S^* state in a very short time ($<10\,\mathrm{ps}$) without the emission of a photon, called the internal degradation. From the S^* state they decay at a time scale of $\mathcal{O}(1\,\mathrm{ns})$, depending on the scintillator, to excited vibrational states in the S_0 level by photon emission. This process is the fast (prompt) scintillation part. The fact that the decay happens not always to the vibrational ground state of S_0 makes a scintillator transparent to its own scintillating light. The emitted photons have lower energies and cannot excite another electron to higher levels. This phenomenon is called *Stockes-shift*.

In the case of the triplet states, excited electrons decay to T_0 via internal degradation. A transition from T_0 to S_0 is suppressed by multi-pole selection rules. The decay of T_0 states usually occurs via interaction of another T_0 state to

$$T_0 + T_0 \rightarrow S^* + S_0 + \text{phonons} \tag{3.4}$$

The decay of the one S^* state is then the same as described above. The longer time scale of the T_0 decay is responsible for the slow (delayed) contribution of the scintillator.

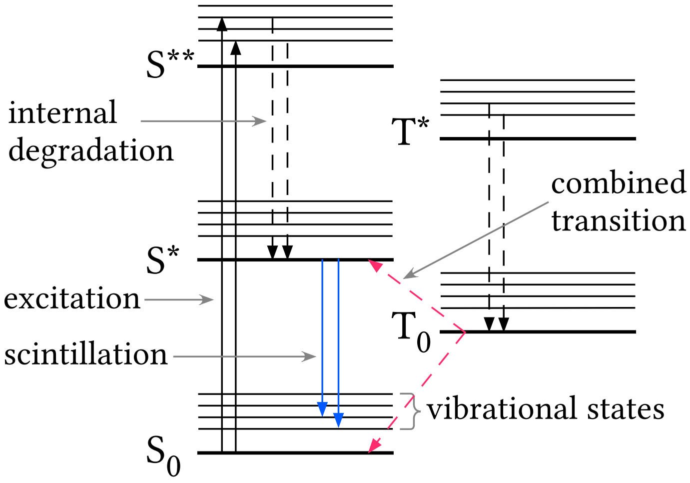

Figure 3.2: Schematics of the energy levels and its transitions of the π-electrons in benzene. Only the blue arrow indicate transitions with the emission of photons. Picture adapted from [53].

Plastic organic scintillators are produced by solving the organic scintillator and mix it with a carrier substance as polyvinyltoluene or polystyrene. These compounds have a typical scintillator molecule concentration of about 10 g per liter carrier substance. This technique allows almost arbitrary shapes of solid scintillators and therefore it is possible to produce them at reasonable prices that makes them very popular also in particle physics.

Plastic scintillators are resistant to water (there are no hygroscopic effects in such scintillators) or low molecular weight alcohols. However, they can be attacked by organic solutions as acetone. Also the grease of human fingers and the acidity in their sweat can destroy the scintillator producing microscopic cracks that causes a significant decrease in the light yield (crazing). Therefore plastic scintillators should always be handled with protective gloves.

The scintillation light of these types of scintillators is often in the UV region or at the blue end of the visible light. Depending on the photonsensor that is used, wavelength shifters need to be added. This wavelength shifters are either added to the solution directly during the production of the scintillators or they are added as additional wavelength shifting light guides.

3.1.2 Scintillator Fibers

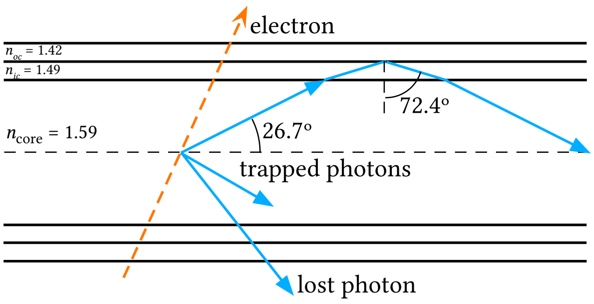

Figure 3.3: Longitudinal cut of a double cladding fiber showing the acceptance angle for total internal reflexion. Picture adapted from [55].

The scintillator fibers introduced in section 2.3.7 are made of a plastic scintillator core. The fibers are not only used as scintillators but also to guide the light to a photon detector (cf. section 3.2.2) that is preferably outside the active area of the experiment. It is the same principle as used for guiding (laser) light in communication fibers. The photons inside the fiber (irrespective whether they are generated within the fiber or coupled in with a laser) travel along the fiber due to total internal reflexion within the core of the fiber and one (or more) claddings with decreasing refractive indices. In most cases in particle physics the fiber consists of a scintillating core made of polystyrene (PS) where the scintillator is added. The refraction index of the core is $n_{\text{core}} = 1.59$. Single cladding fibers have a cladding with a decreased refraction index. Typically this is a polymethyl methacrylate (PMMA) (at $n_{\text{ic}} = 1.49$). A cladding with an even lower refractive index consisting of a fluorinated polymer (FP) (at $n_{\text{oc}} = 1.42$) has been developed more recently that increases the critical angle for total reflexion and therefore the trapping efficiency. Due to bad mechanical stability and increased absorption there are no single cladding fibers with only the PS core and a FP cladding. The FP cladding is only used with double cladding fibers having a PS core, a PMMA inner cladding and a FP outer cladding. Such fibers show an increase in trapping efficiency of about 50 % (fig. 3.3). For an experiment like Mu3e, where 250 µm thin fibers are used, it is important to have a maximum possible photon trapping efficiency.

3.2 Silicon Photon Detectors

This section is a summary of [28, 53, 56]. The conversion of the ionization energy to photons in a scintillator is only the first step of the detection of a particle passage[1]. Unless the experimentalists do not use their bare eyes (cf. section 3.1) the photon signals need to be converted to an electrical signal with a proper analog to digital (ADC) conversion. Measuring faint photon signals, especially in the case of single photon signals, demands a detection device with a high quantum efficiency (qe). The signal needs to be amplified to a level that allows it to be transported to the ADC and to make use of the full sensitivity range of the ADC.

For low photon fluxes the photomultiplier tube (PMT) is the most elaborated device. However, these devices cannot be used for the Mu3e detector as explained in section 2.3.7. Fortunately, there is a fast development in the design of solid state detectors with high quantum efficiencies and sensitivities at single photon levels.

Even though there is a huge variety of solid state sensors, almost all are based on the same principle as explained in the following sections. Solid state photon detectors are made from semiconductor materials (e.g. silicon). Their properties bring different advantages to particle physics. Due to the high material density of such devices, charged particles deposit a lot of energy after passing a short path. Solid state detectors can therefore reach a spatial resolution below 10 µm. The technique and materials to produce semiconductor devices are the same as used in the design for microprocessors. It makes the devices relatively cheap to produce. As in the example of the HV-MAPS it makes it even possible to combine the detectors and readout electronics on the same integrated circuit die emerging a new class of highly integrated devices. This section explains the working principle of silicon sensors focusing on photon detection.

3.2.1 General Working Principle

Different sensor types exist that can be used to detect photons. They usually have a common working principle. Such sensors employ two layers of silicon where one has a p- and the other one a n-dopant, which are in contact to each other leading to a *p-n-junction*. Electrons from the n-dopant layer can recombine through diffusion with holes from the p-dopant layer. The doping atoms are fixed in the crystal structure and do not move. Close to the contact region there will be left a positive charge in

---

[1] As long as not stated otherwise the principles can be used for timing- and tracking-detectors. The usage is given by the scintillator geometry and the way of data digitization.

the n-dopant layer and a negative in the p-dopant[2]. An electric field emerges due to the remaining charge of the fixed atoms that counteracts to the diffusion of the free moving charges until an equilibrium is reached. The area where there are no free moving charge carriers left is called *depletion region* (fig. 3.4). This configuration is called a semiconductor diode.

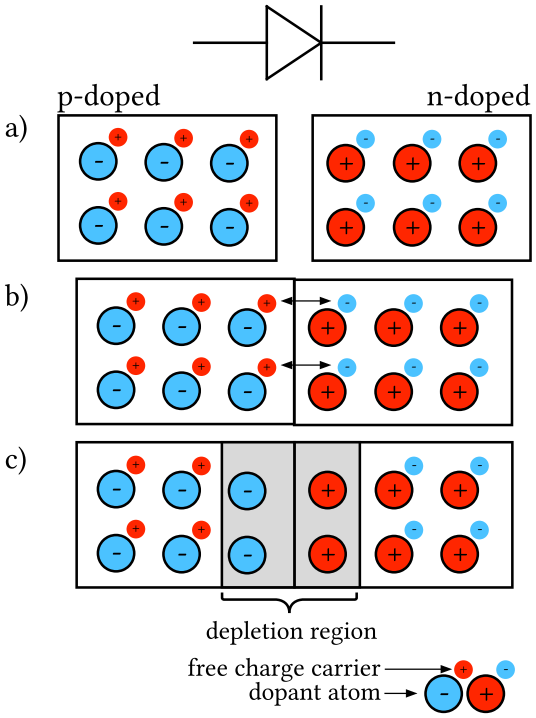

Figure 3.4: Schematics of a p-n-junction. *a)* shows a p- and an n-doped semiconductor. *b)* When the two semiconductors get in to contact, electrons and holes recombine until an equilibrium is reached *c)*.

All sensors have in common that an external field is applied in reverse direction. It widens the depletion region and the active volume of the sensor increases. In the active area electron-hole pairs can be produced either by ionizing particles or due to the photoelectric effect by photons. These pairs drift within the electric field to the electrodes at the detector and produce a current. Generating an electron-hole pair needs to overcome the band gap of the used semiconductor. For silicon it is 1.12 eV, leading to a natural limit in photon detection for wavelengths shorter than about 1110 nm. Thermal excitations of electron-hole pairs contribute to the current in the sensors and are an important source of noise. Thermal noise is in particular a problem for high

---

[2] The overall charge of the junction stays of course neutral, whereas there are local changes in the charge density

sensitive detectors where single photons need to be detected. This will be discussed in further details in the next section and in section 6.3.1.

A simple example of a semiconductor photon detector is the PIN[3] diode (fig. 3.5). This diode consists of a strongly p- and n-doped layer with an undoped (intrinsic) or weakly doped silicon in the middle. With the intrinsic silicon the depleted volume can be enlarged at still moderate bias voltages. The principle is exactly the same as described above. Due to the photoelectric effect, electron-hole pairs are generated that travel to the electrodes. The advantage of such a device is that the signal is directly proportional to the photon current it is exposed to. However, as there is no signal amplification within the detector, a detection of single photon events is nearly impossible.

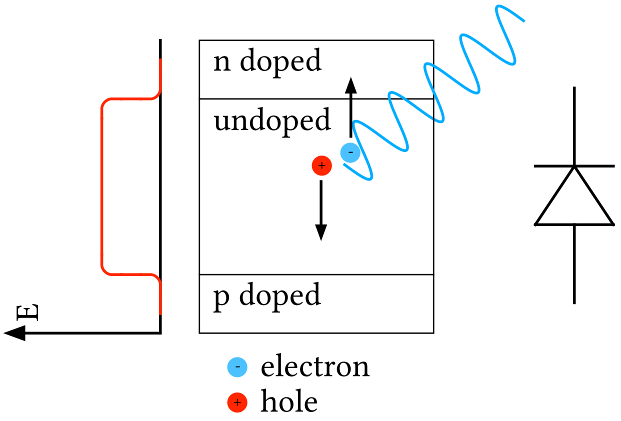

Figure 3.5: Schematic of a PIN diode. The electron and the hole drift within the applied electric field to the edges of the sensor. Picture adapted from [28].

Avalanche photodiodes (APD) are sensors similar to the PIN-diodes. But the doping profile differs. Instead of an intrinsic Si layer the APD has a lightly p-doped volume in the middle (fig. 3.6). Such a device is mainly divided in a collection area and an amplification area. Electron-hole pairs are produced in the collection area whereas an avalanche process starts only at the high field gradient produced at the p-n-junction. The electrons can produce other electron-hole pairs by impact ionization in the high gradient area. The secondary electrons can again produce electron-hole pairs and an avalanche starts. As seen with the PIN-diode the electrons propagate to the anode and the holes to the cathode respectively. It is important to emphasize that in an APD the bias voltage is chosen to a level that only the electrons and not the holes produce avalanches. The bias voltage is therefore below the *breakdown* level. The avalanche

---

[3] three Si-layers, p-doped, intrinsic, n-doped → PIN

propagates therefore only to one side of the detector and stops after all electrons have reached the electrode. The avalanche amplifies the signal of the first electron-hole pair (typical APD gains are within a range of about 10 to 1000) making it possible to detect low signals of about only 10 photons [49]. The APD is still a linear device where the signal generated by the device is proportional to the photon flux. For the Mu3e fiber detector even more sensitive devices are needed and a single photon sensitivity is demanded.

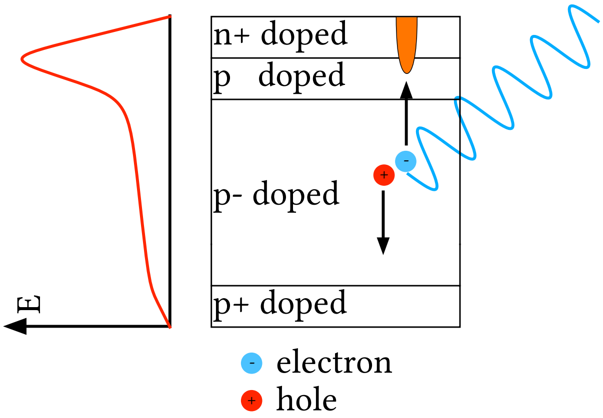

Figure 3.6: Schematic of an APD. The electrons start an avalanche in the high electric field of the p-n-junctions while the holes propagate to the opposite site without inducing an avalanche. Picture adapted from [28].

A special form of the APD, the *Geiger mode APD* (GAPD) can be used to detect single photons. The GAPD is an APD with a bias voltage above the breakdown level. With the increased bias voltage not only the electrons but also the holes produce avalanches propagating to the cathode by generated secondary electron-hole pairs. As the secondary pairs can produce new pairs a diverging avalanche multiplication starts and high currents occur (i.e. the *Geiger discharge*). The GAPD requires a quenching mechanism to stop the avalanches as the gain would reach infinity and, even more important, to get the system ready for the detection of a new event. The easiest way is to use a quenching resistor in series to the GAPD. As soon as there is a large avalanche current, the bias voltage drops at the quench resistor leading to a field small enough that no new electron-hole pairs are generated. The avalanches stop and the sensor gets ready again to detect a new event. The detailed working principle and an electronic equivalent circuit is discussed in section 5.2 where the signal that is produced by such a device is simulated. Quenching of a sensor can also be done by active electronics. In this case the bias voltage will be reduced below the breakdown voltage of the device and increased again after a specified time. This form of *active quenching* is interesting when fast sensors are needed that can deal with high rates. The disadvantage of an active quenching is the additional electronic and logic that needs to be implemented.

GAPDs have large gains of $\mathcal{O}(10^6)$ that makes them very powerful devices to detect small photon fluxes. It is even possible to detect single photons with such devices. Due to the Geiger discharge the signal produced in the sensor is not dependent on the photon flux anymore. One implication is that the device is a binary unit: light yes or no. It makes the discrimination between thermal noise and events where actually photons were detected impossible, as both show the same signal. A solution to this problem is discussed in the following section.

3.2.2 Silicon Photomultipliers in Detail

Silicon photomultipliers (SiPMs)[4] are devices that unify the high gain and sensitivity of APDs driven in Geiger mode and a dynamic response to the photon flux. SiPMs are highly integrated silicon devices consisting of a two dimensional array of APDs operated in Geiger mode. Each individual pixel of such an array is still a binary device. But with the assumption that the photons are distributed over the whole array, the device gets a dynamic response. Figure 3.7 and fig. 3.8 show a simplified schematic of a SiPM. Each pixel is shown as a diode and has its own quenching resistor. The signal of each pixel is added analogously. As a result the SiPM device responds linearly to the number of pixels fired.

Even though the response is linear to the number of fired pixels, an ideal SiPM with a 100 % quantum efficiency per pixel will not show a linear response to the photon flux over the whole dynamic range[5]. With higher photon intensities the probability increases that a photon hits a pixel that has already been hit by another photon. As the pixel themselves are in Geiger mode it does not detect the second photon. The number of pixels fired N_{fired} (with still ideal efficiencies) gets therefore

$$N_{\text{fired}} = N_{\text{pixels}} \cdot \left(1 - \exp\left(-\frac{N_{\text{photons}}}{N_{\text{pixels}}}\right)\right) \tag{3.5}$$

with N_{pixels} the number of pixels in a device and N_{photons} the number of photons hitting the active area of the device. With the small light intensity expected in the fibers for Mu3e, this effect can be neglected.

Nevertheless the SiPM still suffers form thermal noise. In contrast to single GAPDs the SiPM can clearly distinguish between events with several photons and the thermal

---

[4] also called multi-pixel photon counters (MPPCs)

[5] The dynamic range is specified by the number of pixels a SiPM provides

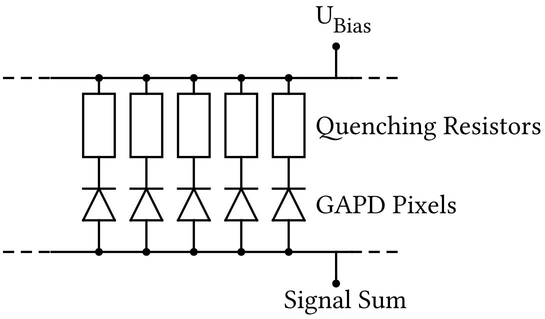

Figure 3.7: Simplified schematics showing the principle of summing up individual GAPDS to a SiPM with a dynamic response to the photon flux.

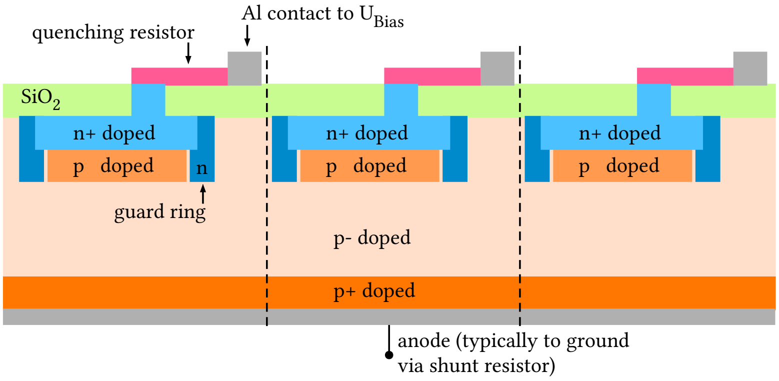

Figure 3.8: Schematic cross section of the doping layers in a SiPM. Three pixels are shown where each forms a GAPD. Newer models have also an optical isolation (trenches) between the pixels to reduce optical crosstalk. Picture adapted from [57].

noise. At a single photon threshold the SiPM suffers from the same problems as a GAPD. Current state of the art SiPMs have thermal noise rates[6] at $\mathcal{O}(100\,\mathrm{kHz})$[7] at single photon level. This value depends on the temperature and the bias voltage. The typical pixel sizes of SiPMs are between $25 \times 25\,\mu\mathrm{m}^2$ and $100 \times 100\,\mu\mathrm{m}^2$. One single device can cover active areas up to $6 \times 6\,\mathrm{mm}^2$ (fig. 3.9).

An important value for SiPMs is the *photon detection efficiency* (PDE) [58]. The PDE includes the quantum efficiency that depends on the average number of electron–hole pairs created by the photon in the sensor. Losses at the entrance window due to reflection or absorption lowers the PDE. The effective area of a SiPM is smaller than the specified active area as there is dead area between pixels in the sensor. Furthermore the breakdown probability, stating the probability that a single electron (or hole) can trigger a breakdown, can be smaller than 1. This depends highly on the electrical field

---

[6] also called dark count rates

[7] at room temperature and nominal bias voltage

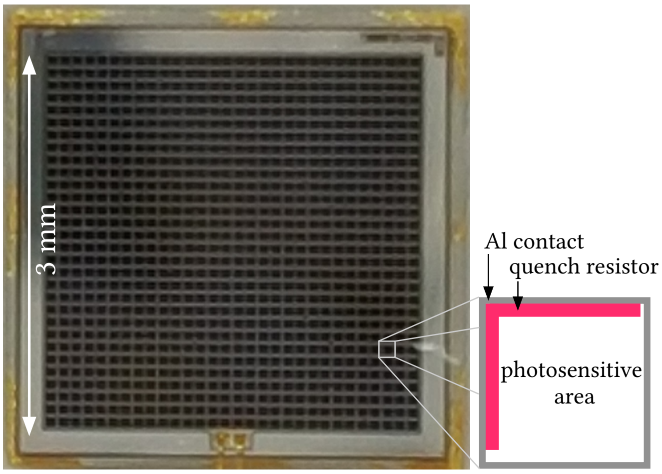

Figure 3.9: Picture of a 3 × 3 mm^2 SiPM (left). The schematic on the right shows one pixel from top with the electric metal contact, the quench resistor and the active area covered by SiO_2.

strength at the junction of the pixel. After a breakdown the pixel needs a certain time (typically $< 1\,\mu\mathrm{s}$, depending on the quench resistor and the capacity of a single pixel) to recover and be ready again (cf. section 5.2). Due to background light or thermal noise pixels may not be not ready for a detection as they are in the recovery state. Operation conditions should be chosen in such that not more than 1 % inefficiency occurs. A good shielding of the ambient light and a cooling the device to reduce the thermal noise are therefore important.

4

Fiber Simulation

The Mu3e experiment invests a lot of effort to develop a detailed framework to simulate the whole detector. As in every experiment a lot of research and development can already be done on a simulation level without the real detector or even only a few prototypes working. The more detailed knowledge is available for the detector modules, the more can be implemented into the simulation. Also the fiber part of the detector needs to be implemented to the main simulation. But having a full optical simulation for thousands of fibers with $\mathcal{O}(1\,\mathrm{MHz})$ occupancy would be extremely computing-power and memory intensive. And — as soon as the optical properties are fully understood — there is no interest anymore how the photons propagate inside the fiber. The only information needed is the amount of photons that arrive at the fiber end and their distribution in time.

In parallel to a simulation framework for the whole detector, a dedicated fiber simulation has therefore been developed. The dedicated fiber simulation copes with the optical propagation and distribution of the photons within the fiber for a small amount of fibers. With the results generated from dedicated simulations, a parametrization has been implemented for the main simulation. In this chapter such a dedicated simulation of the fibers optics is discussed as well as a parametrization of the results that has been implemented in the main simulation covering the whole detector. The baseline for all simulations is the Kuraray SCSF 81 multi cladding fiber with a diameter of 250 µm [55].

All simulations have been developed in Geant4 [59, 60]. Geant4 is a toolkit written in C++ used to simulate the passage of particles through matter. It can be used for tracking, production of daughter particles, simulating detector responses by implementing arbitrary geometries of materials. The materials can be implemented as desired for a custom detector, including density, chemical composition and also, in particular needed for this thesis, optical properties like refraction indices, attenuation length and non-perfectly smooth surfaces. The Geant4 modular principle allows also to decide which information of an event is stored.

An event is in general the timespan between the spawn of a particle with a given momentum until the particle itself, or all its daughter particles reach the end of the implemented *world* volume, or their energy go below a specified threshold. The world consists of the materials themselves and, if needed, from external applied electric and magnetic fields. The materials within the world (the *daughter volumes*) can be placed either by using basic geometrical shapes (e.g. cylinders, cubes, spheres) or by defining more complex structures with boolean operations from the basic shapes (e.g. cutting out a cylinder from a cube). For each daughter volume it can be decided whether the particle(s) should just pass them with the proper particle-matter physics of interaction or whether data during the passage needs to be written out. Such data can be the coordinates (position within the detector as a function of time) of the particle during its propagation, where it entered a specific volume, how many daughter particles have been produced or how much energy has been deposited within the volume.

In addition, Geant4 uses the concept of *optical photons* implemented as the “G4-OpticalPhoton” class. It is used in the case when the wavelength of the photon is much larger than the atomic spacing of the matter. The optical photon class uses the wave like nature of electromagnetic radiation and is therefore different to the “G4Gamma” class implementing high energy photons. The distinction is insofar important than there are no smooth transitions between those two objects, and optical photons will not count to the energy budget of an event in Geant4. The principle of the simulation can be summarized as simulating the energy deposit of a charged particle (e.g. an electron) in the active part of the fiber, producing the corresponding amount of scintillating photons along the particle path and propagating them along the fiber where their temporal and spacial distribution when they reach the end of the fiber is stored in a data file.

4.1 Software Framework

The dedicated simulation tool written for the fibers is designed with the idea to be very flexible. As several parameters of the fibers were not known, the idea was to run different simulations in parallel. With the help of an easy understandable configuration file different scenarios can be simulated. This includes single fiber examination, arbitrary ribbon configurations, different ambient materials like glue, helium, vacuum and an additional titanium dioxide coating for the fibers (table 4.1).

Table 4.1: Configuration parameters available for the dedicated fiber simulation. The corresponding dimensioning in case of manual staggering is shown in fig. 4.1.

Parameter	Description	Values
fibertype	type of fiber	1 = round fiber double cladding 2 = squared fiber single cladding 3 = scintillator rod 4 = BCF10 single Cladding
perfectSurface	perfectly polished surface	boolean
useTiO$_2$	additional TiO_2 coating	boolean
fiberLength	length of the fiber	in cm
fiberDiameter	diameter of the fiber	in mm
Ncolumns	number of columns for ribbons	integer
Nrow	number of rows for ribbons	integer
interfiberDist	distance between fibers	mm
sensorGap	gap between fibers and SiPM	mm
worldMaterial	material of the fiber surrounding	1 = epoxy glue 2 = POM 10 = Air
useManualStaggering	switch for special fiber ribbons	boolean
xStep	if manual staggering: x pitch of fibers	mm
yStep	if manual staggering: y pitch of fibers	mm
staggerShift	offset between two layers of fibers	mm

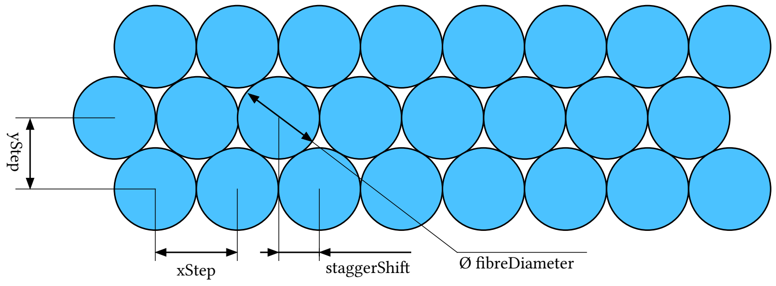

Figure 4.1: Dimensioning if manual staggering is configured for the fiber simulation (cf. table 4.1.)

For a deeper understanding of all processes the simulation has been implemented in such a way that different steps can be read out individually. This means that in a first step the number of photons reaching the fiber end has been recorded and—if needed—also how many photons would reach a SiPM detector. This approach allows to analyze potential photon losses and helps to improve the setup. For a systematic analysis of the fiber photon response, electrons and positrons with momenta of 15 MeV/c to 53 MeV/c are simulated.

As discussed in detail in section 6.5 the results have been compared to measurements done at the Paul Scherrer Institute. Therefore the simulation also offers the option to simulate beam conditions as used during the testbeams there.

4.2 Materials

The Kuraray SCSF-81M fiber is built exactly from the materials as described in section 3.1.2. The fiber diameter is 250 µm including both claddings. Each cladding layer has a thickness T of 3 % of the fiber diameter (fig. 4.2). The first (inner) cladding is polymethyl methacrylate (at $n_{\text{ic}} = 1.49$) and the outer cladding consists of a fluorinated polymer (at $n_{\text{oc}} = 1.42$).

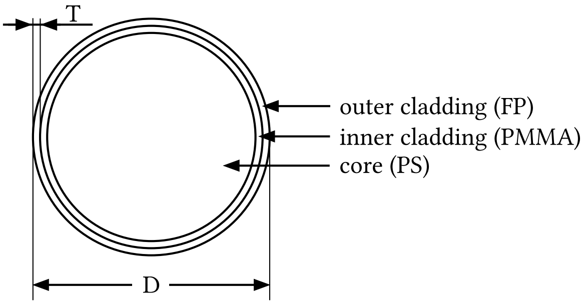

Figure 4.2: Cross-section of a Kuraray SCSF-81 multi cladding fiber [55]. The schematics has the actual scale.

The simulation implements the fiber with all layers. The polystyrene core is implemented as defined in the Geant4 material database [61] based on [62] as G4_POLYSTYRENE. It is a $(C_8H_8)_n$ polymer chain with a relative mass distribution of 92 % carbon and 8 % hydrogen. The refraction index is implemented wavelength independently as $n_{\text{core}} = 1.59$. The scintillating light of the fiber is produced in the core. The spectrum of the scintillating light is implemented as shown in fig. 4.3.

The amount of photons generated by the Geant4 simulation depends on the energy deposited in the material. For the fiber core it is defined as 8000 photons per MeV deposited energy [63]. The Birk's law as described in section 3.1 is also implemented in the simulation. As the light yield is not yet specified by Kuraray, the value is taken from a similar product produced by Saint-Gobain. The Saint-Gobain fiber core consists of the same material as the Kuraray fibers and therefore the scintillation yield is assumed to be the same for both types. From this number Geant4 calculates the mean photon yield for a particular event. In addition there is a statistical fluctuation using a Gaussian distribution with mean μ_{py} mentioned before and a standard deviation of the photon yield $\sigma_{\text{py}} = \sqrt{\mu_{\text{py}}}$. The photons are emitted isotropically along the path of the particle.

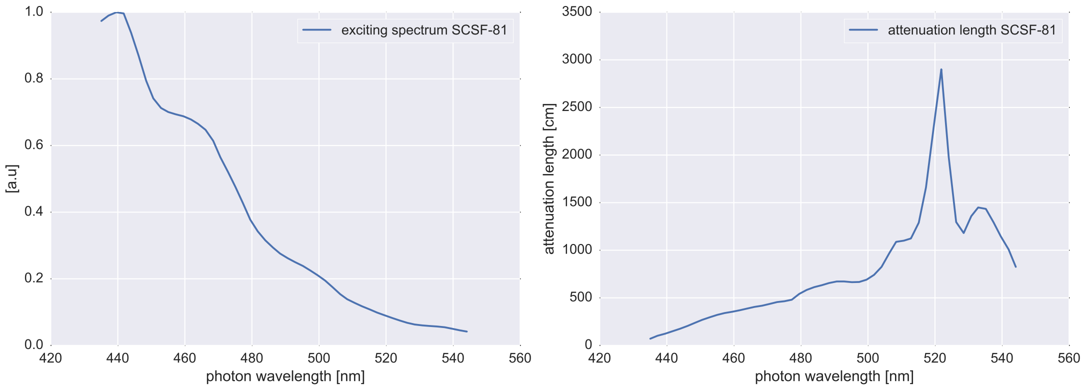

Figure 4.3: Emission spectrum *(left)* of the SCSF-81M round multi cladding fiber and the absorption spectrum *(right)*. Adapted from [55].

Geant4 calculates the energy deposit within a limited step resolution. Usually Geant4 automatically calculates the number of steps done in a specific volume. For such small geometries it turned out that Geant4 does only one step within the fiber. This step is done at the geometrical boundary (i.e. between the cladding and the fiber core). To avoid the production of scintillating light only at the fiber border, the step width has been set manually to a maximum of 1/10 of the fiber core diameter (fig. 4.4).

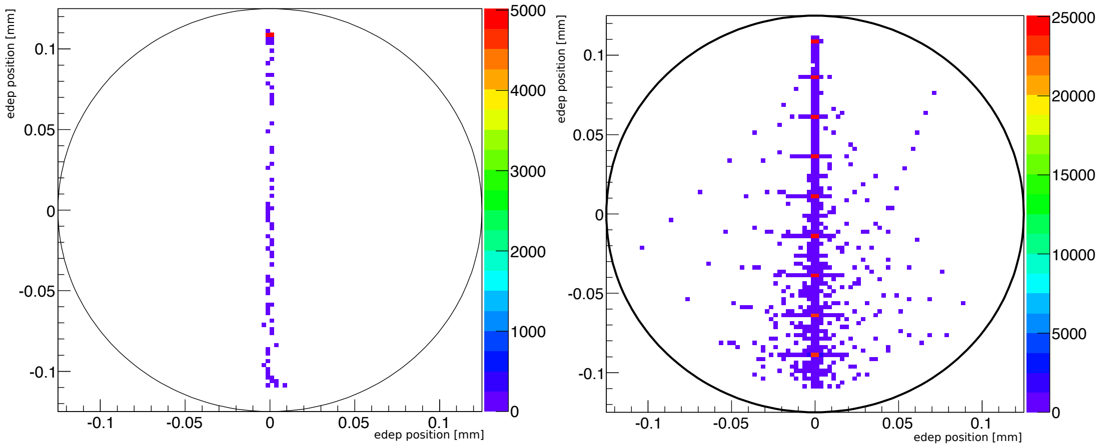

Figure 4.4: Comparison of the Geant4 step with. The pictures show where the electron deposits energy within the fiber. The left picture shows the default behavior and the right picture a step width not larger than 1/10 of the geometry width. Deflection due to multiple scattering are also visible now.

Transporting the generated photons depends on reflexion, scattering at boundaries of surfaces, and absorption within the medium. The absorption length is implemented for the core material as defined in the datasheet. The implementation of the surfaces is more complicated. Geant4 provides different ways to model surfaces. The most important value to understand optical processes in Geant4 is the radiant intensity $\mathcal{J}$, defined as the photon flux $\mathrm{d}\Phi$ passing through the solid angle $\mathrm{d}\omega$ leading to $\mathcal{J} = \mathrm{d}\Phi / \mathrm{d}\omega$ [64]. For an ideal polished surface of two transparent media the radiant intensity $\mathcal{J}_P$ is given by

$$\mathcal{J}_P := \left[R(\theta_i, n_1, n_2)\delta(\theta_i - \theta_r) + T(\theta_i, n_1, n_2)\delta(\theta_t - \theta_s)\right] \delta(\varphi_r) \tag{4.1}$$

with

- n_1 – the index of refraction of the incident medium,
- n_2 – the index of refraction of the transmission medium,
- θ_i – the angle of incidence relative to the average normal,
- θ_r – the angle of reflection with respect to the average normal,
- θ_t – the angle of refraction with respect to the average normal,
- $\theta_s = \sin^{-1}\left(\frac{n_1}{n_2}\sin(\theta_i)\right)$,
- φ_r – the angle between the projection of the reflected or refracted photon onto the average surface and the plane of incidence.

R and T describe the reflexion and transmission coefficient. For the surface between the fiber core and the first cladding as between the first and the second cladding the model has been extended by micro facets (fig. 4.5). For each optical photon reaching the surface, an effective angle is calculated assuming a Gaussian distribution of the angle with a standard deviation of σ_α around the angle that is given by the geometrical orientation of the surface (called the average angle). Defining the σ_α an arbitrary roughness between two surfaces can be specified. The radiant intensity with micro facets $\mathcal{J}_m$ is then

$$\mathcal{J}_m := R(\theta_i', n_1, n_2)g(\alpha; 0, \sigma_\alpha) + T(\theta_t', n_1, n_2)g(\alpha; 0, \sigma_\alpha) \tag{4.2}$$

with the additional parameters

- θ_i' – the angle of incidence relative to the micro-facet normal,
- θ_t' – the angle of refraction with respect to the micro-facet normal,
- α – the angle between a given micro-facet and the mean surface,

- $g(\alpha; 0, \sigma_\alpha)$ – the Gaussian distribution with mean 0° and the standard deviation σ_α.

It is not easy to estimate the proper value of σ_α for the surface between the core and the claddings. Often it is empirically tested using different values and comparing it to measured results. As the simulation needed to be ready before the actual fiber ribbons were available the value has been estimated to be 0.31° as proposed by [65]. How well this value agrees with the measurement is discussed in section 6.5.2.

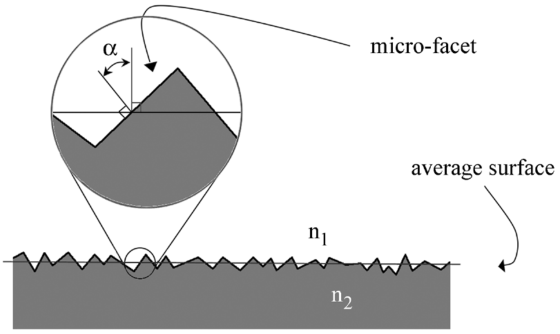

Figure 4.5: Definition of the surface quality in the unified model. The standard deviation of the angle distribution of the micro-facets around the surface normal is defined as σ_α. Picture taken from [65].

In the case the simulation needs to simulate an additional Titanium Dioxide (TiO_2) coating, the coating is placed between the outer cladding and the surrounding of the fiber[1]. Equation (4.2) needs to be extended to the so called UNIFIED model $\mathcal{J}_U$ that can be approximated with

$$\begin{aligned} \mathcal{J}_U &\approx R(\theta_i', n_1, n_2)[C_{sl} g(\alpha; 0, \sigma_\alpha) \\ &+ C_{ss}\delta(\theta_i - \theta_r)\delta(\varphi_r) \\ &+ C_{bs}\delta(\theta_i - \theta_r)\delta(\varphi_r) \\ &+ C_{dl}\cos(\theta_r)] \\ &+ T(\theta_t', n_1, n_2) g(\alpha; 0, \sigma_\alpha) \end{aligned} \tag{4.3}$$

with the coefficients

- C_{sl} – the specular lobe constant that controls the probability of specular reflection about the normal of a micro-facet
- C_{ss} – the specular spike constant that controls the probability of specular reflections about the average normal of the surface

---

[1] the surrounding can be the epoxy glue or air

- C_{bs} – the backscatter spike constant that controls the probability of backward reflection
- C_{dl} – the diffuse lobe constant that controls the probability of internal Lambertian reflection

controlling arbitrary surfaces (cf. fig. 4.6). The sum of the four coefficients C_i needs to be 1. The UNIFIED model includes the previous model: setting $C_{sl} = 1$ and the other coefficients to zero the model simulates a rough surface between two transparent media as shown in eq. (4.2).

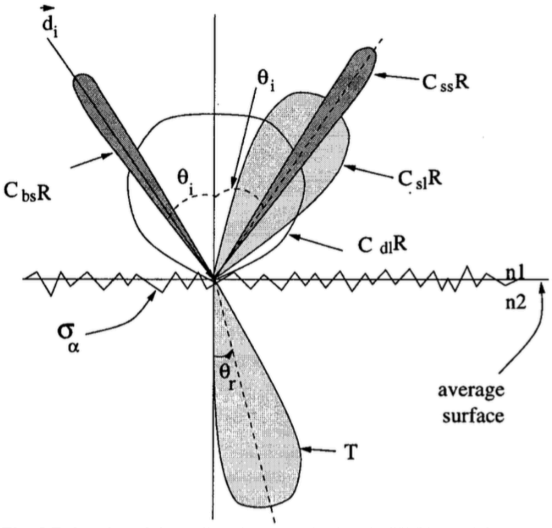

Figure 4.6: The additional coefficients in the UNIFIED model C_i. Picture taken from [64].

The challenging part is finding the proper coefficients for equation 4.3 to simulate a proper TiO_2 coating. But due to the long distance of the fiber, a proper modeling of the surface is crucial to get useful results. In [66, 67] a detailed study of different measurements are performed using a laser that irradiates different surfaces as TiO_2, Teflon, and others on different surface roughnesses. The reflected light is measured with an array of photodiodes. These measurements show that the assumption that the four coefficients are independent of the incident angle is actually wrong [67]. The results from these measurement with different surface roughnesses are provided in Geant4 as a look-up table (LUT) providing more accurate results [65]. For each photon that reaches a surface that is implemented by using the LUT, the photon incident angle is rounded to the next integer value. The LUT provides a probability distribution for the reflecting angle for each integer incidence angle. From this probabilities a new direction of the reflected photon is calculated. For the simulation of a TiO_2 coating this approach was used.

4.3 Single Fiber Analysis

4.3.1 Photon Yield Parametrization

For the simulation covering the whole experiment a detailed analysis of the fiber response has been performed. In this scenario one TiO_2 coated fiber was placed in a helium environment.

Figure 4.7 right shows the photon yield as a function of the deposited energy when a 36 cm long fiber is crossed in the middle (i.e. at coordinate $z = 0$ as shown in fig. 4.10). The fiber thickness is negligible compared to its length. The amount of photons that reach the end of the fiber therefore depends only on the energy deposit and where along the fiber the particle crossed. Nevertheless an offset crossing of the fiber causes less light. This effect is due to less energy deposit as the path in the scintillator material gets shorter (fig. 4.7 left). An energy deposit dependent analysis takes this effects into account.

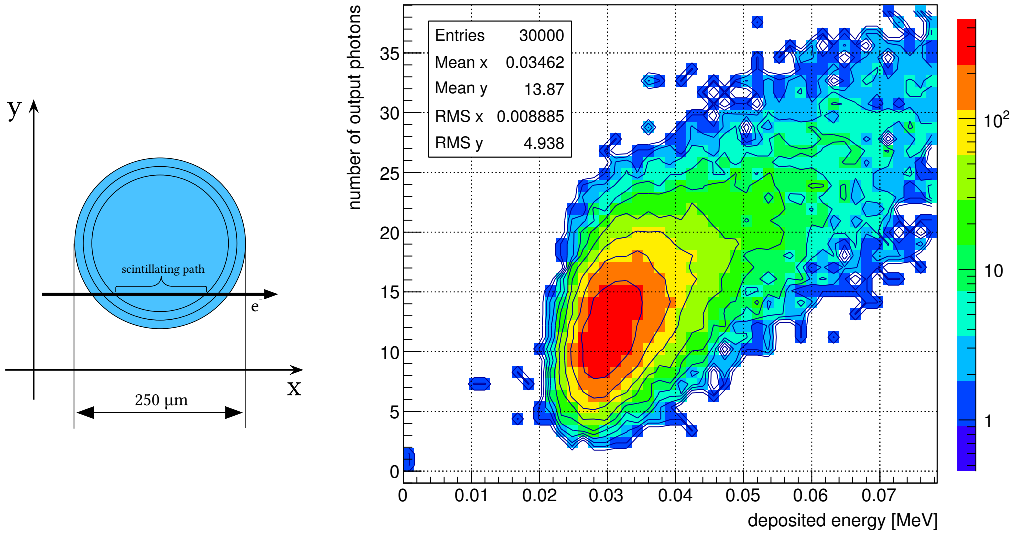

Figure 4.7: Left: Definition of an offset crossing event. In this case the electron crosses the fiber off center concerning the x-y-plane. Right: Light yield of a single TiO_2 coated fiber. The figure shows the number of photons reaching one fiber end when the fiber is crossed by a 15 MeV c^{-1} positron.

Figure 4.8 shows the spacial distribution of the photons at the fiber end. The photons mainly travel along the fiber border. This has important implications for the alignment of the fiber to the SiPM. Therefore the area of the SiPM has to be at least as large as the fiber cross section itself. The expectation that this might reduce the dynamic range of the SiPM, as the probability to hit the same cell several times increases is not justified as the number of photons is reaching the sensor is expected to be small. More important is the angle of the photons leaving the fiber.

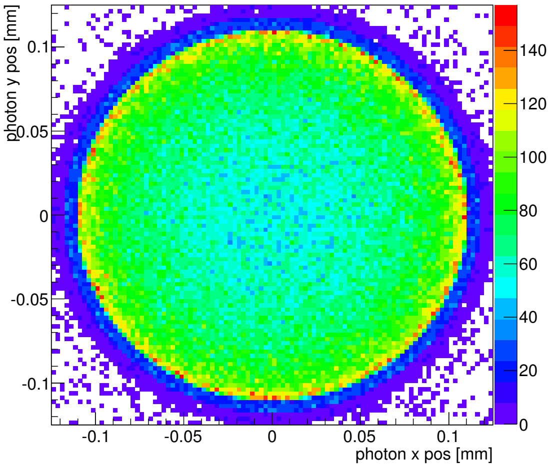

Figure 4.8: Distribution of the expected photons at the end of the fiber.

Figure 4.9 shows that the photons leave the fiber with an angle of $(14 \pm 1)^{\circ}$. As the SiPM might touch the fiber perfectly and that there is typically an epoxy resin that covers the sensor itself, the sensor should be even larger than the fiber.

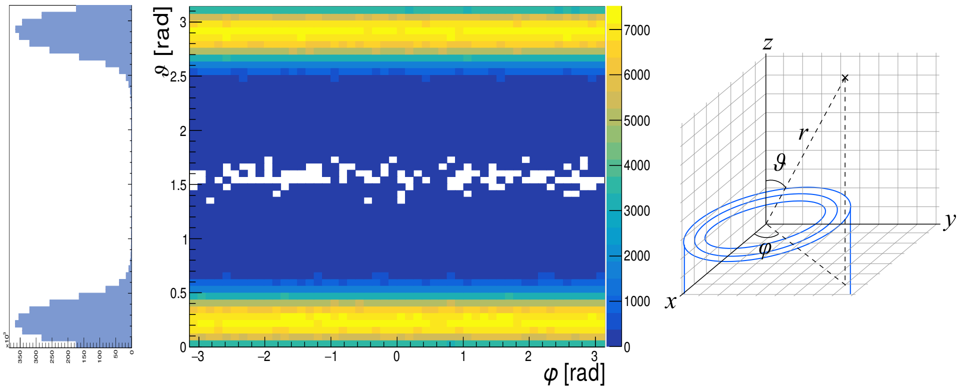

Figure 4.9: Left: Distribution of the angles under which the photons leave the fiber. In this plot there is no change of refractive index at the fiber end. Right: The definition of the angles relative to the fibers.

For an effective parametrization the simulation has been performed for particle crossings at z-coordinate 0 cm, 2.25 cm, 4.5 cm, 6.75 cm, 9 cm, 11.25 cm, 13.5 cm, 15.75 cm and 17.99 cm seen from the fiber center (cf. fig. 4.10).

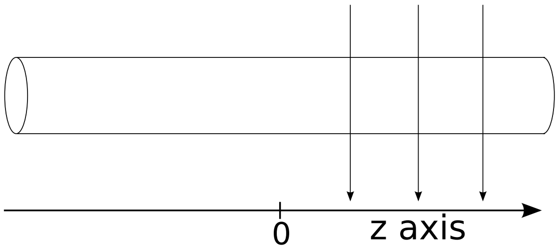

Figure 4.10: Definition of the z-coordinate of the fiber. $z = 0$ is defined in the middle of the fiber.

At each position 10 000 fiber crossing events and the number of photons that reached the fiber end were recorded. The mean photon yield depends about linearly on the energy deposit. An example of the photon yield for a specific energy deposit bin is shown in fig. 4.11. For each slice in the energy deposit the distribution was assumed as Gaussian and the mean μ and width σ were calculated. In a second step the means of the Gaussians versus the energy deposit were fitted as a straight line (fig. 4.12). The slope of this line was plotted in dependence of the particle crossing positions along the fiber. The dependency of the slope is assumed to be a double exponential, see fig. 4.13. The first exponential dependency comes from the absorption along the fiber where the second one is due to the fact that if the crossing of the particle is close to a fiber end there is also *direct light* visible that would not be trapped by the fiber (i.e. no total reflexion within the fiber). The fit values can be parametrized dependent on E_{dep} in MeV c^{-1} and the z-coordinate in cm:

$$\begin{aligned}\mu(E_{\mathrm{dep}}, z) =& E_{\mathrm{dep}} \cdot (\exp(6.90 - 0.05z) + \exp(8.61 - 1.00z))\\ \sigma(E_{\mathrm{dep}}, z) =& E_{\mathrm{dep}} \cdot (\exp(4.46 - 0.03z) + \exp(4.99 - 1.05z))\\ &+ \exp(1.61 - 0.56z) + \exp(0.92 - 0.02z)\end{aligned} \tag{4.4}$$

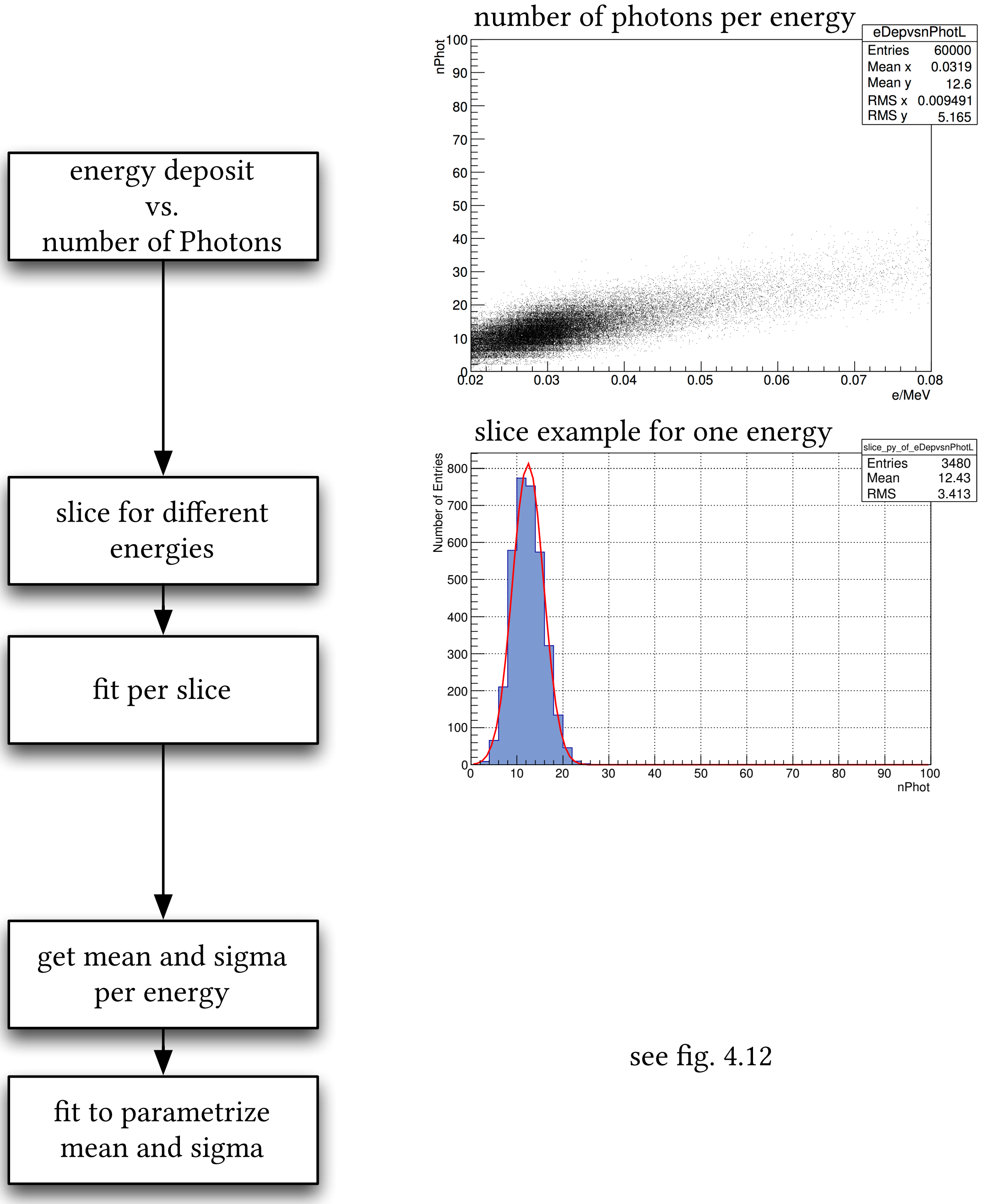

Figure 4.11: Schematic work-flow for the parametrization build for the main simulation. Slices for different energies yield to a mean and width in the number of photons distributions per slice. The mean and width can then be parametrized by linear fits as shown in fig. 4.12.

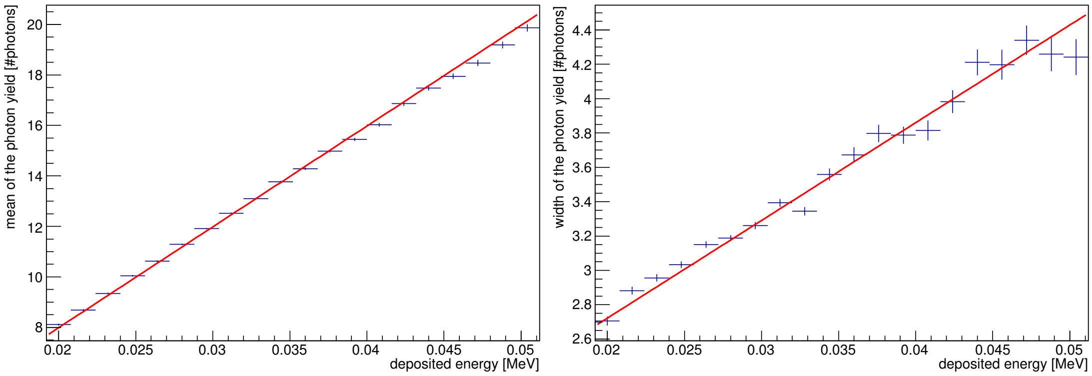

Figure 4.12: Mean (left) and width (right) of the Gaussian photon yield distribution versus the energy deposit at the fiber crossing distance of 18 cm. The parametrization of both fits is shown in eq. (4.4)

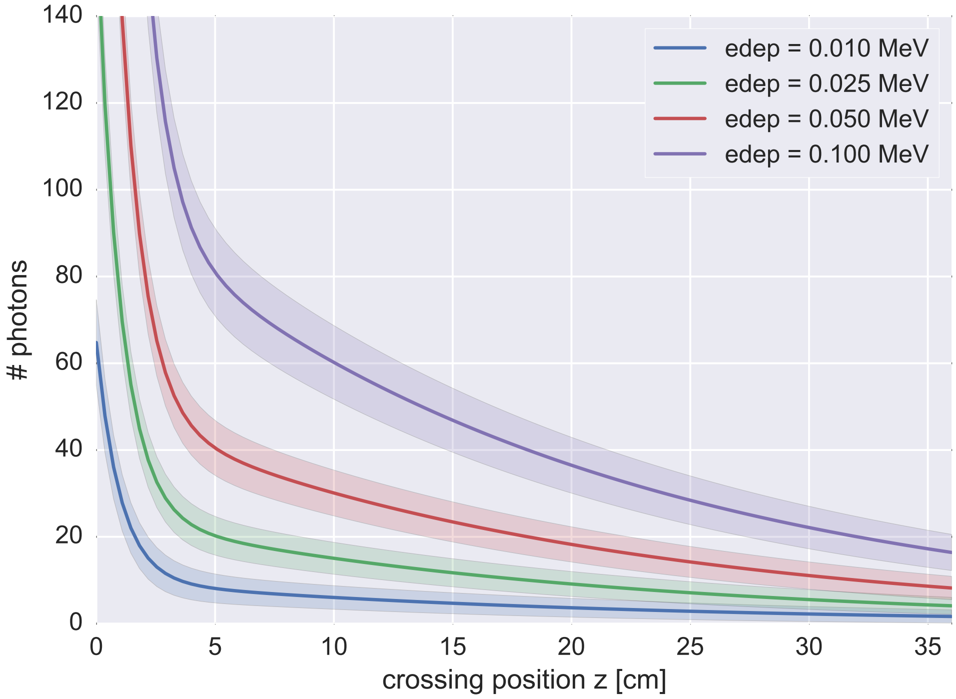

Figure 4.13: Dependency of the photon yield at the fiber end along the fiber as a function of the crossing point z-coordinate. Each line represents a specific energy deposit with a 1σ error band.

4.3.2 Implementation of the Parametrization in the Main Simulation

The scintillator fibers are also implemented in the main (detector) simulation. The implementation includes the detailed geometries of the fibers, i.e. the fiber core, the first and the second cladding. As there is no generation and propagation of the optical photons in the main simulation, the parameters surface roughness, scintillation spectrum and the type of the coatings are not needed to be implemented here. The glue that is used to build the fiber ribbons is implemented as it contributes to the material budget.

To keep the main simulation also as flexible as possible, a hit in the fiber has been processed in several steps. In a first step the energy deposit E_{dep} of a crossing particle is summed up for each fiber it traverses. With E_{dep} the number of photons at both fiber ends is calculated using the parametrization in eq. (4.4). This is done for all fibers in an event.

In a next step optical crosstalk can be enabled. For each fiber the number of photons in the surrounding fibers are calculated. With a crosstalk probability that can be specified in the simulation the number of additional crosstalk photons is calculated. The optical crosstalk photons are then added to the number of photons generated by the fiber itself. Using the final number of photons, the number of hits registered in the SiPM is generated. The number of hits is calculated by the final number of photons at the fiber end with respect to the SiPM quantum efficiency. In the main simulation the quantum efficiency is assumed as a constant without wavelength dependency as there is no information about the wavelength there.

For the evaluation of the tracking algorithms and the digital readout of the detector a simulation of darkcounts in the SiPMs can be enabled. The darkcount photons are added to the signals calculated before. The crosstalk and the implementation of the darkcounts is done by [37].

4.4 Timing Limits

For the single fiber analysis the arrival time of the photons at the fiber end is used to estimate the time resolution that is achievable. In a first study the arrival time of the first photon is investigated. From each fiber the time when the first photon reaches the fiber end is taken and compared with the time from the first photon at the other fiber end. The width of the distribution of the arrival time differences specifies the resolution of the system. Figure 4.14 shows the distribution of the arrival times. It is clearly visible that it can be fit by a Laplace distribution (eq. (4.5)) as we probe essentially the decay time of the scintillation light with this approach:

$$f(t) = c \cdot e^{\frac{-|t|}{\tau}} \tag{4.5}$$

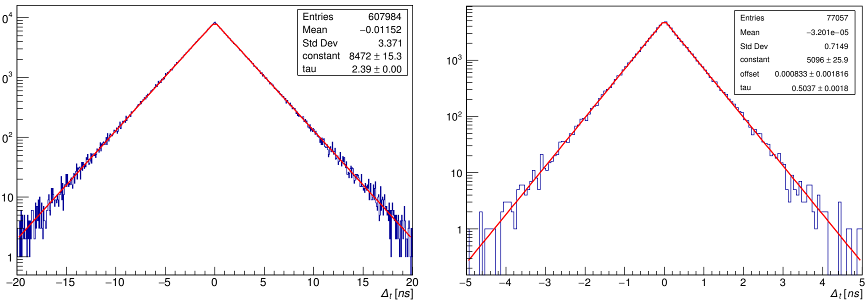

Figure 4.14: Time distribution of the arrival time difference of the first photon at each fiber end for a scintillator with a decay time of 2.4 ns *left* and 0.5 ns *right*.

The fact that the timing is dominated by the scintillation time needs further investigation. In fig. 4.15 the time difference distribution is shown where different minimal numbers of photons are demanded. As expected the distribution gets smaller with a higher number of photons. The Laplace distribution describes the data well with $\tau \propto 1/\#\text{photons}$. Defining here the time resolution as the full width half maximum (FWHM) and as $\text{FWHM} = 2\tau \ln(2)$ the time resolution is reciprocally proportional to the number of detected photons. Table 4.2 shows a summary of the expected time resolutions. To compare the simulation results and the measurements in section 6.6 with the design criteria that assumes a Gaussian distribution we compare the results with a Gaussian with the same FWHM as defined by $\text{FWHM}_{\text{Gaussian}} = 2\sqrt{2\ln(2)} \cdot \sigma \approx 2.35 \cdot \sigma$. As we measure the time difference between the arrival times of the photon on both fiber ends, the time resolution of one single fiber end (σ_{se}) is then $\sigma_{\Delta_t}/\sqrt{2}$ as both ends contribute the same way to the width. The best achievable time resolution would be using the mean of the two arrival times, leading to a resolution σ_{be} calculated as $\sigma_{\Delta_t}/2$.

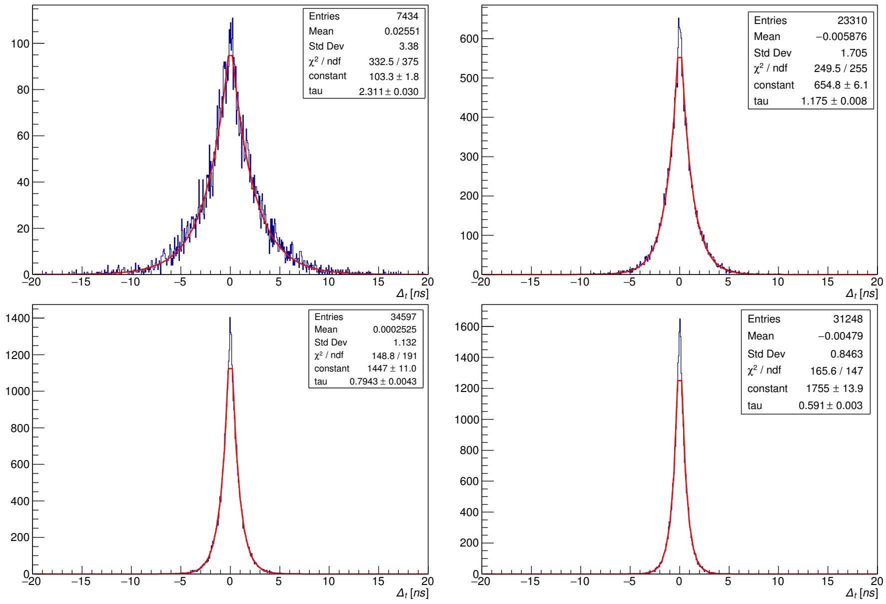

Figure 4.15: Time difference of the fist photon between the left and the right fiber end requiring exactly 1 (top left), 2 (top right), 3 (bottom left) or 4 (bottom right) photons.

Table 4.2: Resolution estimates by the time signal of the first photon requiring exactly 1,2,3 or 4 photons. "σ_{Δ_t}" is the value of the equivalent Gaussian with the same width, "σ_{se}" shows the time resolution looking at one single fiber end ($\sigma_{\Delta_t}/\sqrt{2}$), "$\sigma_{\mathrm{be}}$" the time resolution by averaging over both fiber ends ($\sigma_{\Delta_t}/2$).

photons	τ [ns]	FWHM [ns]	σ_{Δ_t} [ns]	σ_{se} [ns]	σ_{be} [ns]
1	2.3	3.2	1.4	1.0	0.7
2	1.2	1.7	0.7	0.5	0.4
3	0.8	1.1	0.5	0.3	0.2
4	0.6	0.8	0.3	0.2	0.2

The time resolution does not only depend on the fiber itself but also on the data acquisition system. The time distributions shown in fig. 4.15 give a theoretical limit on the time resolution. Depending on the DAQ system that will be used in the end the timing signal will not always be determined by the first photon alone. This effect is studied in fig. 4.16 and summarized in table 4.3. In this case the average arrival time per event for each fiber end is calculated and the time difference shown in the histogram. This scenario shows a worsening of the time resolution as the decay photons of the later times will now broaden the distribution. The best timing resolution is achieved by detecting as many photons as possible and by using a DAQ system that is sensitive to the arrival time of the first photon.

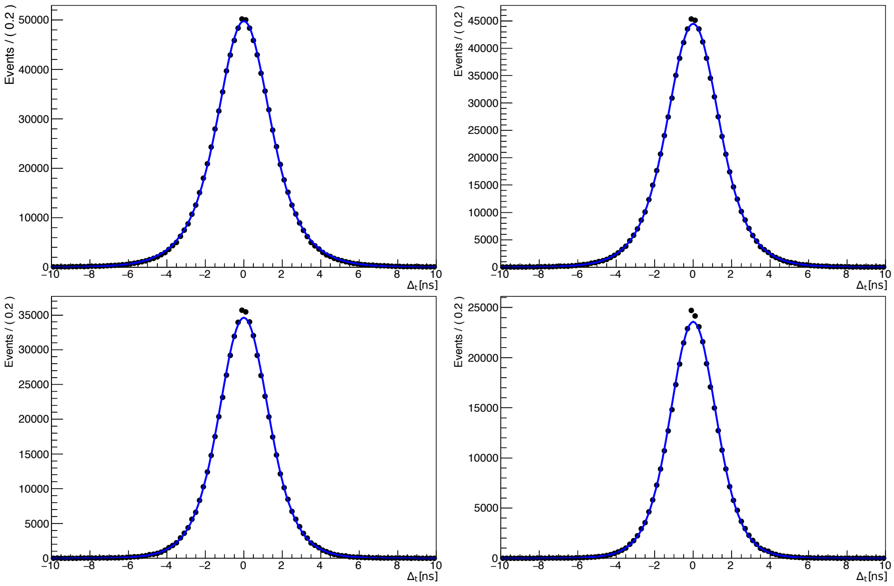

Figure 4.16: Time difference between the left and the right fiber end for measured at least 1 to 4 photons (from top left to bottom right) and the time average used on each side.

Table 4.3: Resolution estimates by the time average for at least 1 to 4 photons measured.

photons	FWHM [ns]	σ_{Δ_t} [ns]	σ_{se} [ns]	σ_{be} [ns]
1	3.3	1.4	1.0	0.7
2	3.2	1.4	1.0	0.7
3	3.0	1.3	0.9	0.6
4	2.8	1.2	0.8	0.6

The dependency of the time resolution on the number of photons makes it necessary to take the quantum efficiency of the sensor into account. As discussed in section 5.1.1 a typical quantum efficiency is about 35 %. In fig. 4.17 the distribution are shown including quantum efficiencies as stated by the technical datasheet for the sensors that are used for the test measurements discussed in the next chapter. From the simulation the wavelength of the photon arriving at the fiber end is known (cf. section 4.2) and for each photon it has been calculated whether or not it is seen by the SiPM by using a Bernoulli trial with the quantum efficiency as a probability. The results are summarized in table 4.4.

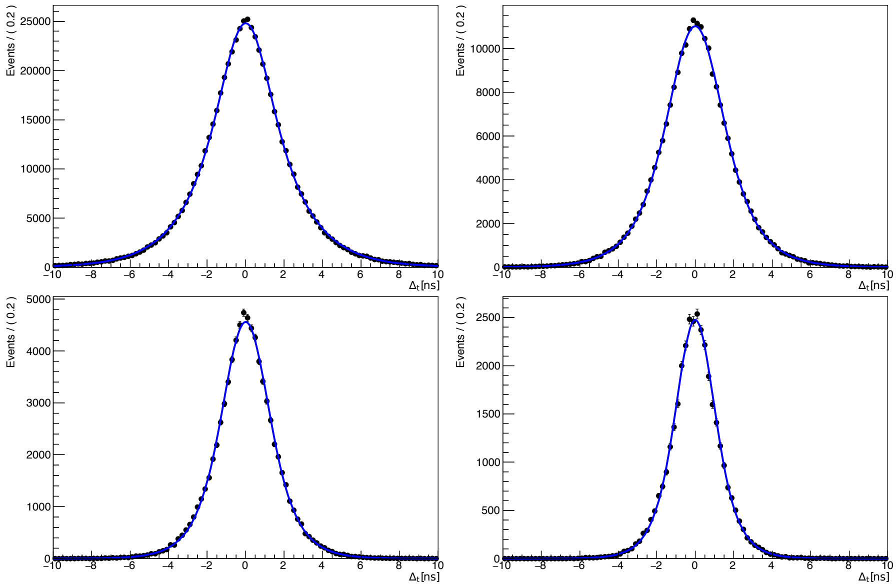

Figure 4.17: Time difference between the left and the right fiber end for at least 1 to 4 photons measured (top left to bottom right) and the time average used on each side. The quantum efficiency of the SiPM is taken into account.

Table 4.4: Resolution estimates using the time average for at least 1 to 4 photons measured. The quantum efficiency of the SiPM is taken into account.

photons	FWHM [ns]	σ_{Δ_t} [ns]	σ_{se} [ns]	σ_{be} [ns]
1	3.9	1.7	1.2	0.8
2	3.6	1.5	1.1	0.8
3	3.0	1.3	0.9	0.6
4	2.5	1.1	0.8	0.5

The results in fig. 4.16 and fig. 4.17 show that the time resolution gets worse compared to the theoretical limit in fig. 4.15 when more realistic detection scenarios are implemented. The time resolution is not only determined by the scintillator but also by the definition of the timestamp. Depending on the coupling of the fiber to the SiPM and the detection efficiency of the SiPM the time resolution also changes. Less light due to a bad coupling leads to a worsening of the time resolution of the system. In the case of events with more than one photon another effect starts to be important: Depending on the algorithm used to specify the time, the photons coming later due to the exponential decay will not be taken into account anymore.

The simulations show that using the combined readout of both fiber ends a time resolution below 1 ns can be achieved.

Measurements were performed and discussed in section 6.6 to compare this theoretical limits with experimental reality in order to get confidence into the accuracy of the simulation.

4.5 FIBER RIBBON ANALYSIS

With the modular principle of the software different fiber ribbon configurations have been tested. For this particular analysis the main crossing angle of the electrons regarding to the ribbon has been evaluated. The light yield has been evaluated for crossing a fiber ribbon at different positions. With the help of the detector simulation the mean angle of the particle crossing has been evaluated. In this analysis a homogeneous magnetic field of 1 T is assumed. Figure 4.19 shows the distribution of the angle where the electrons cross the fiber ribbon. The angle is defined relative to the fiber ribbon, i.e. relative to the radial vector as shown in fig. 4.18.

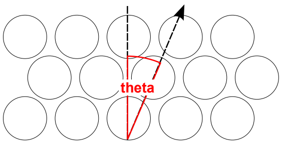

Figure 4.18: Definition of the crossing angle of the electrons relative to the fiber ribbon orientation.

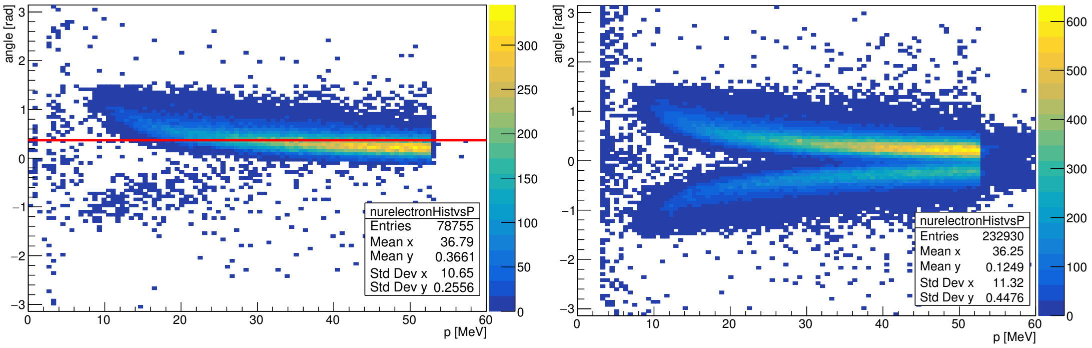

Figure 4.19: Distribution of the electron fiber crossing in the detector (cf. fig. 4.18). The data shows electrons and positrons crossings only. In the left picture the crossing for all muon decay events are shown. The distribution is therefore dominated by the electrons produced by Michel decays. The mean angle is highlighted in red. As a comparison the right picture shows the distribution for μ→eee events only.

With the mean angle as seen from the distribution two possible fiber staggerings have been considered. Figure 4.20 left shows the natural way to stagger the fibers where there is an offset of half a fiber width per layer. Figure 4.20 right shows a way to stagger them without an offset called the squared staggering.

The light yield has been simulated by for ribbons of both configurations. For each configuration 10 000 events have been recorded where the electron passes the ribbon under the mean angle. Each fiber has been analyzed individually looking at the photon yield at the fiber end. The photon yield is estimated by fitting the distribution to a

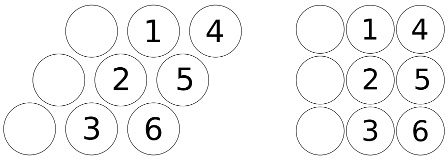

Figure 4.20: Simulated scenarios to stagger the fibers.

convolution of a Landau distribution with a Gaussian distribution (fig. 4.21, right). The Landau distribution is justified by the fact that the energy deposition follows the Landau distribution and the number of generated photons is proportional to the energy deposit. The Gaussian smearing originates from the photon production mechanism as discussed in section 4.2.

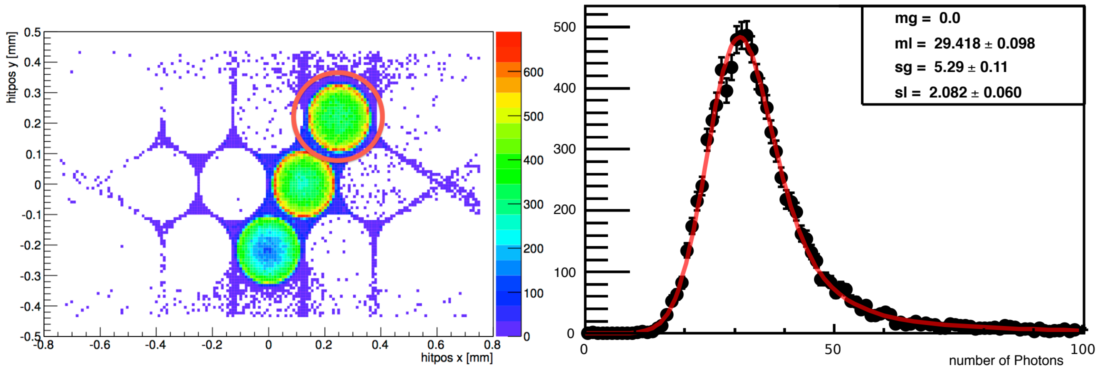

Figure 4.21: Example of the light yield simulation for a fiber crossing at $x = 40\,\mu\text{m}$ from the center. The overall light yield is shown in the left figure and the parametrized for the emphasized fiber is shown right.

Figure 4.22 shows the light yield of the ribbons depending on the crossing position of the electron. The values show the most probable value that is expected per event. It is clearly visible that the denser staggering leads to an increased light yield under certain conditions but the sum of the light depends strongly on the crossing position. The squared staggering leads to a more uniform distribution but never reaches the maximum light yield of the dense staggered ribbon. The dead material (in this case the glue used to build the ribbon) and therefore the overall material budget of the squared staggered ribbon is increased compared to the other staggering. The decision which geometry should be used is finally a trade of between light yield, uniformity and mechanical feasibility. A much more complicated way to build it and the increased passive material disfavors the squared staggering.

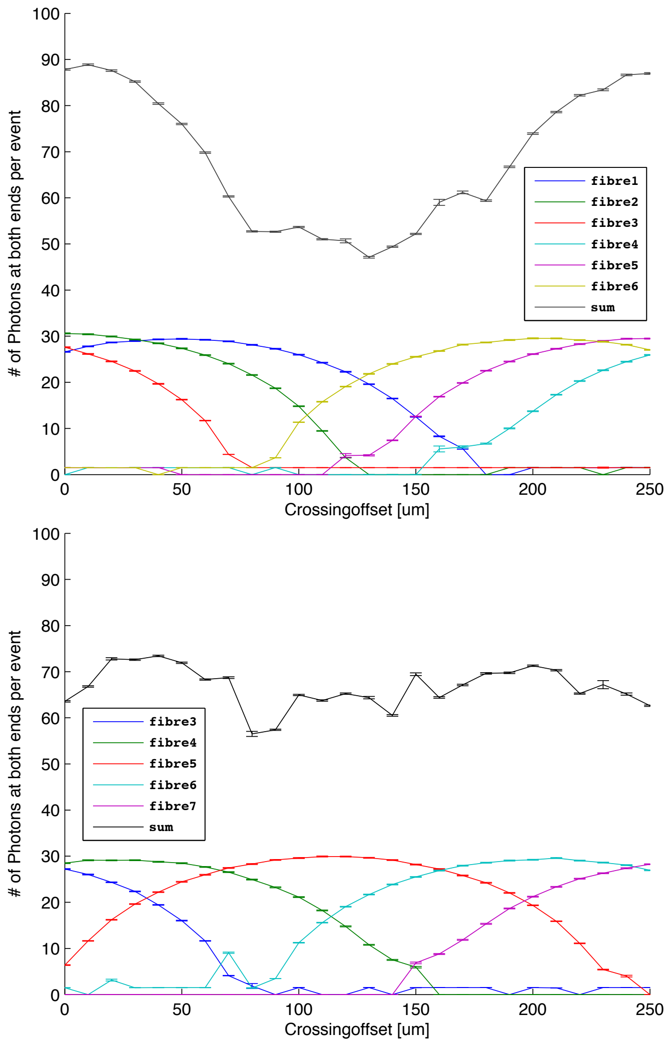

Figure 4.22: Predicted number of photons versus positron crossing position at the most likely crossing angle for two alternative staggering geometries. The top figure shows the light yield for fibers staggered as shown in fig. 4.20 left and the bottom figure for fibers staggered as in fig. 4.20 right.

4.6 Simulation Scenario for the Test Beam

A special set of simulations has been performed that is used to compare the simulation with testbeam measurements. In this simulations the length of the fiber has been changed to 49.5 cm to fit the ribbon length that has been produced (cf. section 5.1). The PSI simulation scenario implements the exact sensor used for all test measurements as described in section 5.1.1. It includes the active area of the sensor, the refraction index of the epoxy resign and the air gap due to the plastic housing of the SiPM having a border higher than the position of the sensor itself.

The simulation uses a particle source that emits electrons with the same momentum used at PSI, set to 161 MeV/*c*. In addition, the source is implemented to have a homogeneous distribution along the fiber height (cf. fig. 4.23). The results from the PSI simulation are discussed in chapter 6 where they are directly compared to measurements.

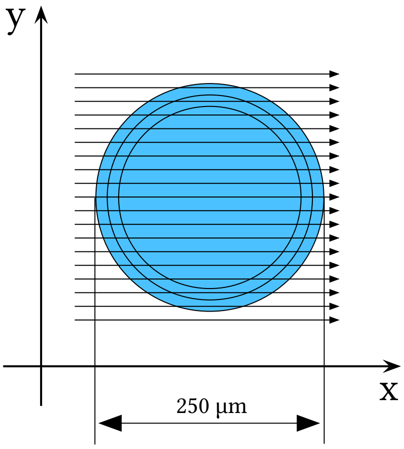

Figure 4.23: Particle crossing along the fiber diameter for the PSI simulation. The crossing is equally distributed along the *y* axis.

5

Fiber Prototype

In this chapter a test setup is discussed that has been developed to verify the fiber simulation studies. All hardware parts are built in a modular way and can therefore be exchanged independently. The modules consist of the fiber ribbons, a fanout for the specific fibers under investigation, sensor boards, signal amplifiers and the signal digitization.

5.1 TESTFIBERS AND RIBBONS

In all tests the Kuraray SCSF-81M fiber as described in chapter 4 have been used. In collaboration with the University of Geneva and the ETH Zürich several test ribbons have been produced. The fibers in the test ribbon have a total length of 49.5 cm including the fiber fanout. A special tool that has been developed in Geneva is used to align the fibers properly where they are glued in several steps layer by layer. A polytetrafluoroethylene holding structure allows to glue the fibers together in a holding structure and avoids that the fibers are stuck to the holding structure after the hardening of the glue.

The fibers have been glued to 16 mm wide modules like they are planned to be installed for the experiment. The ribbons consists of four layers where the fibers on each layer are shifted of half the fiber pitch. They are glued together with an epoxy resin (fig. 5.1). In two adjacent layers there are for each layer eight fibers guided to a fanout board that fits the pitch of the photon sensors as described in section 5.1.2. To hold the fibers in the fanout they are glued from the backside with an epoxy resin. The holes in the fanout have a diameter of 300 µm so that the fiber cladding is not

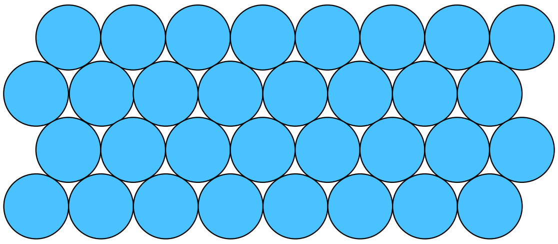

Figure 5.1: Schematic of the fiber ribbon cross-section. Only a fraction of the ribbon is shown.

damaged during insertion of the fibers and that the resin can flow into the holes for a stronger fixation. A smooth surface is achieved by first cutting the fibers close to the fanout and by additional polishing. The polishing is done by hand with a polishing set used for optical communication fibers (fig. 5.2). Only ribbons without TiO coating were available that could be tested.

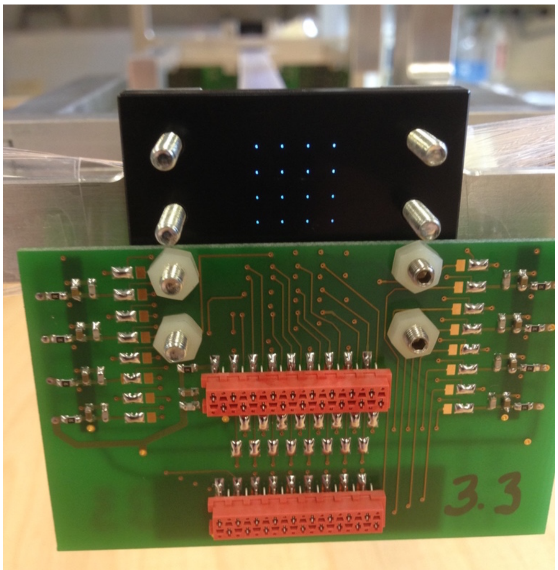

Figure 5.2: The fibers are glued in a fanout that matches the sensor board. The lower half of the fibers is already connected to the sensor board.

A mounting structure (fig. 5.3) is used to hold the ribbon, its fanout, the sensor boards and the amplifiers. The mounting structure is built such that the ribbon is mechanically protected and can be rotated along the longitudinal axis to the desired angle for test beam studies.

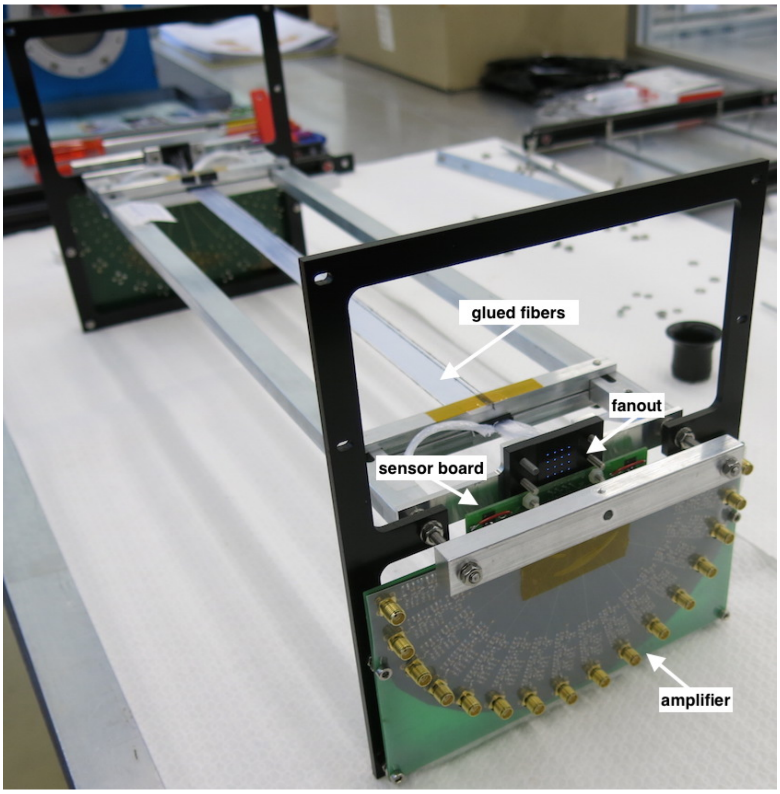

Figure 5.3: 16 mm wide ribbon with 250 µm thick double cladding fibers in the mounting structure.

5.1.1 Photon Sensors

Different photon sensors have been tested. An early prototype used was a monolithic device with 4×4 SiPMs with a 1.3 mm pitch. Because these devices showed in the tests an extremely high darkcount rate (up to 1 MHz) and the fact that they have a common anode which leads to an increased electrical crosstalk they have not been used any further. To keep the system backward compatible also the successor sensor board uses the same pitch even though they could have been built with a narrower pitch. In the final design Hamamatsu S12571-050P silicon photomultipliers [68] are used. These sensors have an active area of $1 \times 1\,\mathrm{mm}^2$ with a pixel pitch of 50 µm and in total 400 pixels. Each sensor has a geometrical fill factor of 62 %. They are built as a surface mountable device with an epoxy resin window with a refractive index of $n_{\mathrm{Window}} = 1.55$. The spectral response wavelength ranges from 320 nm to 900 nm (fig. 5.4), with a gain of $1.25 \cdot 10^6$ at the recommended voltage. The darkcount rate of this sensors is about 100 kHz when biased with the recommended voltage at 25 °C ambient temperature.

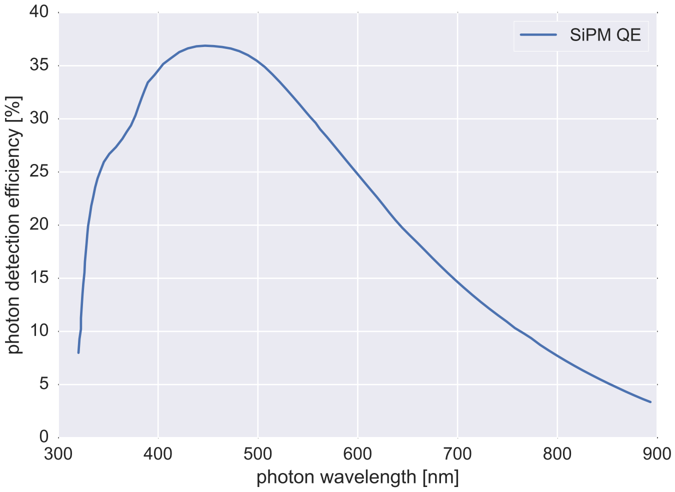

Figure 5.4: Quantum efficiency of the S12571-050P SiPMs at a bias voltage $U_{\text{op}} = U_{\text{BR}}{+}2.6\,\text{V}$. Adapted from [68].

5.1.2 SENSOR ELECTRONIC

The sensor board design allows two ways to bias the individual SiPMs. Either a common voltage is used that powers all the SiPMs with the same voltage or individual voltages for all sensors can be applied. For the measurements done for this thesis the common high voltage is used. The voltage distribution uses a RC low pass filter before each SiPM to decouple them electronically. Figure 5.5 shows a simplified schematic of the readout electronics focusing on the sensorboard. If used with the amplifier the readout is single ended over the shunt resistor $R_{\text{shunt}} = 39\,\Omega$. The readout with the STiC chip is done differently. In this case all the electronics is integrated into the chip and the sensor board only needs to connect the SiPM to the STiC without additional electronics.

The sensor board provides four mounting holes so it can be screwed easily to the fan-out of the fibers with a proper alignment. The first generation of the board can only be used with the amplifier described in section 5.2 with a 16 pin TE connectivity micromatch plug.

The second generation board has been extended to the possibility to use it without the amplifier to connect it directly to the STiC ASIC chip. In this case all the electronics and high voltage supplies are provided by the ASIC. For backward compatibility it can still be used with the setup mentioned above and solder pads are used to switch between the two modes.

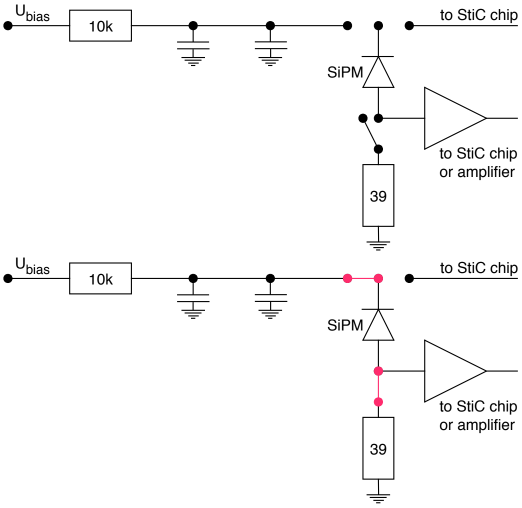

Figure 5.5: *Top:* Electronic scheme of the sensor board. The wiring is repeated for each SiPM. The top switch is used to select a common bias voltage for single ended readout or an individual biasing for differential readout. In the differential readout case the signal goes to the amplifier before the 39 Ohm shunt resistor and needs to be opened therefore. *Bottom:* Setting of the switches (red) used for this thesis.

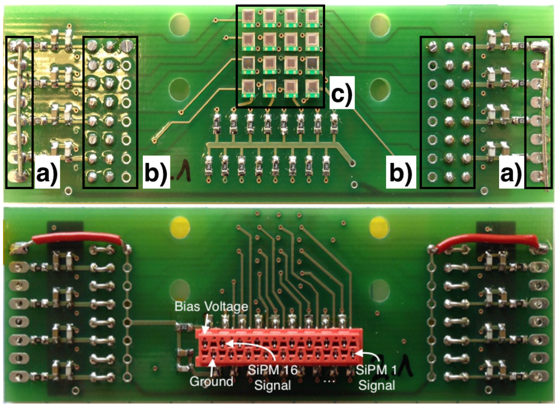

Figure 5.6: Picture of the 2nd generation sensor board. The top pictures shows the side with the sensors, the bottom picture the backside with the connector to the amplifier board. *a)*: connection for individual bias voltage, *b)*: optional space for jumpers for individual or common high voltage, *c)*: SiPM sensor matrix

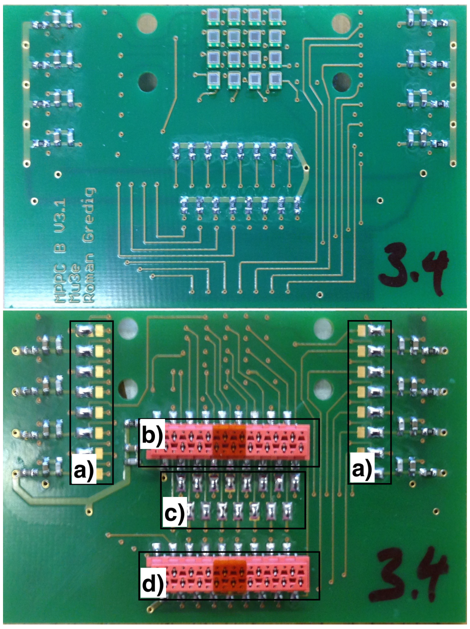

Figure 5.7: 3rd generation sensor board. The solder pads *a)* are used to change between common high voltage or for the individual one from the STiC chip. The micromatch plug *b)* uses the same pinout as the 2nd generation sensor board. To use it with the STiC chip the resistors to ground can be switched of with the solderpads *c)* and the circuit connected to the STiC with *d)*.

5.2 Readout Electronics

The signals generated by the SiPMs need to be amplified so that they can be connected to the data acquisition system with a signal amplitude high enough that it can be recorded using the full scale of the analog to digital converter range.

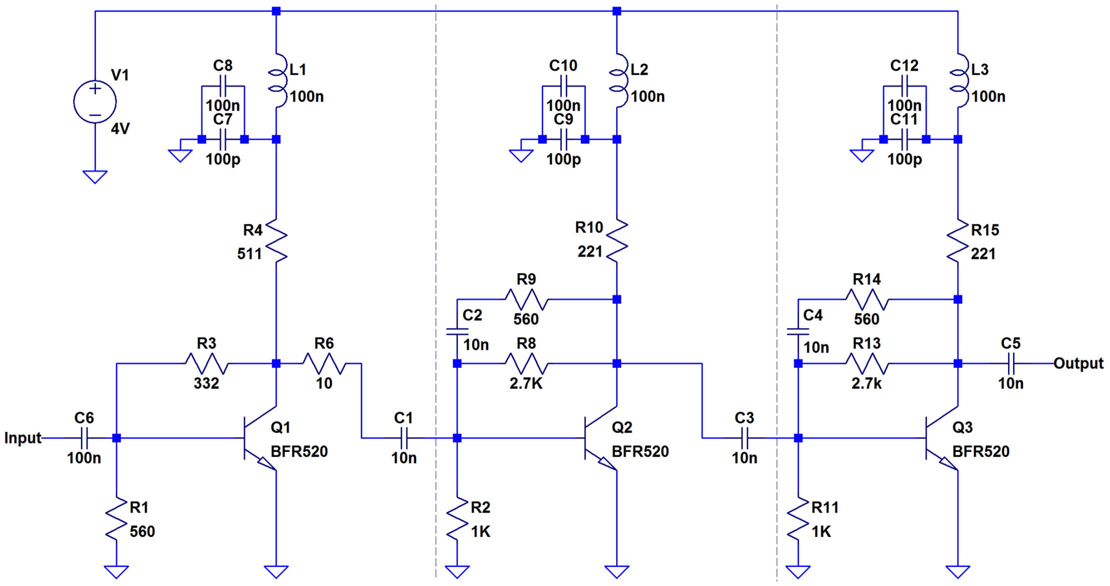

Figure 5.8: Schematic of the amplifier as used for every SiPM channel. Each transistor power has its own filter.

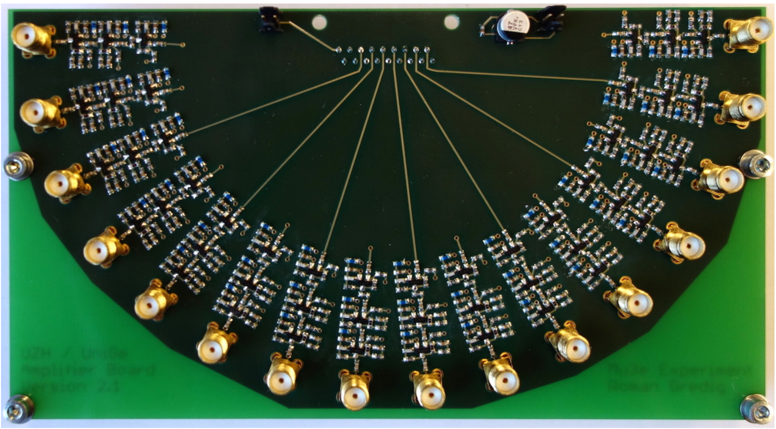

Figure 5.9: Sixteen channels amplifier board. The connector for the sensor-boards is on the back side. The amplified signal is fed via the SMA sockets to the DAQ system.

Based on a design developed at the University of Geneva by Yannick Favre a three stage common emitter circuit amplifier is implemented. The photon current generated by the SiPM is converted to a voltage by the shunt resistor as shown in fig. 5.5 and fed into the amplifier via the AC-coupling capacitor C_6 shown in from fig. 5.8. The amplifier gain can be adjusted by changing the supply voltage within a range of about 3 V to 8 V. If not stated otherwise 4 V are used to power the amplifier. A wide band transistor, the BFR520 from NXP Semiconductors [69], with a transition frequency of 9 GHz has been used for all three stages. At the second and the third stage there is a frequency dependent voltage feedback to compensate for the high-pass behavior because of the AC coupling capacitance between the stages. The amplifier is built to drive a 50 Ω cable to route the signal into the DAQ system. The response is simulated with a SPICE simulation within a frequency range of 10 MHz to 6000 MHz as shown in fig. 5.10.

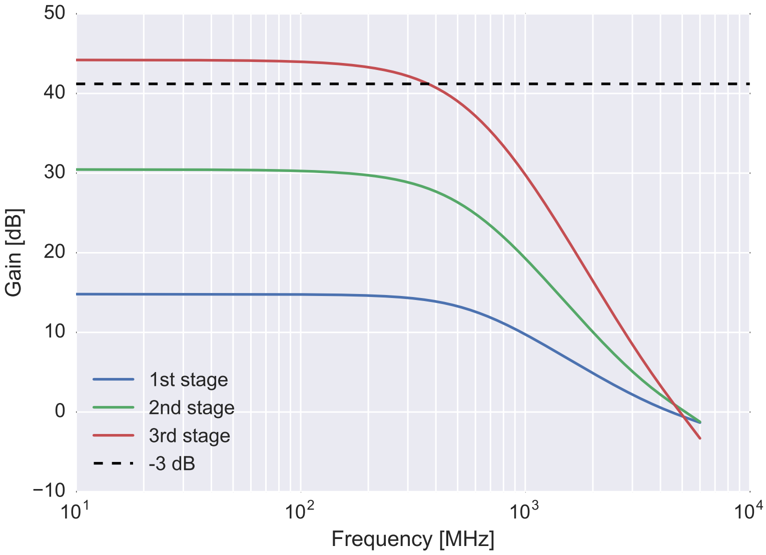

Figure 5.10: Spice simulation of the amplifier gain at 4 V supply voltage.

To simulate the expected signal with the amplifier a one photoelectron pulse has been simulated. In a simplified model each cell of the SiPM is a charged capacitance C_c (fig. 5.11). The cell is charged to the bias voltage U_{Bias}. At the moment of an avalanche induced by a photon the cell capacitance is discharged up to the breakdown voltage as the voltage over the SiPM drops because of the quench resistor R_q built into the SiPM. Quench resistors have a typically values of $\mathcal{O}(100\,\text{k}\Omega)$. The discharge is done through a resistor R_s that represents the resistance of the depleted region containing the avalanche plasma and the neutral part of the sensor[1]. The resistance is about 1 kΩ. The capacitance C_c is given by the gain and at a specific over-voltage. The sensors are operated at an average over-voltage of 2.6 V where they have a gain of $1.25 \cdot 10^6$. With $C = \frac{Q}{U}$ this leads to a capacitance

$$C_c = \frac{1.602 \cdot 10^{-19}\,\mathrm{C} \times 1.25 \cdot 10^6}{2.6\,\mathrm{V}} = 7.7 \cdot 10^{-14}\,\mathrm{F}. \tag{5.1}$$

The moment the voltage over the capacitance drops a current through the quench resistor starts. This current reaches its maximum I_max when the capacitor is discharged down to the breakdown voltage U_BR. With a quench resistor of $R_q = 300\,\mathrm{k\Omega}$ the current reaches up to

$$I_\mathrm{max} \approx \frac{U_\mathrm{Bias} - U_\mathrm{BR}}{R_q} = 8.7\,\mu\mathrm{A}. \tag{5.2}$$

The discharge time constant is

$$\tau_\mathrm{discharge} = R_s C_c = 7.7 \cdot 10^{-11}\,\mathrm{s}. \tag{5.3}$$

The current in the sensor is converted to a voltage by a (small) shunt resistor with a value of $R_\mathrm{shunt} = 39\,\Omega$ leading to a peak input voltage of the amplifier of $U_\mathrm{max} \approx 340\,\mu\mathrm{V}$. After dropping below the break down voltage the discharging stops and the diode's capacitor charges up again to the bias voltage. The charging current flows via the quench resistor R_q resulting in a time constant

$$\tau_\mathrm{recharge} = R_q C_c = 2.3 \cdot 10^{-8}\,\mathrm{s}. \tag{5.4}$$

For the spice simulation the signal input is modeled therefore as

$$U_\mathrm{input}(t) = U_\mathrm{max}\left(-\exp\left(\frac{-t}{\tau_\mathrm{discharge}}\right) + \exp\left(\frac{-t}{\tau_\mathrm{recharge}}\right)\right) \tag{5.5}$$

In fig. 5.12 the simulation results for a sample SiPM signal and a true digitized signal are compared. The signals are in the expected range where individual variations of the amplitudes are expected since the over-voltage is not always 2.6 V for all sensors because all 16 sensors are at a common high voltage.

---

[1] not to be confused with the shunt resistor

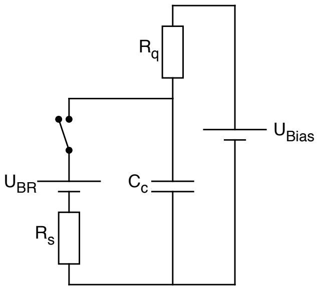

Figure 5.11: Electric circuit model of one SiPM microcell. The start of an avalanche is simulated by closing the switch. Adapted from [70].

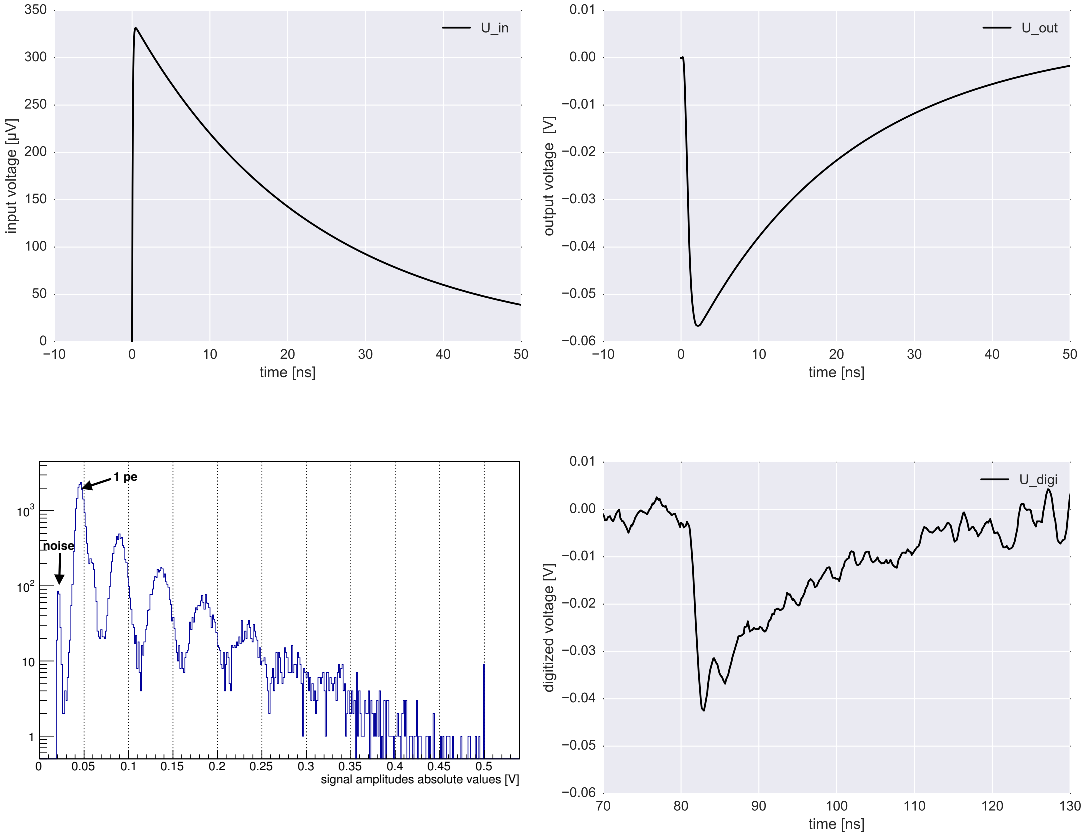

Figure 5.12: Spice simulation of the SiPM signal *(top left)* and the amplifier output *(top right)* compared with the measured signal amplitudes distribution *(bottom left)* and a sample digitized signal waveform *(bottom right)*

5.3 Data Digitization

5.3.1 Signal Recording

For a detailed understanding of the fiber ribbon response a DAQ system with waveform digitization has been envisaged. The idea was to record at least 2 × 16 channels leading to a readout of 16 fibers at both ends. All the data recording has been done with the DRS4 evaluation board developed at the PSI [71]. The evaluation board consists of a switched capacitor array that can sample to up to 5 gigasamples per second. If a trigger signal occurs the data is digitized from the buffer with a 14 bit analog to digital converter and written out to a binary file. Each evaluation board has four analog inputs terminated at 50 Ω. As 2 × 16 channels are needed to be recorded the evaluation boards have to be daisy chained. The final setup uses 8 boards for the SiPM signal inputs and one board in addition for an optional trigger. The trigger and clock signals are propagated trough all the evaluation boards.

Figure 5.13 shows the principle of the daisy chaining possibility of the evaluations boards. Only the master board at the beginning of the chain can be used as a trigger board. Triggering is either done by a threshold at the analog input or fed in externally via a TTL signal. The clock propagation is done via the FPGAs inside the evaluations boards.

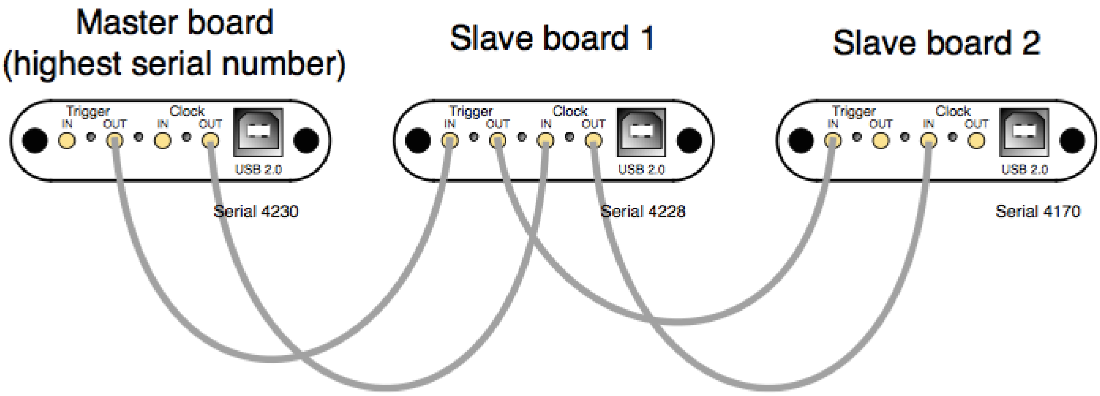

Figure 5.13: Schematic of the daisy chaining of the DRS evaluation board. The analog inputs are on the other side of the boards. Picure taken from [72].

5.3.2 Data Acquisition Time Resolution

A test series has been performed to test the accuracy of the timing between different boards. With a pulse generator an analog pulse with a steep falling edge (2.5 ns from 10 % to 90 % of the pulse height) has been generated. The pulse is then split passively by an owen-splitter[2] to ensure that there is no time jitter between the two test pulses. The pulses after the splitter are fed into two inputs. Either two inputs of the same board have been used or two inputs of different boards (fig. 5.14) and for each combination 100 000 events have been recorded. The resolution of the DAQ system consists of two parts:

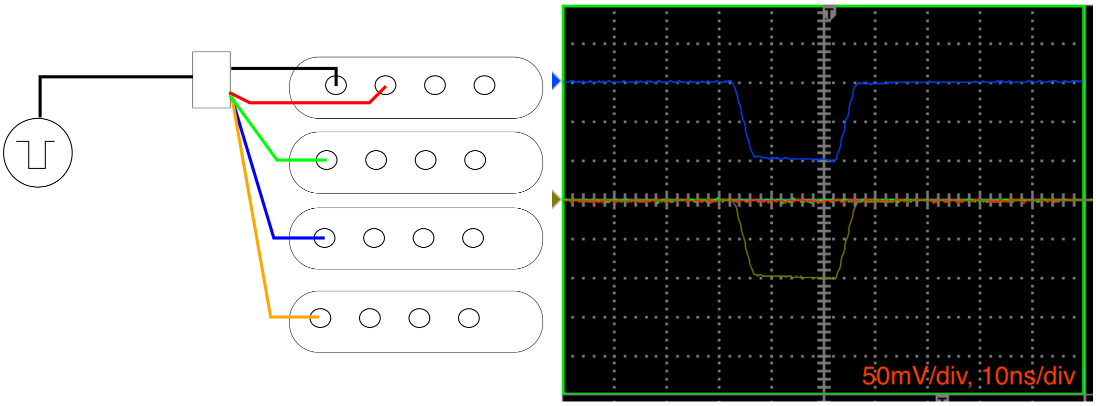

Figure 5.14: *Left*: Schematic of the setup to measure the time resolution of the DAQ system. The analogue signal is split into two channels where one channel is always connected to the first board and the second is connected to different boards for each measurement. *Right*: the signal injected by the function generator

- the time resolution within one board: σ_{ch}
- the jitter of the trigger propagation between boards: $\sigma_{\mathrm{interboard}}$

The time resolution within one board can be estimated by the distribution of the time difference between the two split signals. Assuming that all channels on one board have the same time resolution and that their measurement is independent, the width of the time difference distribution is

$$\sigma_{\Delta t} = \sqrt{{\sigma_{\mathrm{ch1}}}^2 + {\sigma_{\mathrm{ch2}}}^2} = \sqrt{2{\sigma_{\mathrm{ch}}}^2}\ . \tag{5.6}$$

A possible jitter between the analog signal from the generator and its sync TTL output (used to trigger the DRS) is irrelevant for this measurement as it is a relative measure only. Assuming a Gaussian distribution of the time difference histogram the $\sigma_{\Delta t}$ can

---

[2] Named after Chris Owen. It is a resistive splitter only and therefore performs from DC up to high frequencies as there is no intrinsic limit (only parasitic elements) of the bandwidth. An additional good isolation between the ports helps to reduce signal crosstalk that might be happen because of impedance mismatch.

be estimated (see top left figure of fig. 5.15) and the channel resolution becomes

$$\sigma_{\text{ch}} = \frac{\sigma_{\Delta t}}{\sqrt{2}} = 95\,\text{ps} \tag{5.7}$$

The jitter of the boards can be calculated from the width of the time difference between different boards

$$\sigma_{\Delta t} = \sqrt{2{\sigma_{\text{ch}}}^2 + n \cdot {\sigma_{\text{interboard}}}^2} \tag{5.8}$$

where n is the number of boards in between the two channels $+1$ and therefore

$$\sigma_{\text{interboard}} = \sqrt{\frac{{\sigma_{\Delta t}}^2 - 2 \cdot {\sigma_{\text{channel}}}^2}{n}} = 132\,\text{ps}\ . \tag{5.9}$$

Equations (5.7) and (5.9) show that the time resolution is dominated by the uncertainty between two boards. The reason is that the clock and the trigger signal are propagated through the chain via the FPGAs inside the evaluation boards. The time resolution could be increased using an external clock and feeding it in into one channel of each board. This would reduce the number of available channels by 1/4 and requires an accurate clock distribution. This approach has not been taken into account.

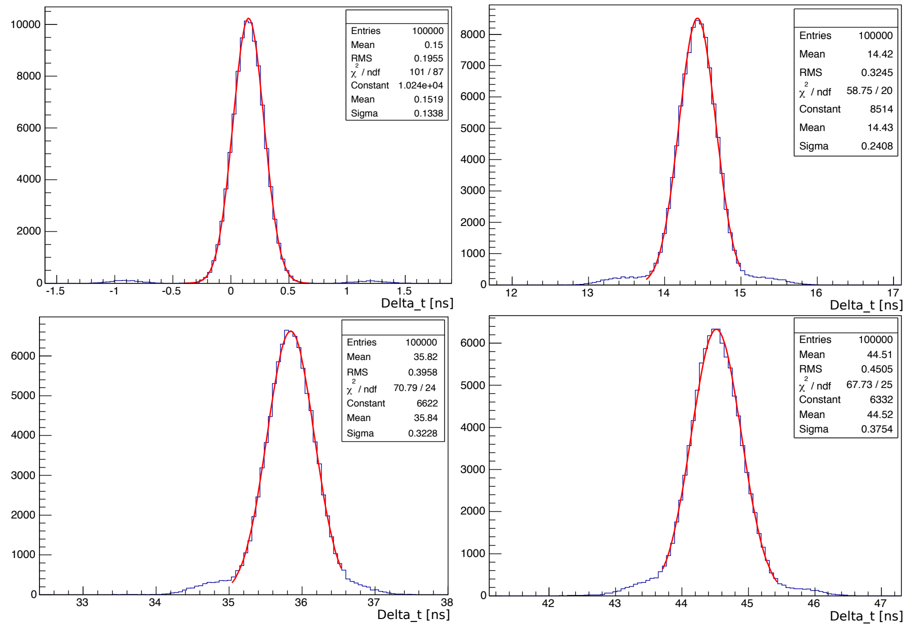

Figure 5.15: Distribution of the time signal difference for two channels on one board, board 1 and board 2, board 1 and board 3, board 1 and board 4 (from top left to bottom right).

5.4 Post Signal Processing

The recorded data is processed before any analysis is done. This procedure helps to reduce the amount of data which leads to an heavy increase of the speed in the data analysis. The data digitized as described in section 5.3.1 is written in a 200 ns long time window with a common time base for all channels. After a trigger occurs the SiPM can generate signals several times within the whole buffer length. The reasons for several signals are: an actual photon coming from the fiber, dark counts or another photon as the particle rate in the laboratory or during test beams might be as high that one trigger event records several particle crossings.

5.4.1 Signal Splitting

In a first step the whole buffer is divided in *sub-signals*. The post processing algorithm searches along the buffer for a crossing of the signal below a given threshold[3]. From this threshold it searches back until the signal passes over 0 V. This defines the beginning of a sub-signal. The end of a sub-signal is set to the point when the signal passes again over 0 V after the threshold. The following steps are done for all sub-signals found.

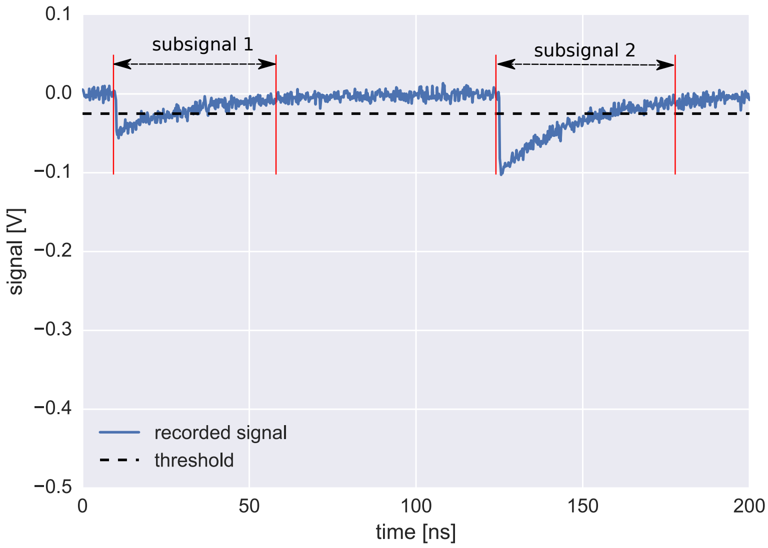

Figure 5.16: Example of a recorded signal. The red lines indicate where a sub-signal starts and where it ends. Information like amplitude, integral, timestamps is written out for each sub-signal.

---

[3] In general the threshold is set to 0.5 p.e., i.e. -0.025 V. Depending on high voltage, low voltage and noise conditions this value has been changed.

5.4.2 Signal Intensity

The signal amplitude within a sub-signal and the integral are written out to have information about how many photoelectrons have been measured. Due to pickup noise and crosstalk[4] in the electronics the integral information is used to determine the number of photoelectrons as the integral is less sensitive to this kind of noise (fig. 5.17).

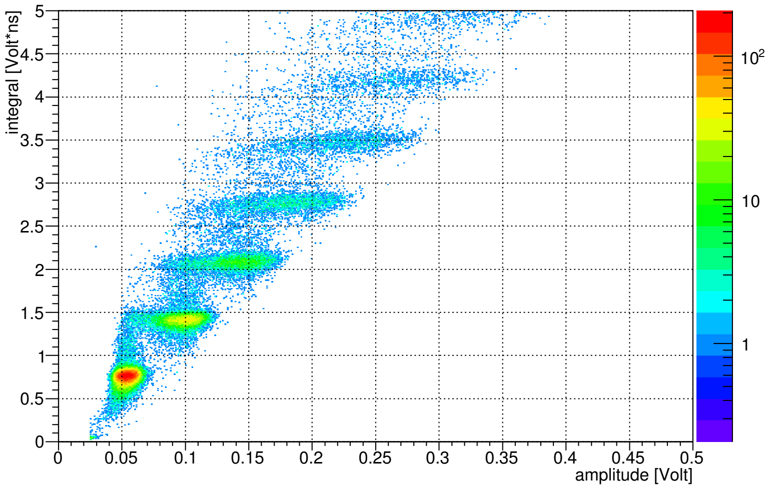

Figure 5.17: Comparison between the integral and amplitudes information for one fiber. The smearing of the amplitude is more dominant whereas the integral information delivers a good separation between the numbers of photoelectrons.

5.4.3 Time Information

For each sub-signal a time is determined. The optimal algorithm to specify the time is dependent on the scenario and the signal. Different algorithms are implemented and used for all sub-signals. These algorithms are explained in the following sections.

Threshold

The simplest way to get a time information is to use the time at which the signal crosses a given threshold. The same threshold is used as the threshold to define sub-signals. The use of the threshold for timing is highly depreciated as it leads to a *time walk* where the time information is dependent on the signal intensity. The threshold algorithm is implemented to cross check other timing algorithms and is also used for signals that do not change in amplitude or shape.

---

[4] In this case the electrical crosstalk in the sensor board wires before the amplifier is meant and not crosstalk within the SiPM that produces additional photoelectrons

Constant Fraction

The constant fraction algorithm is used to compensate for the time walk. Instead of a constant threshold the time is specified when the signal reaches a constant fraction relative to its maximum. For this work the threshold was set to 20 %. Even though the constant fraction discrimination helps to prevent a worsening of the accuracy of the time measurement it can still shift the time signal in case of an after pulse of the SiPM. As signals with only one photoelectron have to be taken into account an after pulse can shift the time as soon as the amplitude is higher than the one from the actual signal.

FlashCam Algorithm

The best accuracy has been achieved by adapting an algorithm developed for the FlashCam project for the Cherenkov Telescope Array (CTA) [73]. The sub-signal is first numerically differentiated. From the derivative the center of gravity between the zero crossing in the beginning and the next following (i.e. at the signal amplitude) is calculated and used for the time stamp (fig. 5.18). Figure 5.19 shows the difference between the timing using a threshold and the FlashCam algorithm. If not mentioned different, for all timing analysis the FlashCam algorithm has been used.

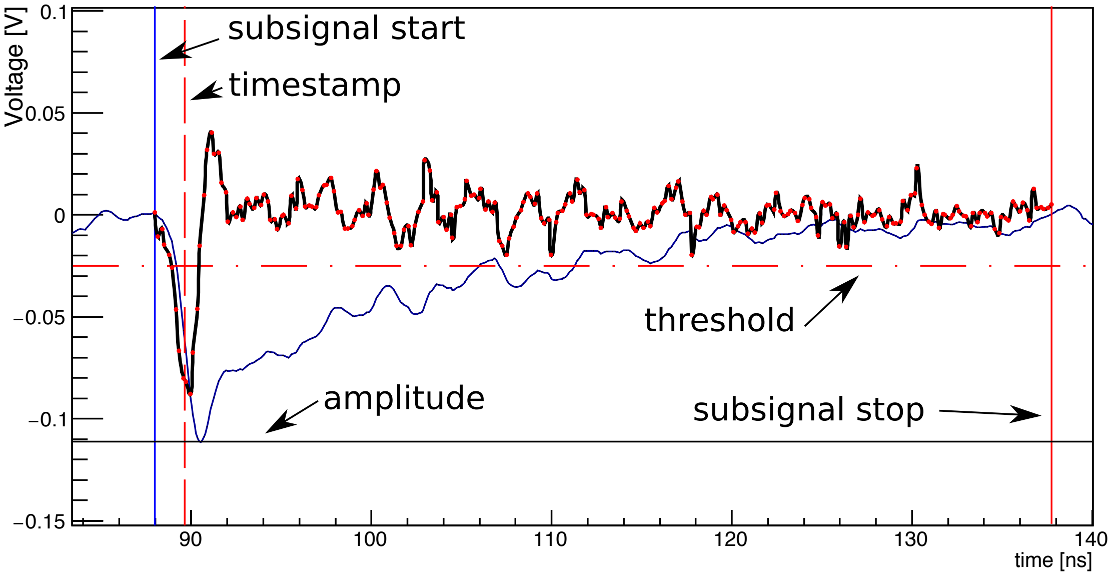

Figure 5.18: Sample of a digitized waveform. The raw data is shown in blue, the processed data in black. The red dotted line shows the definition of the time-stamp.

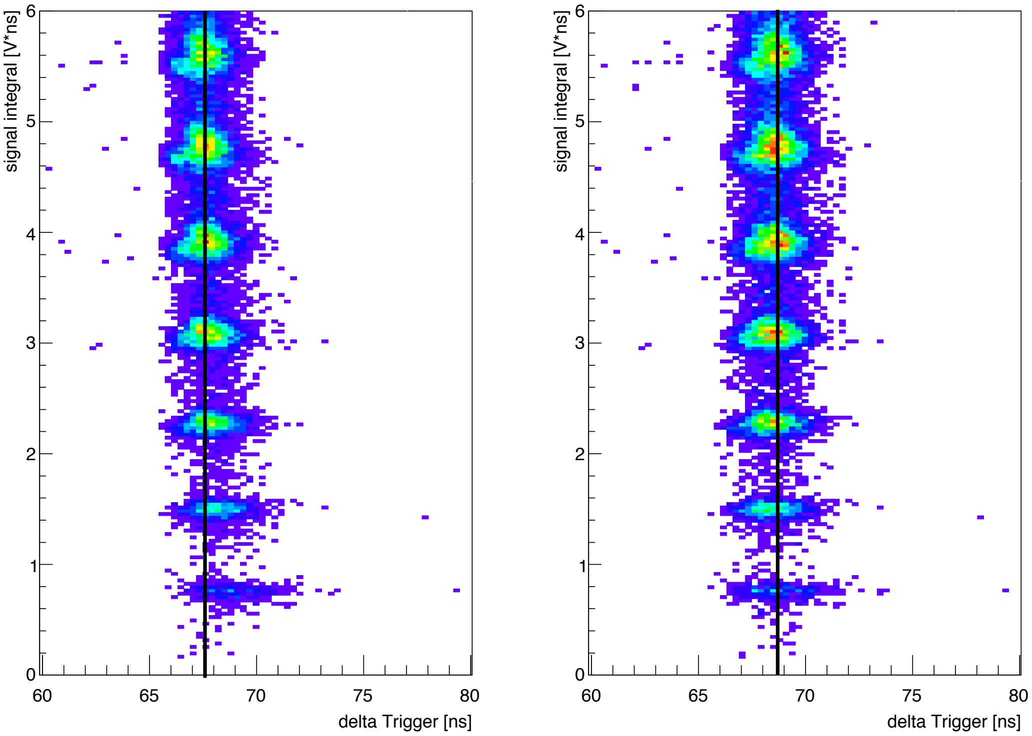

Figure 5.19: Comparison between the threshold timing algorithm *(left)* and the FlashCam timing algorithm *(right)* for one fiber. The time is relative to the time stamp generated by the scintillator trigger described in the next section. The data has been recorded with a 161 MeV c^{-1} electron beam at PSI with an offline particle identification shown in chapter 6.

5.5 TRIGGERING

For the investigation of the fibers during test beams and in the laboratory an external trigger has been used. This trigger consists of two 1 mm diameter fibers arranged under an angle of 90° connected to a photomultiplier tube (PMT) each (fig. 5.20). Each fiber is surrounded by a tube that keeps the fiber in place. Furthermore the tubes are light tight so that only photons generated by the fibers reach the PMT. The very compact trigger has been built using the Hamamatsu R7400U subminiature PMTs with a diameter of 16 mm and a length of only 12 mm. The PMT signals are directly connected to the trigger board of the DAQ system. The trigger starts the recording of one event with the DAQ when both PMT signals reach a threshold below −20 mV in coincidence.

For all the measurements the trigger has been placed behind the fibers, which is

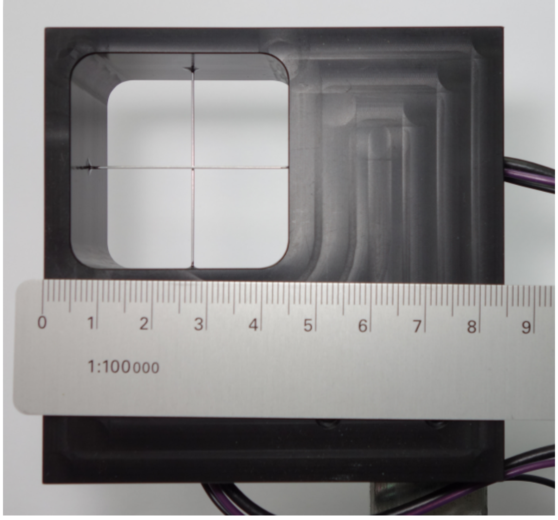

Figure 5.20: Trigger cross with two 1 mm round fibers using two photomiltiplier tubes.

in particular important for measurements done in the laboratory where a ^{90}Sr source is used to avoid measurements where the strontium electrons are stopped within the fibers due to their low energies.

5.6 Silicon Photonmultiplier and Amplifier Time Resolution

For all measurements with the fiber ribbons the major goal is to measure the time resolution that is achievable. The time resolution of the DAQ-system itself was discussed in section 5.3.2. To understand the time resolution of the amplifier and the SiPM together, a test measurement has been developed using a laser system [74]. The laser allows to generate pulses with a time resolution of about 10 ps. Its light has been guided to the sensors with the help of an optical fiber. The sensorboards and the amplifiers are installed without the scintillating fiber ribbons. The laser has been attenuated so far that single photon measurements were possible.

5.6.1 Single Sensor Time Resolution

With a laser repetition rate of 100 kHz the optical fiber has been aligned to irradiate all sensors. Figure 5.21 shows the distribution of the time difference measured with two SiPMs on the same board. The distribution width includes the DAQ error itself (cf. section 5.3.2) and the contribution from the SiPMs and the amplifiers. Within one

DRS board the uncertainty is

$$\sigma_{\text{SiPM}} = \frac{\sigma_{\Delta t}}{\sqrt{2}} = \frac{277\,\text{ps}}{\sqrt{2}} = 196\,\text{ps}. \tag{5.10}$$

The result has been crosschecked with a second measurement where the laser is set to a much higher repetition rate of 77 MHz (fig. 5.22). In this measurement the time difference between two peaks is measured using only one sensor. The time resolution calculates as in eq. (5.10) to $\sigma_{\text{SiPM}} = 190\,\text{ps}$. This is in agreement with the first measurement.

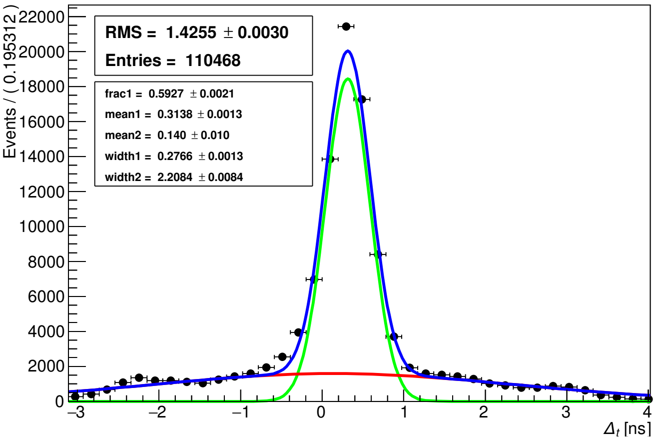

Figure 5.21: Time difference between two sensors for the same signal on the same DRS board.

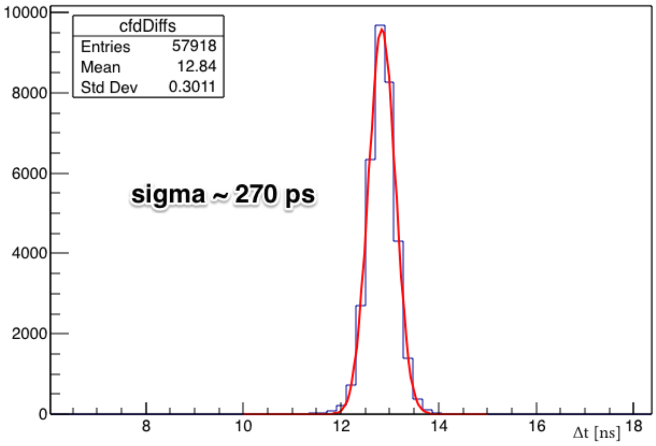

Figure 5.22: Distribution of the time difference between two subsequent signals measured with one sensor only.

5.6.2 Time Resolution Using Several Readout Boards

The jitter between the DRS boards has also been investigated with the laser. In this analysis all sensors have been irradiated with the laser. Figure 5.23 shows the distribution of the time difference between a sensor on board 2 and board 6. The resulting time resolution using this two sensors is

$$\sigma_{\Delta t} = 400\,\text{ps} \Rightarrow \sigma_{\text{channel}} = \frac{\sigma_{\Delta t}}{\sqrt{2}} = 283\,\text{ps}. \tag{5.11}$$

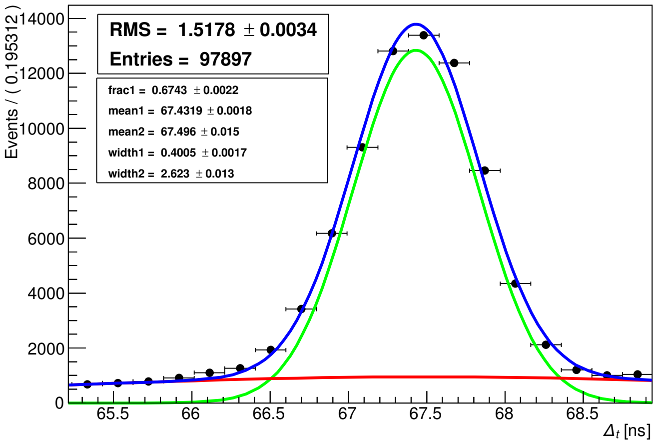

Figure 5.23: Time distribution for two sensors being separated by six boards. The additional background originates from crosstalk signal as the laser was irradiating all the sensors.

The result can be compared with the jitter propagation estimated from eq. (5.9) and eq. (5.10). The error from the two sensors on the same board propagated with six times the board jitter of 132 ps leads to an overall error of 420 ps which is in good agreement with the 400 ps from the laser measurement.

6

Fiber Ribbon Characterization

This chapter discusses properties of individual fibers such as light yield, absorption along the fiber and timing as well as properties when they are glued together as ribbons. For the ribbons the efficiencies and optical crosstalk is measured. All results shown in this chapters are gained using scintillation light by the energy deposition of electrons within the fibers.

6.1 Test Environments

6.1.1 Irradiation with an ^{90}Strontium Source

First measurements are done irradiating the fibers with the β^- emitter ^{90}Sr. Due to the low energy of the electrons (below 0.546 MeV/c for the ^{90}Sr electrons and below 2.28 MeV/c for the ^{90}Yttrium daughter nucleus) the ribbon could only be irradiated through the four layers. The trigger behind the ribbon is not only used to start the data acquisition but also to ensure that no signals are recorded where the electrons have stopped in the fiber.

The source has been placed in a lead collimator with an exit hole diameter of 1 mm close to the fibers in the ribbon. It is needed to reduce background by irradiating surrounding fibers and to reduce signals from gammas resulting in signal events directly in the photomultiplier tubes of the trigger. The trigger cross is placed directly after the fibers. The collimator and the trigger are moved along the fiber z-axis (cf. fig. 4.10) to measure the dependency of the photon yield along the fiber.

6.2 The πM1 Test Beam Area at the Paul Scherrer Institute

Several test beams campaigns have been performed at the PSI πM1 test beam area. The 590 MeV/*c* protons of the ring cyclotron are collided with the *M-target* at PSI. It is a rotating 5 mm thick carbon target. The secondary particles from the target are extracted to the πM1 beamline providing electrons, muons and pions (fig. 6.1).

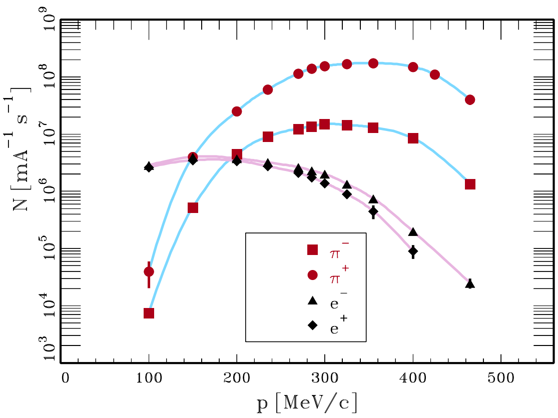

Figure 6.1: Particle flux rates at the πM1 beamline. The muon flux is in general about 100 times smaller than the pion flux [75].

The provided momentum range reaches from about 100 MeV/*c* to 500 MeV/*c*. For the measurements a momentum was chosen such that a good particle separation as described later in section 6.4 is possible in the offline data analysis. All measurements have therefore been done with 161 MeV/*c*. The high particle momentum allowed to irradiate the ribbon tilted to a horizontal position. In this configuration the particle crossing of sixteen fibers in a row is possible. The holder for the fibers has been designed to allow using the horizontal orientation without a collision of the beam with the aluminum frame (fig. 6.2).

The fiber ribbon was placed in the focus of the beam where the beam spot has a width of about 2 cm. The same trigger cross as used in the laboratory is placed again after the fiber ribbon. For the alignment of the trigger a laser is used as it has only to be aligned with an accuracy of 1 cm. A misalignment of the trigger would only lead to a decreased flux of particles through the trigger. As the data acquisition rate is limited to 50 Hz it is not needed to position the trigger with the highest possible flux rate. But the ribbon itself has to be aligned with respect to the trigger by an $\mathcal{O}(1\,\mathrm{mm})$ accuracy. This alignment is much more crucial as it needs to be such that the trigger records as many events as possible where the active part of the ribbon is crossed by the particle beam. It is done by first aligning the ribbon with the laser. The ribbon is then moved

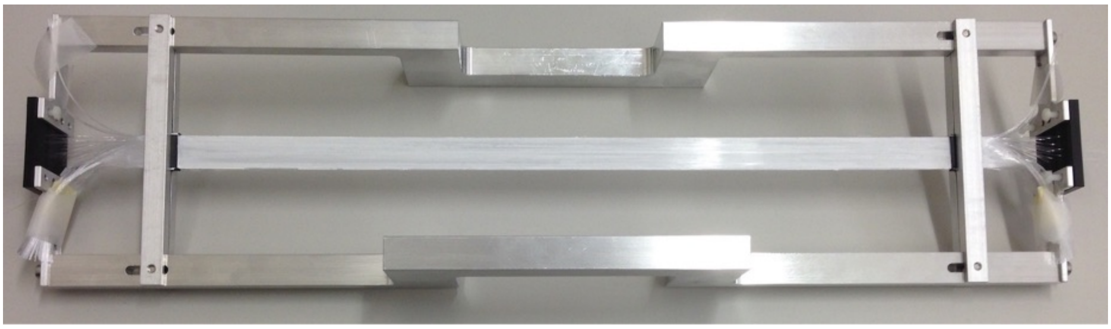

Figure 6.2: Picture of the improved holder for the fiber ribbons. The middle part allows the beam to pass the holder also in horizontal orientation without hitting the aluminum structure.

in 1 mm steps in height up and down relative to the trigger and the number of all measured photons is counted by recording the same amount of events. A histogram showing the measured number of photons as a function of the ribbon position is used the find the best alignment. The best position is at the maximum of this histogram (fig. 6.3). This procedure is repeated every time the orientation of the ribbon has been changed or when it has been moved to the side.

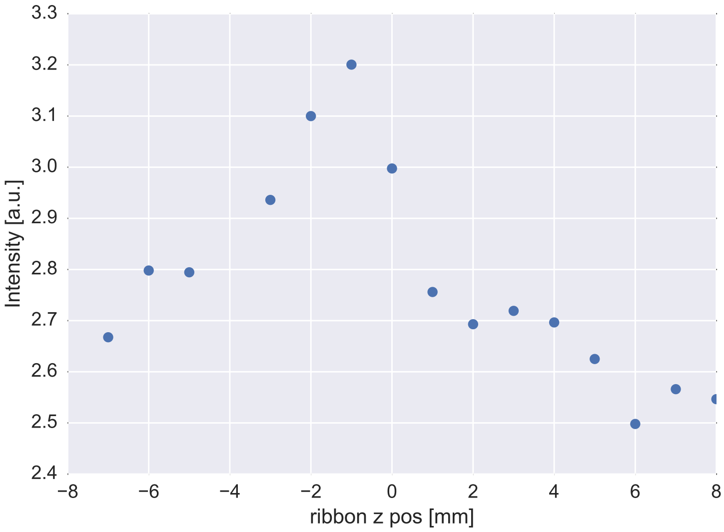

Figure 6.3: Measured number of photons depending on the relative position of the ribbon with respect to the trigger. The peak indicates the position with an optimal alignment.

All measurements at PSI show an increased level of noise. Figure 6.4 top left shows a recorded event without a SiPM signal and therefore background noise only. With the help of a discrete Fourier transformation the recorded noise has been analyzed (fig. 6.4 right). Peaks at 50 MHz and 150 MHz indicate that the amplifier picks up the radio frequency (RF) signal from the accelerator cavities of the 590 MeV/c ring cyclotron.

A crosscheck of the origin of the noise is done by summing up the signals of 1000 events for one channel aligned relative to the provided RF signal of PSI. The sum is compared to a superposition of two sinusoidal waveforms with 50 MHz and 150 MHz with the amplitudes given from the Fourier spectrum. The comparison in fig. 6.4 shows a good agreement with the theory that the originates from the cavities and that it is present in all events and correlated to the RF-phase. Electrical noise due to pickup as shown in this example shows the importance to use the signal integral to calculate the number of photon (cf. section 5.4.2) in a signal as the sinusoidal part of the noise cancels out. Possible effects from the signal on the time resolution are discussed in section 6.6.

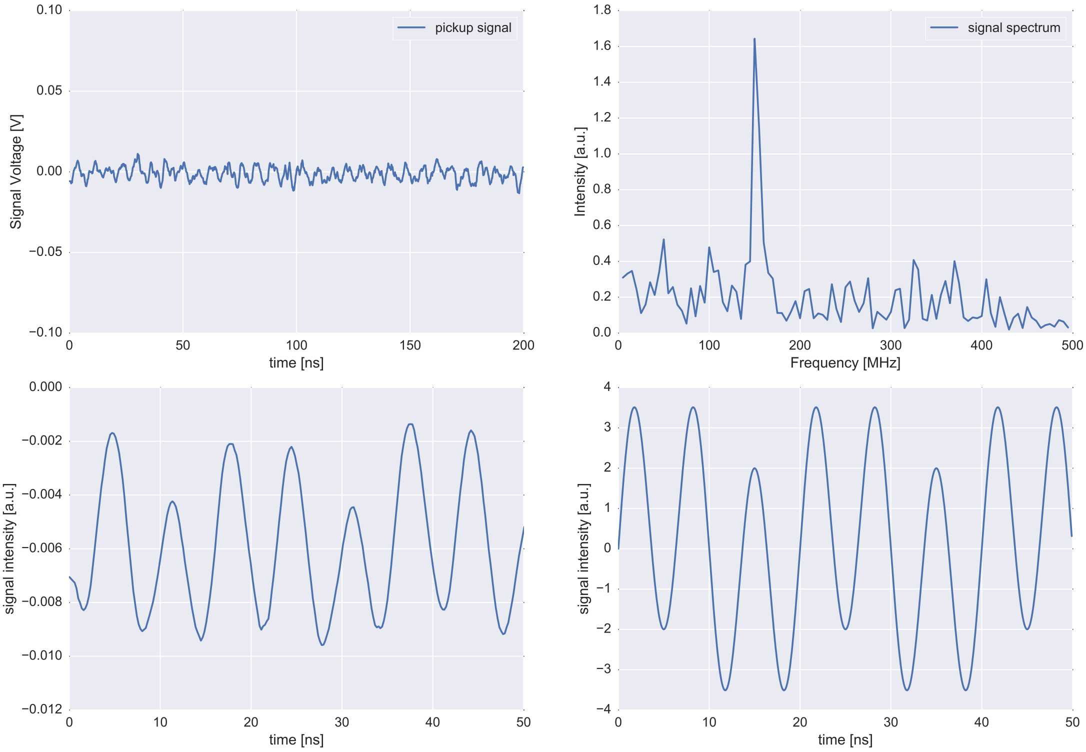

Figure 6.4: Example of the background noise due to pickup from the PSI accelerator cavities. The signal waveform *(top left)* shows an event without a SiPM signal. The frequency spectrum *(top right)* shows clearly the 50 MHz signal of the four acceleration cavities and the 150 MHz signal of the flattop cavity of the ring-cyclotrone. A comparison of the phase correlated sum of 1000 background events *(bottom left)* is done with a superposition of two sine waves of 50 and 150 MHz with the amplitudes corresponding to the Fourier spectrum *(bottom right)*.

6.3 Signal Analysis

The data processed as described in section 5.4 needs further processing. A flexible and adaptable software package to interpret the data has been written that allows to use it for different test scenarios as test beams or laboratory measurements. Due to the high number of channels and scenarios the signal analysis focuses on automation as far as possible. With the proper monitoring tools the quality can be assured for all measurements. A dedicated software class dealing with further signal calibration has been written. It is used for all test series.

6.3.1 Data Acquisition Time Window Selection

As the buffer of the DRS is 200 ns long the region of interest needs to be specified. A narrower region in the time base helps to suppress dark count signals (important for the efficiency analysis) and it helps to associate the right signal in case the particle rate through the ribbon is high enough to produce multiple signals within the 200 ns buffer. A histogram is generated of all time signals from all sub-signals over all events that have been recorded. From the peak in this histogram a time window of ± 10 ns has been specified (fig. 6.5, left). For all the rest of the analysis only signals within this window are considered as signals belonging to this event.

6.3.2 Photon Calibration

Each SiPM and each channel of the amplifier has a different gain. Depending on environmental noise and the specific version of the amplifier electronics the gain of the amplifier has been set to different values for different test series. The resulting channel specific gain and the high number of channels demands an automatic calibration system that shows the correlation between the signal integral and the number of photons measured by the sensor. For each channel a histogram is generated for all signal integrals from the sub-signals located within the time-window specified in the previous section. The highest peak and all local peaks that are higher than 5 % of the highest peak in the histogram are searched. In the integral histograms the highest peak specifies the signal for one photoelectron. The subsequent peaks show the signals for two and more photoelectrons. The gain of the SiPM and the amplifier is high enough that the peaks are clearly separated from each other. The value exactly in the middle of two peaks in the integral spectrum is used to determine the boundary for the number of photoelectrons. For the signals higher than the last peak found the signal-to-photoelectron windows are extrapolated from the previous peaks as the signal integral increases linearly with the number of photoelectrons (fig. 6.5, right).

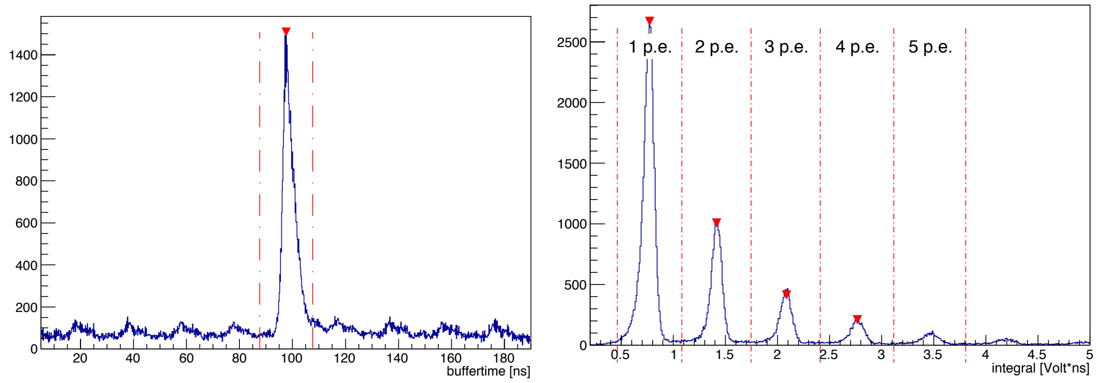

Figure 6.5: *Left:* Histogram of the time distribution of all signals for one channel. The red lines show the specified region of interest. In this example there are a lot of small peaks in 20 ns distance visible as expected from the PSI test beam rate. *Right:* Histogram of all sub-signals within the time acceptance window. The red dashed lines show the window boundaries for the corresponding number of photoelectrons.

6.4 Particle Identification

The beam at the PSI (cf. section 6.2) does not only provide electrons but also muons and pions. A selection between the particle types cannot be done a priori and therefore the recorded data contains events from all three particles. To distinguish the three particles in the data analysis, the 50 MHz signal of the ring acceleration cavities (the RF-signal) is recorded at the trigger-board (fig. 6.6, left). This information allows to use a particle identification (PID) feature implemented in the analysis software. The time difference between the trigger signal and the time when the RF-signal undershoots a specific threshold[1] for the first time is used to generate a histogram as shown in fig. 6.6, right. With the knowledge of the distance between the target and the trigger scintillator and the momentum of the particles, the time of flight differences modulo 20 ns can be specified and compared to the distribution. The momentum (acceptance) of the secondary particles is given by the beam line settings and was set for all measurements at PSI to 161 MeV/c. This setting allows a good separation of the muons, pions and electrons. With

$$\beta = \frac{p}{\sqrt{p^2 + m^2}} \quad \text{and} \quad t = \frac{1}{\beta c} \tag{6.1}$$

---

[1] To simplify matters the same algorithms as for the SiPM signals are used to split the RF-signal into sub-signals. As the amplitude of the sine is constant the threshold time as defined in section 5.4.3 is used.

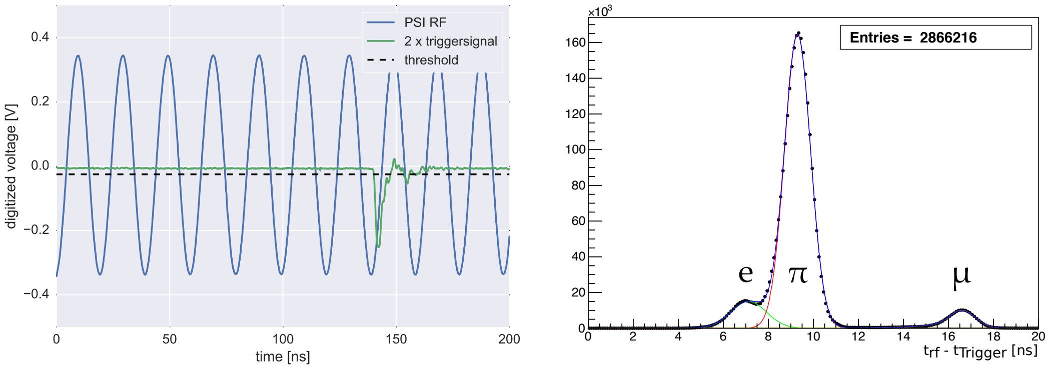

Figure 6.6: *Left:* Sample of a recorded event with the digitized PSI RF signal and the trigger. The trigger signal is scaled in this plot by a factor of two for better visibility. *Right:* Particle separation using the time difference between the accelerator frequency and the trigger signal.

the time of flight and therefore the difference to the RF-signal is given by the distance $l = 21\,\mathrm{m}$ between the target and the trigger and the selected momentum (fig. 6.7). If PID is used the window is set to 1σ from each peak to separate particles. The matching from the peak to the specific particle needs to be done by hand. It depends on the run specific beam settings like the specified momentum and the position of the trigger scintillators along the beam axis.

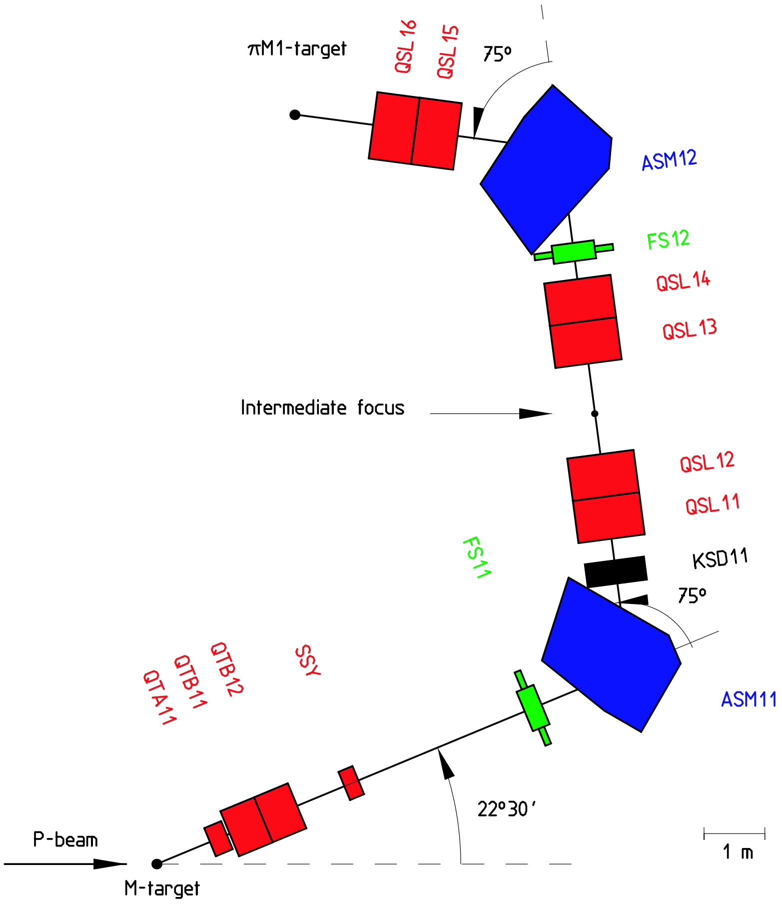

Figure 6.7: Schematic of the πM1 beamline after the carbon target M. The focusing magnets are shown in red and the dipole magnet for the momentum selection are in blue. The shutter elements shown in green can be used to reduce the beam intensity. The length of the beamline is 21 m from the target to the focal point in the experimental area [75].

6.5 Photon Yield

6.5.1 General Considerations

One important reason for the test measurements is to have the opportunity to compare the photon yield between the simulation and the measurement. The information allows to compare the simulation results and to improve them. In the simulation the crossing of the particle is well known and can be controlled. In the test environment the situation is more complicated. As the trigger of the system is a 1 mm thick scintillator it covers several fibers. The round shape of the fibers also means that the particle crosses different amounts of material and do therefore deposit different amounts of energies within the fiber. The photon yield for one fiber is essentially a convolution of the distribution of the path length in the active area with the landau distribution of the energy deposit $\mathrm{d}E/\mathrm{d}x$ per path length. As the fiber's active area is smaller than the trigger, the measurements lead to a lot of empty entries for a specific fiber. This must not be mistaken with inefficiencies of the fibers.

To make a comparison of the simulated data as described in section 4.6 and the measurements done at PSI at a single fiber level all data has been histogrammed by ignoring the bin for zero photons. Hence events that did fire the trigger but actually missed the fiber under investigation do not account to the histogram. All measured data has been reduced to events with electrons only (cf. section 6.4).

Simulation Results

The results of the simulation of the light yield under the PSI beam conditions are shown in fig. 6.8. In this simulation not only the complete setup and beam conditions have been implemented as described in section 4.6 but also the quantum efficiency of the SiPM is taken into account. The light yield for three different distances between the fiber end and the position where the electrons cross the fiber are simulated. As expected the mean number of photons decreases with increasing distance between the sensors and the fiber crossing.

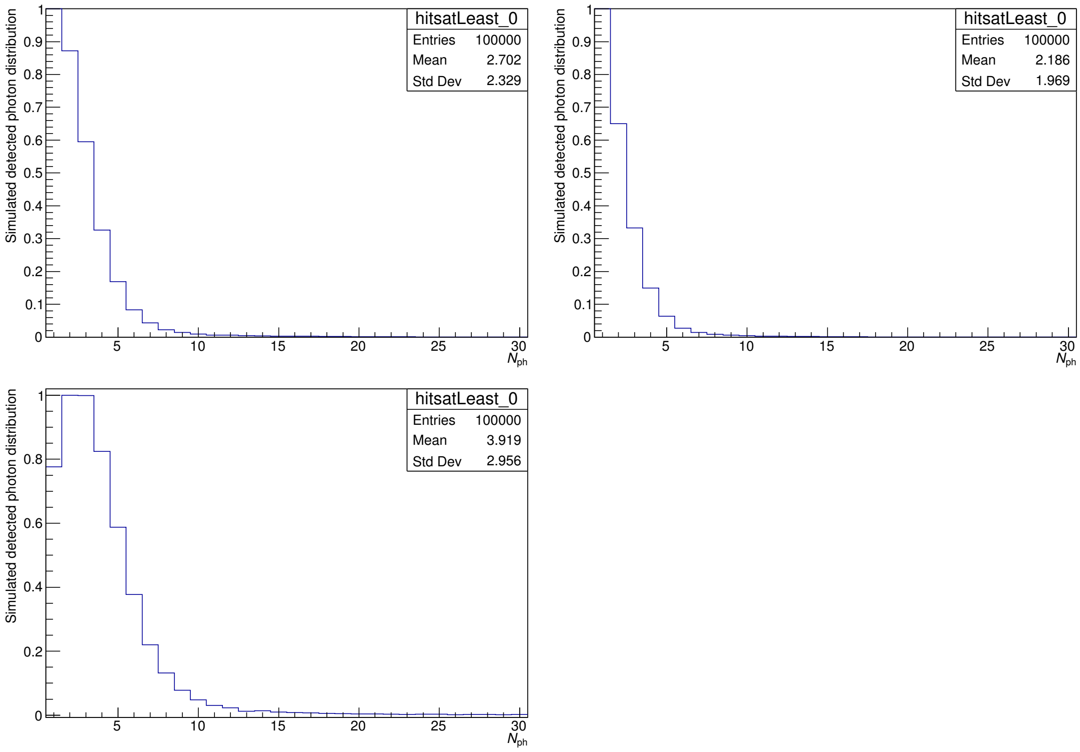

Figure 6.8: Distribution of the predicted photons per event by simulating the crossing of a 49.5 cm long fiber at three different distances to the sensors. The histogram top left shows the light yield at a distance of 24.75 cm, the top right histogram shows the results at 42.25 cm and bottom left at 6.75 cm. The refraction index and the quantum efficiency of the SiPM are taken into account.

Measured Photon Yield

For a comparison of the simulation the ribbon has been placed in the PSI test-beam at the same distances. For the middle distance (i.e. 24.75 cm) the results are shown in fig. 6.9, for the far distance (i.e. 49.5 cm) in fig. 6.10 and for the close distance in fig. 6.11. The results show that the measured data shows less light than expected from the simulation. Looking at the mean number of photons the measured average for all fibers is 2.0 ± 0.1, 2.2 ± 0.1 and 2.5 ± 0.1 (for the far, middle and close distance) photons per event, whereas in the simulation there are 2.2, 2.7 and 3.9 photons predicted. The measurements show only 92 %, 82 % and 63 % of the predicted light. The results for all fibers are summarized in table 6.1.

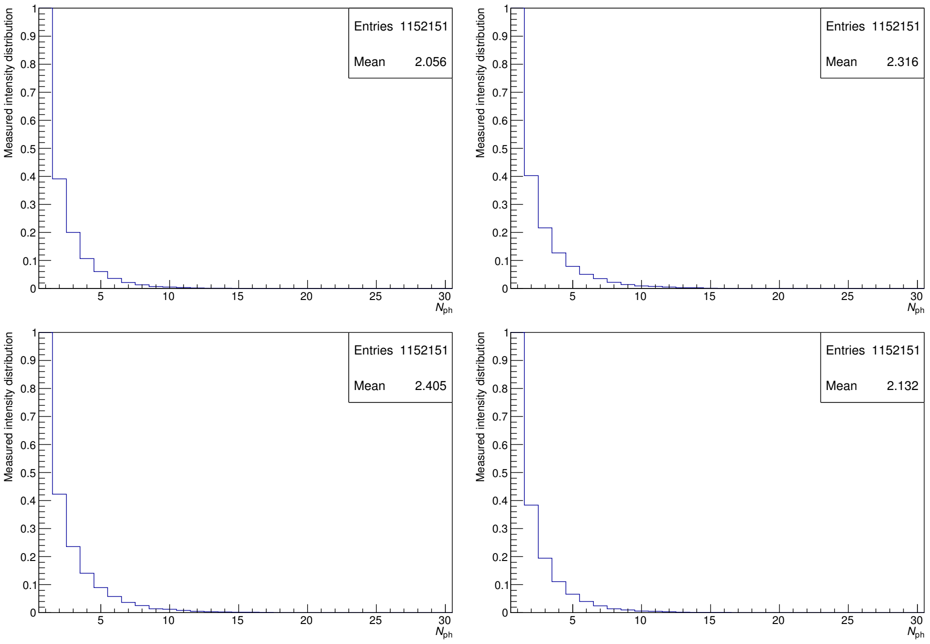

Figure 6.9: Measured distribution of detected photons per event by crossing a 49.5 cm fiber ribbon in the middle with 161 MeV/c electrons. The results are shown for four different fibers.

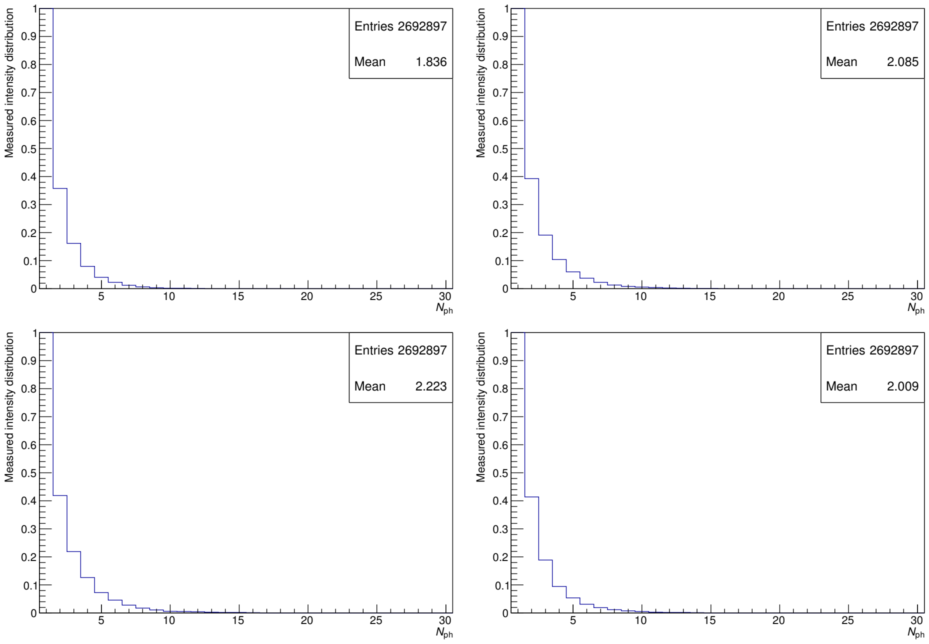

Figure 6.10: Measured distribution of detected photons per event by crossing a 49.5 cm fiber ribbon at a distance of 42.25 cm from the sensors with 161 MeV/c electrons. The results are shown for four different fibers.

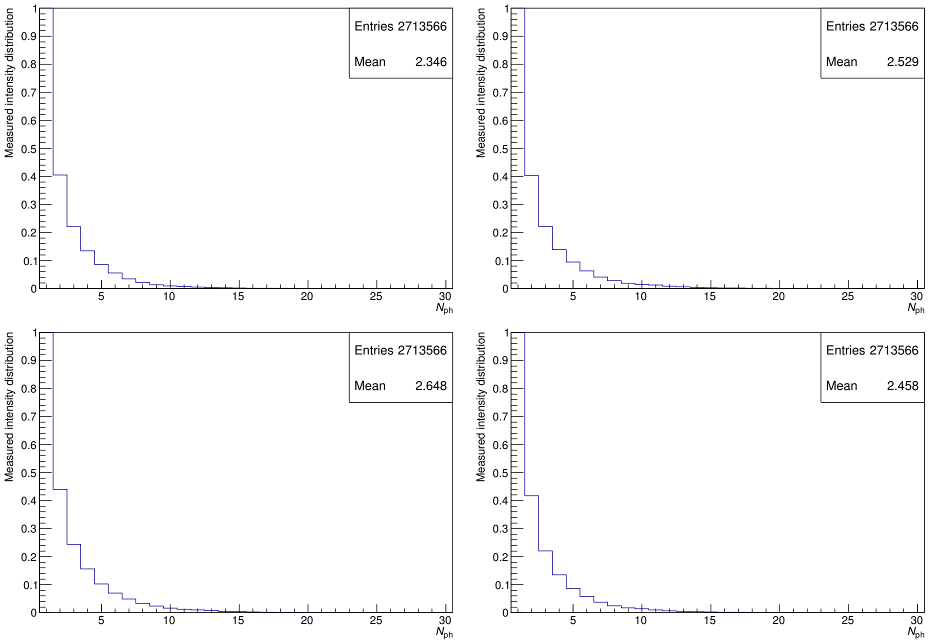

Figure 6.11: Measured distribution of detected photons per event by crossing a 49.5 cm fiber ribbon at a distance of 6.75 cm from the sensors with 161 MeV/c electrons. The results are shown for four different fibers.

Table 6.1: Summary of the mean light yield measured with ribbon (A) at PSI for the distances between light sensors and fiber crossings of 24.75 cm (middle), 6.75 cm (close) and 42.25 cm (far).

fiber	middle	far	close	fiber	middle	far	close
1	2.1	1.9	2.3	9	2.1	1.9	2.4
2	2.2	2.1	2.5	10	2.2	1.9	2.4
3	2.3	2.1	2.5	11	2.2	1.9	2.5
4	2.1	2.0	2.4	12	2.3	2.1	2.5
5	2.1	1.8	2.4	13	2.1	1.9	2.4
6	2.3	2.1	2.5	14	2.2	2.0	2.5
7	2.4	2.2	2.7	15	2.2	1.9	2.4
8	2.1	2.0	2.5	16	2.5	2.2	2.7

The source of the discrepancy can be of several reasons. The simulation can contribute in two ways: Either the simulation overestimates the production of the scintillating light in general, or more photons are absorbed or lost while simulating their propagation to the fiber end. Especially due to the fact that the fibers are quite long ($\mathcal{O}(10\,\mathrm{cm})$) compared to the thickness ($\mathcal{O}(100\,\mu\mathrm{m})$) the transportation needs to be simulated with high accuracy. This problem is analyzed more in detail in section 6.5.2 and could actually be excluded.

Also for the measurements possible systematic errors are needed to be discussed. As discussed more in detail in section 6.5.4 a bad coupling between the fibers and the sensors or a bad quality of the fibers can lead to a decreased light yield. Non linearity effects in the gain of the SiPM that would lead to a wrong calibration of the signal into the number of photons or saturation effects as described in eq. (3.5) can be excluded as there are only a couple of photons expected.

The histograms of the measured data show much more entries in the bin for one photon than the simulation. Dark counts generated by the SiPM can have a contribution to this bin. Even though a lot of effort has been made to suppress these effects (cf. section 6.3.1), it can not be excluded that in some events where the electron actually missed the fiber and the event should have been ignored has been taken into account because of a dark count in the sensor. The same argumentation counts for optical crosstalk within the fibers (cf. section 6.5.3). Events that released the trigger where the electron crosses another fiber can produce light in the fiber under investigation due to optical crosstalk. Therefore a closer look in the effect of the bin of one photon is needed. For this the weighted mean for two and more photons is calculated. In the case for two or more photons the mean is 3.3 ± 0.1, 3.5 ± 0.1 and 3.9 ± 0.1 (for the far, middle and close measurement). The values are summarized in fig. 6.12. In a simplified assumption where the landau distribution of the energy deposit and the fact, that the electron can cross the fiber with different thickness is neglected, the photon yield can be described by a Poisson distribution where the probability P to see events with k photons is given by:

$$P(k,\lambda) = \frac{\lambda^k e^{-\lambda}}{k!} \tag{6.2}$$

with λ being the expectation value. The expectation value is set in this way that the weighted mean of the Poisson distribution corresponds to the mean in the simulation and the measurements counting from one or two and more photons is the same. If the mean is calculated starting from one photon the simulation generates a corresponding expectation value of 1.84, 2.48, 3.83 (for the far, middle and close simulation, table 6.2 provides a summary for all values). Starting with only two and more photons the corresponding λ for the simulated mean are 2.34, 2.89 and 4.13. The measurements lead to values for λ to 1.60, 1.87 and 2.19 if the mean is calculated from the first photon bin. Compared to the simulation this means that only 88 %, 75 % and 57 % of the expectation value are measured. Using the weighted means for two or more photons the values for λ get 2.56, 2.93 and 3.41 for the measurements. Hence the expectation value from the measurements are 110 %, 101 % and 83 % of the simulated values. The better agreement between simulation and measurements by ignoring the one photon events indicates a systematic error in the measurements.

Table 6.2: Expectation value λ for a Poisson distribution leading to the same weighted mean within the interval of ≥ one or ≥ two photons.

	far	middle	close
≥ 1 photon simulation	1.84	2.48	3.83
≥ 1 photon measurement	1.60	1.87	2.19
≥ 2 photon simulation	2.34	2.89	4.13
≥ 2 photon measurement	2.56	2.93	3.41

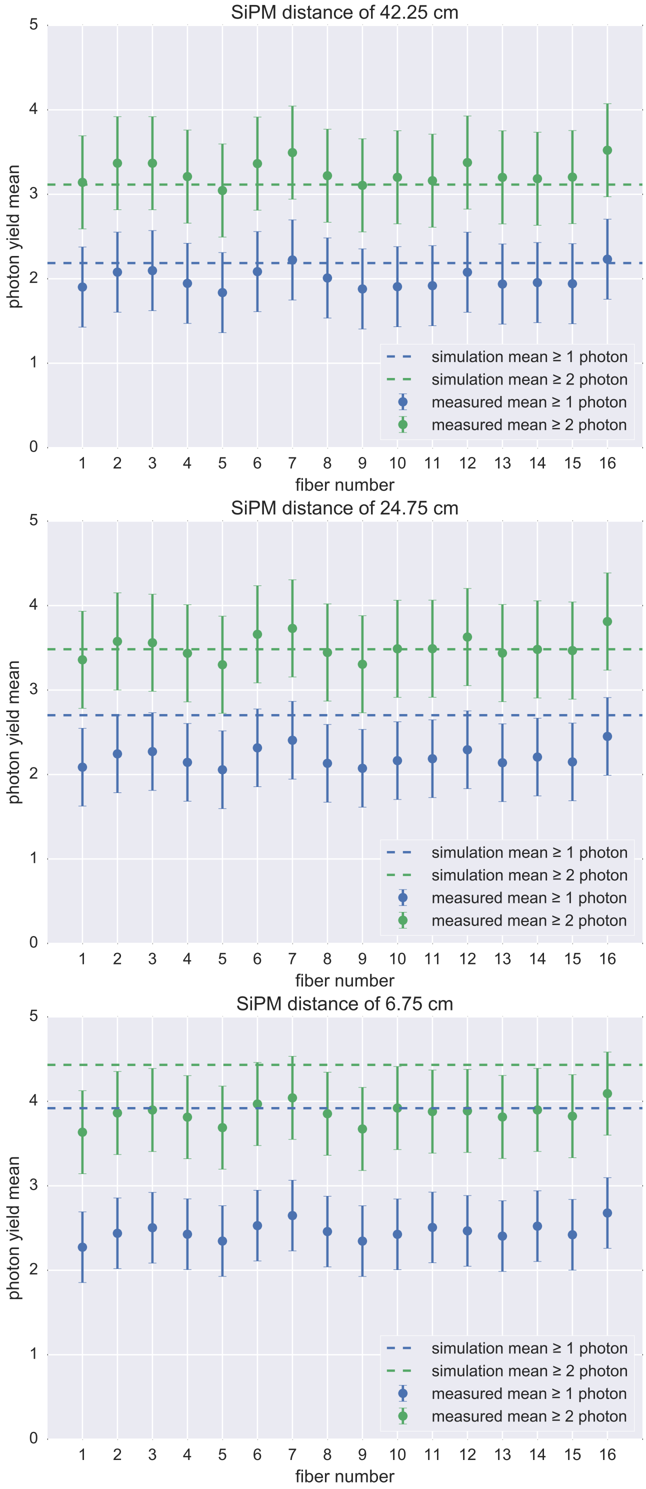

Figure 6.12: Comparison of the weighted mean of the photon yield for the simulation and the measurements counting from one receptively two and more photons. The results are shown for all fibers.

6.5.2 Attenuation along the Fiber

The attenuation of the amount of light depending on the fiber position has been compared with the simulation. As the simulation consists mainly of the photon production and trapping first and the propagation along the fiber afterwards, it is important to analyze these two aspects individually. A better understanding of how well the attenuation is simulated helps to understand the source of the discrepancy between the simulated and measured light yield.

Two measurements are done at different z-positions (pos. a and pos. b) of the ribbon with a distance in between of 355 mm. For both measurements the photon yield histograms (hist. a and hist. b), as introduced in section 6.5.1, have been recorded for one end of the fiber. The data from the histogram a, i.e. the measurement closer to the sensor is used as an input for a theoretical attenuation. For the given distance between the two measurements, the attenuation factor predicted by the simulation can be calculated with eq. (4.4) as 0.475 for 355 mm. Each entry in a bin from hist. a represents an event where n photons have been registered, where n is the bin value. The histogram is processed in such a way as that for all photons of each event the probability is calculated that they will be detected at the end after an additional traveling of 355 mm. This procedure generates a new histogram (hist. c) which can be compared to the second measured data from the far measurement (hist. b) (i.e. where the particles crossed the sensors 355 mm farther away).

The fact that in this analysis only the attenuation factor of the simulation is used, makes further assumptions like the detector quantum efficiency or the quality of the coupling between the sensor and the fiber unnecessary, assuming that the values stay constant. Figure 6.13 shows the comparison between the measurement and simulation. A good agreement between data and simulation shows that the propagation along the fiber has been simulated properly and therefore the implementation of the fiber surface as discussed in section 4.2 is properly done.

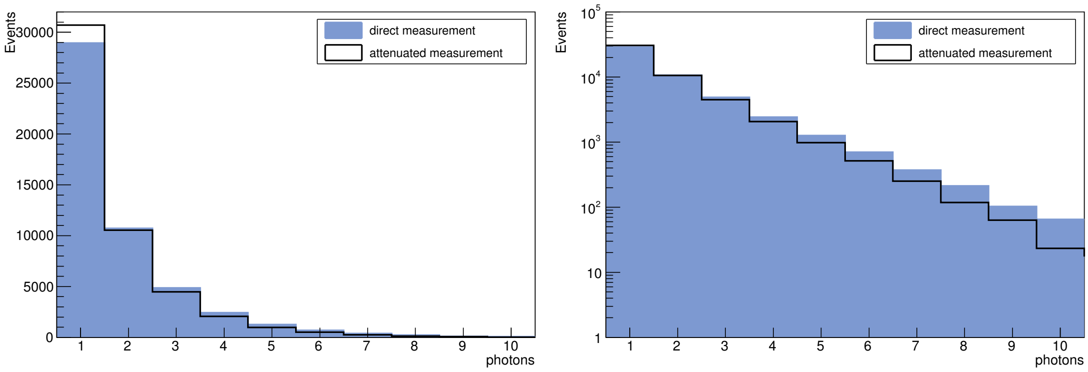

Figure 6.13: Comparison of the light attenuation along the fiber (linear scale left and logarithmic scale right). The data measured with the higher distance is shown in blue (defined as hist *b* in the text) and the attenuated data from the close measurement (hist *c*) in white.

6.5.3 Crosstalk Studies

Especially for an uncoated ribbon the crosstalk needs to be understood properly. On the one hand the crosstalk can worsen the time resolution of the signal and moreover be a problem for the data rate in the DAQ system. The studies shown in this section focus on optical crosstalk only. Electrical crosstalk in the DAQ system is not analyzed in this section as the DAQ system used here will not be used in the final detector design. But it has made sure that electrical crosstalk signals will not be counted as photons by accident.

Figure 6.14 shows an example for the crosstalk analysis. In this measurement the ribbon is irradiated in the middle with electrons from a ^{90}Sr source. It shows the fraction of events where at least one photon is detected in the other fibers while demading at least one photon at one side of fiber a. The electrons crossing fiber a will also cross either one of the fibers b (except when the particle crosses exactly in between them). The high fraction of events with light in the fibers b is therefore not induced by optical crosstalk. The closest fibers for which crosstalk can be studied are fibers c. Those show crosstalk probabilities of up to 20 %.

Crosstalk depends on the position of the layer in the ribbon. Outside layers have neighbors on one side only. The inside layer has neighbors on both sides (cf. fig. 6.15). The crosstalk probability for outside layers is on average $(11 \pm 3)\,\%$, for the inside layer we observe $(18 \pm 3)\,\%$. For the next neighbors the crosstalk is $(8.3 \pm 1.4)\,\%$ and $(5.0 \pm 1.6)\,\%$, respectively

There are two possible contributions that can produce signals that are wrongly interpreted as crosstalk. The first contribution can be dark counts. As we are dealing

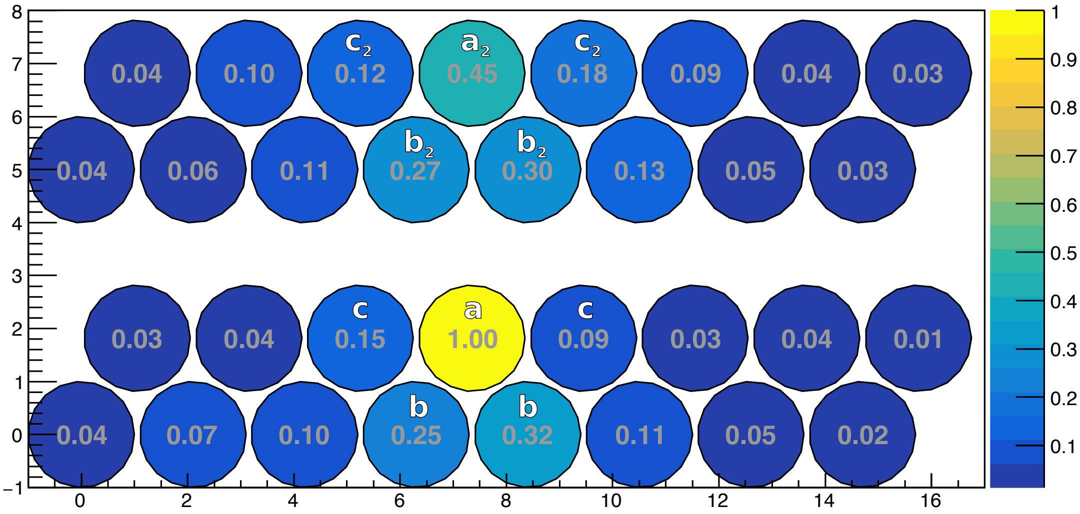

Figure 6.14: Crosstalk study for the fiber a. The figure shows fraction of events that have been registered by looking at the fiber a. The numbers in gray show the fraction of how often a photon has been detected in each fiber in a event where there is at least 1 photon in fiber a. The two separated rows show both ends of the fiber ribbon. The fibers b have the highest ratio as they fire also because the electron will pass fiber a and one of the fiber b. The fibers c are the closest where the ratio shows actual optical crosstalk. The fibers a_2, b_2 and c_2 show the corresponding other end of the fiber. The particle crosses in the middle of the ribbon.

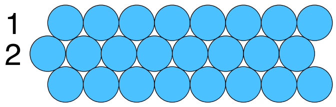

Figure 6.15: Position of the fibers under investigation within the whole ribbon.

with signals at the level of one photon it needs to be taken into account that the dark counts of the SiPM sensor contribute to the number of measured photons in the other fibers. This effect of accidental coincidences will falsify the crosstalk studies. As the time window where a photon is accepted to a certain event[2], is narrowed to 20 ns this effect is suppressed. With a typical dark-count rate of $1 \cdot 10^5$ counts per second at a 0.5 photoelectron level, the expected probability to see also a fake contribution to the cross talk is about $2 \cdot 10^{-3}$.

The second contribution that might falsify the measurement is the probability to have several electrons passing the fibers within the 20 ns time window. The source that has been used has an activity of 37 MBq. To make an estimation of the fake crosstalk rate in this scenario the source is assumed to be a point source radiating

---

[2] cf. section 6.3.1

isotropically. The minimal distance between the source and the fibers is the length of the collimator tunnel that is $r = 5\,\mathrm{mm}$. The electron flux at 5 mm is

$$\varphi_e = \frac{37 \cdot 10^6 \frac{e^-}{\mathrm{s}}}{4\pi r^2} \approx \frac{1.1 \cdot 10^5 e^-}{\mathrm{s\,mm}^2} \tag{6.3}$$

with the diameter of the collimator hole $d = 4\,\mathrm{mm}$ the maximum area covered by a fiber is $A = 4\,\mathrm{mm} \times 0.25\,\mathrm{mm}$ and a time window of $t_w = 20\,\mathrm{ns}$ the probability to have another electron in a fiber is

$$\varphi_e \cdot A \cdot t_w \approx 2 \cdot 10^{-3}. \tag{6.4}$$

The two estimations show that they can contribute to the crosstalk measurement at the 1 % level. Looking at the crosstalk analysis for a fiber at the corner of the ones under investigation (fig. 6.16) this effect is visible for the fibers far away from the one under investigation.

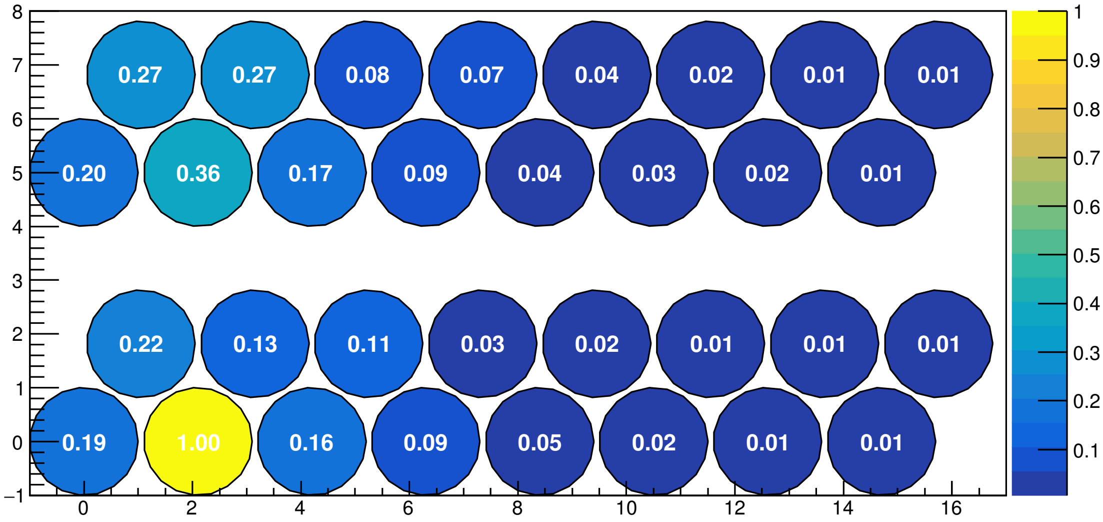

Figure 6.16: Crosstalk showing also some fake-crosstalk hits in fibers far away from the crossed fiber due to the high decay rate of the source used in the laboratory and dark counts of the sensors.

6.5.4 Efficiencies

The measurement of the detection efficiency of each fiber is done by positioning the ribbon in a horizontal orientation. In this orientation the particle crosses all fibers in a row per event (cf. fig. 6.17). As there was no external trigger of the size of the fibers this orientation has been chosen to use the ribbon itself as a trigger. The material that needs to be traversed is much thicker in this orientation and therefore only PSI measurements can be used. The particle energies are high enough to cross all the fibers and to ensure that no particle is stopped within the fiber. The momenta of the ^{90}Sr-source[3] electrons are too low to allow also measurements in the laboratory.

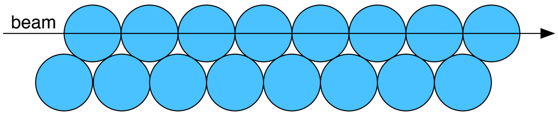

Figure 6.17: Orientation of the ribbon with respect to the beam. For efficiency measurements the orientation of the ribbon is horizontal.

The measuring principle for the different fibers is shown in fig. 6.18. For each fiber a cluster of three fibers is used consisting of the fiber under investigation and its two nearest neighbors. The efficiency is calculated by the ratio of how many events show at least one photon in the middle fiber when the two neighboring fibers show at least one photon each. This way a particle crossing trough the middle fiber can be ensured.

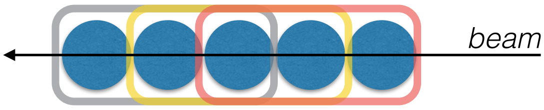

Figure 6.18: Principle of the efficiency measurement. For each fiber a cluster of three fibers is used (grey, yellow, red in this example) to specify the efficiency of the fiber in the middle of a cluster.

Table 6.3 shows the result for all fibers under investigation. Averaged over all fibers the single fiber efficiency is 0.65 ± 0.09. The results show that the fiber efficiency varies a lot between different channels. This can be possibly explained by two reasons. On the one hand there can be a large variety in the fiber quality caused by imperfections in the production process. Especially the extremely thin fiber cladding can be destroyed by improper handling. Also crazing, as discussed in section 3.1.1, can be a problem as the ribbons are manufactured manually. In this case the manufacturing procedures need to be improved. The second potential problem source is bad coupling of the

---

[3] and the electrons of the beta decay of the daughter nucleus ^{90}Y

fibers to the sensors. Especially in the case of single photon experiments a geometric misalignment, dirt or bad polishing can have strong influence on the efficiency. The use of optical grease has not been envisaged as the transparency of the grease tends to degrade in time. A better coupling would certainly be reached by glueing the fibers to the sensors. In this early R&D stage with only one ribbon available and different sensors to be tested glueing was, however, no option. If the fibers with an efficiency lower than 0.6 are considered as broken (cf. fig. 6.19) and only the fibers above this threshold are taken into account the single fiber efficiency rises to 0.69 ± 0.03.

Table 6.3: Single fiber efficiency. The values show the probability of detecting a photon in the middle fiber when there is a photon detected in the two surrounding fibers.

fiber	eff	fiber	eff	fiber	eff	fiber	eff
1	0.73	7	0.47	13	0.65	19	0.72
2	0.64	8	0.72	14	0.64	20	0.55
3	0.68	9	0.50	15	0.69	21	0.74
4	0.70	10	0.51	16	0.65	22	0.70
5	0.68	11	0.37	17	0.71	23	0.71
6	0.70	12	0.74	18	0.66	24	0.67

As the final experiment will have more than one layer of fibers the efficiencies for two and three layers have been estimated as well. In case of two layers new clusters including four fibers have been used for measuring the efficiency. The probability to observe at least one photon in one of the two middle fibers (OR) when the two outer fibers show at least one photon each defines the new efficiency. The measured results are shown in table 6.4.

Table 6.4: Efficiencies for two fibers. The values show the probability of detecting a photon in one of the middle fibers (OR condition) when there is a photon detected in the two surrounding fibers. These results are measured with two subsequent fibers.

pair	eff	pair	eff	pair	eff	pair	eff
1	0.87	6	0.82	11	0.84	16	0.83
2	0.84	7	0.84	12	0.85	17	0.85
3	0.86	8	0.72	13	0.84	18	0.90
4	0.86	9	0.66	14	0.86	19	0.89
5	0.87	10	0.82	15	0.86	20	0.87

The results can be crosschecked by with the single fiber efficiencies. The probability to observe a signal in at least one of the two fibers ϵ_2 can be predicted from the measured single-fiber detection efficiency ϵ_1.

$$\epsilon_2 = 1 - (1 - \epsilon_1)^2 \tag{6.5}$$

These predicted values vary typically 0.86 ± 0.08 (table 6.5) in agreement with the measured 0.84 ± 0.05.

With the same ansatz the efficiencies for three fibers have been calculated. All results are summarized in fig. 6.19. The predicted values are overall 0.95 ± 0.05 and if we skip the fibers considered to be broken it even reaches 0.97 ± 0.01.

Systematic errors in the efficiency measurement can also be induced by optical crosstalk. The high crosstalk probability can produce additional trigger events from where the electron actually passes another row. Such events shift the measured efficiency to a lower value. Therefore the efficiencies stated in this section are considered as a lower limit.

Table 6.5: Extrapolated double fiber efficiencies. These results are the extrapolated values from eq. (6.5) using the measured single fiber efficiencies. Each fiber is treated as it would appear twice.

fiber	eff	fiber	eff	fiber	eff	fiber	eff
1	0.93	7	0.72	13	0.88	19	0.92
2	0.87	8	0.92	14	0.87	20	0.80
3	0.90	9	0.75	15	0.90	21	0.93
4	0.91	10	0.76	16	0.88	22	0.91
5	0.90	11	0.60	17	0.92	23	0.92
6	0.91	12	0.93	18	0.88	24	0.89

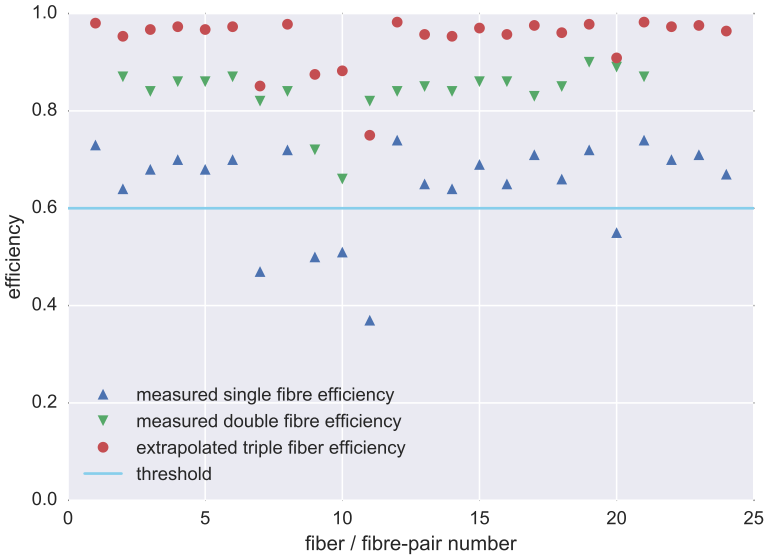

Figure 6.19: Cluster efficiency for electrons. The blue line highlights the threshold where the fibers are considered broken or where the coupling to the sensor was bad.

6.6 Time Resolution

In this section the measured time resolution for single fibers is discussed. It is important to check the simulation results and if the combinatino of the fibers with the signals generated by SiPMs can be used to make a accurate time measurement. The time information for each fiber is extracted as described in section 5.4.3 by using the FlashCam like algorithm. Time measurements below the ns scale are difficult insofar as the accuracy of all electronic components need to be considered too. For this measurements it is decided to do always relative measurements to eliminate as many sources of inaccuracy as possible. The time resolution is measured by doing a histogram of the *time differences* of the two corresponding sensors of one fiber. A possible jitter of the trigger itself or moreover a jitter in the triggering function of the DRS evaluation board[4] do not affect the measurements therefore. The trigger propagation within the DRS boards on the other side is well understood. For the time resolution results in this section the trigger needs to propagate through four boards to measure the time for the two corresponding fiber ends. The total error contribution by the DAQ system and the SiPMs themselves in the time difference measurement, here defined as σ_{DAQ}, is then (cf. section 5.3.2)

$$\sigma_{\mathrm{DAQ}} = \sqrt{2\sigma_{\mathrm{SiPM}}{}^2 + 4\sigma_{\mathrm{interboard}}{}^2} \approx 380\,\mathrm{ps}. \tag{6.6}$$

6.6.1 Test Beam measurements

The first measurement with an uncoated ribbon has been done at PSI. Due to a defective amplifier on one side of the ribbon, only four fibers have been analyzed. Figure 6.20, fig. 6.21 and fig. 6.22 show the distributions of the time difference (as discussed in section 6.6) for the four different fibers where a threshold of at least one, two and three photons is set. The results in table 6.6, table 6.7 and table 6.8 are defined as described in section 4.4 where "σ_{Δ_t}" is the value of the equivalent Gaussian with the same width, "σ_{se}" shows the time resolution looking at one single fiber end $\left(\sigma_{\Delta_t}/\sqrt{2}\right)$, "$\sigma_{\mathrm{be}}$" the time resolution by averaging over both fiber ends $\left(\sigma_{\Delta_t}/2\right)$.

---

[4] the latter is also excluded by defining the own time stamp out of the digitized trigger signals. So done for the time walk measurements in section 5.4.3.

One Photon Time Resolution

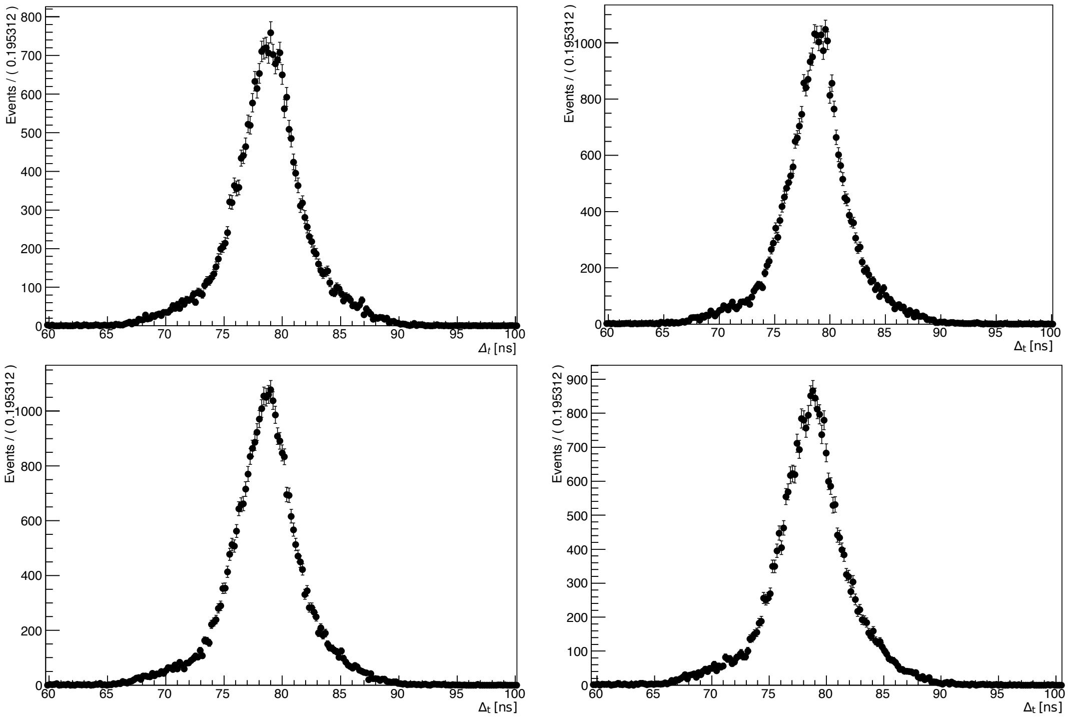

Figure 6.20: Time difference between the left and the right fiber end measuring at least one photon. The results for four different fibers are shown.

Table 6.6: Time difference between the left and the right fiber end measuring at least one photon.

fiber	FWHM [ns]	σ_{Δ_t} [ns]	σ_{se} [ns]	σ_{be} [ns]
1	5.1	2.2	1.5	1.1
2	4.7	2.0	1.4	1.0
3	5.1	2.2	1.5	1.1
4	5.3	2.2	1.6	1.1

Two Photon Time Resolution

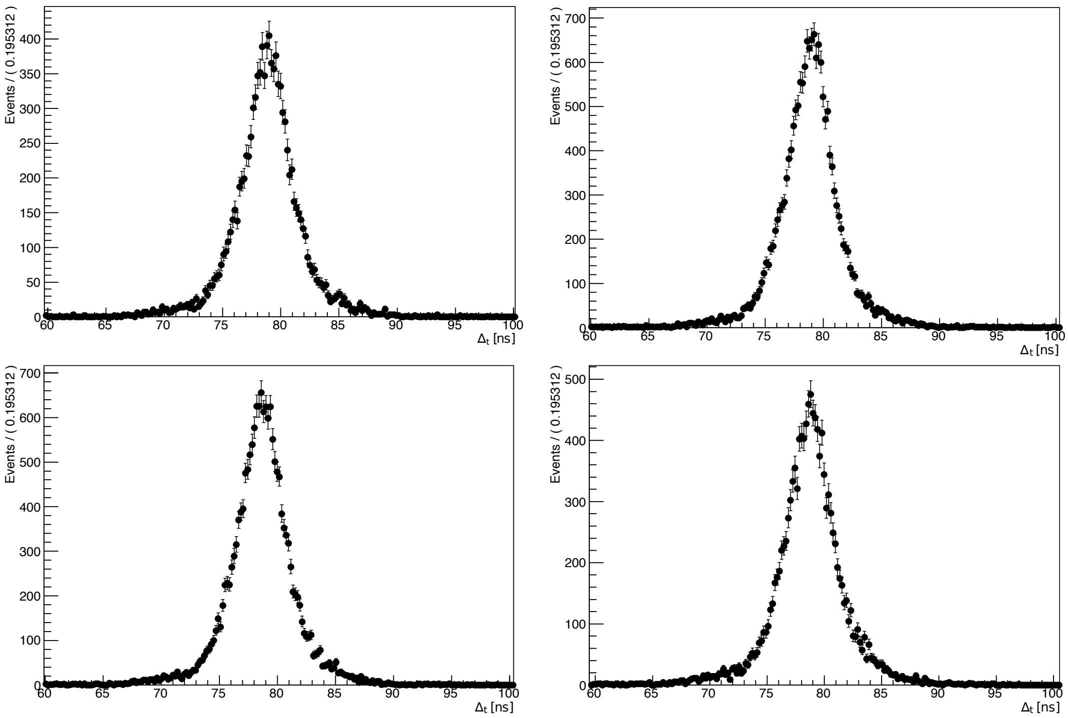

Figure 6.21: Time difference between the left and the right fiber end measuring at least two photons.

Table 6.7: Time difference between the left and the right fiber end measuring at least two photons.

fiber	FWHM [ns]	σ_{Δ_t} [ns]	σ_{se} [ns]	σ_{be} [ns]
1	4.2	1.8	1.2	0.9
2	3.9	1.7	1.2	0.8
3	4.1	1.8	1.2	0.9
4	4.2	1.8	1.3	0.9

Three Photon Time Resolution

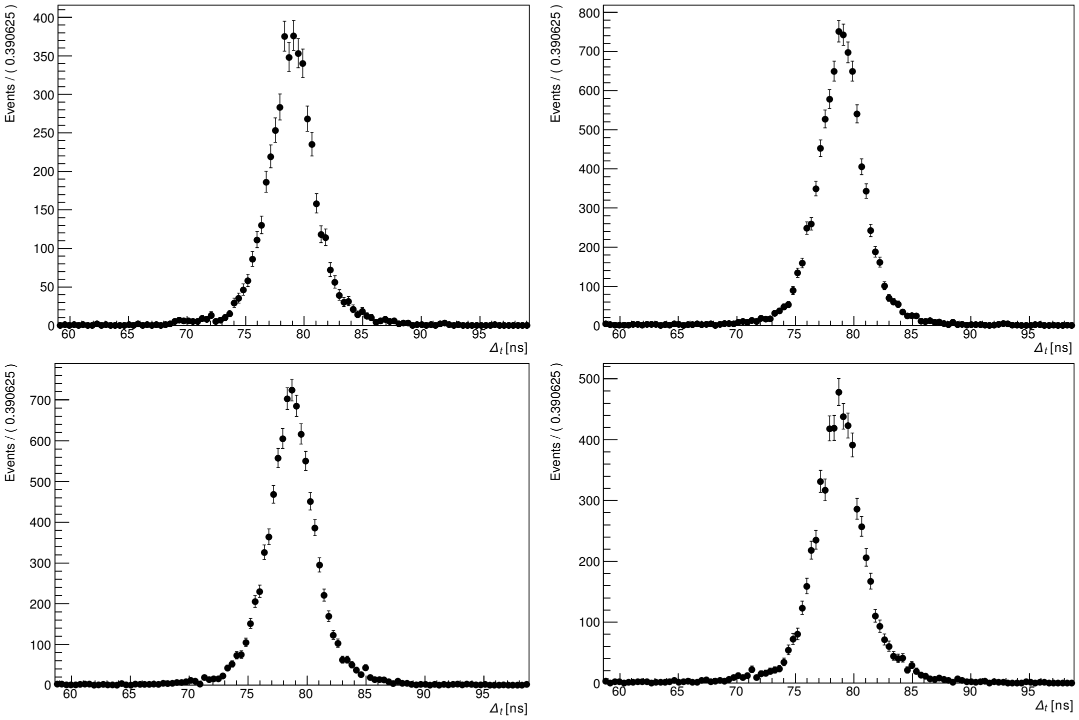

Figure 6.22: Time difference between the left and the right fiber end measuring at least three photons.

Table 6.8: Time difference between the left and the right fiber end measuring at least three photons.

fiber	FWHM [ns]	σ_{Δ_t} [ns]	σ_{se} [ns]	σ_{be} [ns]
1	3.7	1.6	1.1	0.8
2	3.7	1.6	1.1	0.8
3	3.8	1.6	1.1	0.8
4	3.8	1.6	1.2	0.8

The results from the PSI measurement show that at a single photon level the time resolution is (1.07 ± 0.05) ns when using the double end readout. The result is slightly higher than expected from the simulation. The inaccuracy from the DAQ has a minor effect. Using the width from the time difference measurement, the error from the DAQ can be subtracted by

$$\sigma_{\Delta_t} = \sqrt{{\sigma_{\text{measured}}}^2 - {\sigma_{\text{DAQ}}}^2} \tag{6.7}$$

That leads to a time resolution using both fiber ends of

$$\sigma_{\text{be}} = \sigma_{\Delta_t}/2 = (1.06 \pm 0.05)\,\text{ns}. \tag{6.8}$$

As expected the accuracy of the DAQ system plays a minor role. Hence the corrected result is still higher than expected from the simulation. As discussed in section 6.2 a possible source is the pickup from the PSI accelerator. In the next section the measurement is repeated with a source in the laboratory to clarify whether the noise has an impact or not.

6.6.2 LABORATORY COMPARISON

The same ribbon has been irradiated with a ^{90}Sr-source to make a comparison of the time resolution measured in the laboratory to the results measured at PSI. The setup is as explained in section 6.1.1 and the same ribbon has been used. For four fibers the results are shown.

ONE PHOTON TIME RESOLUTION

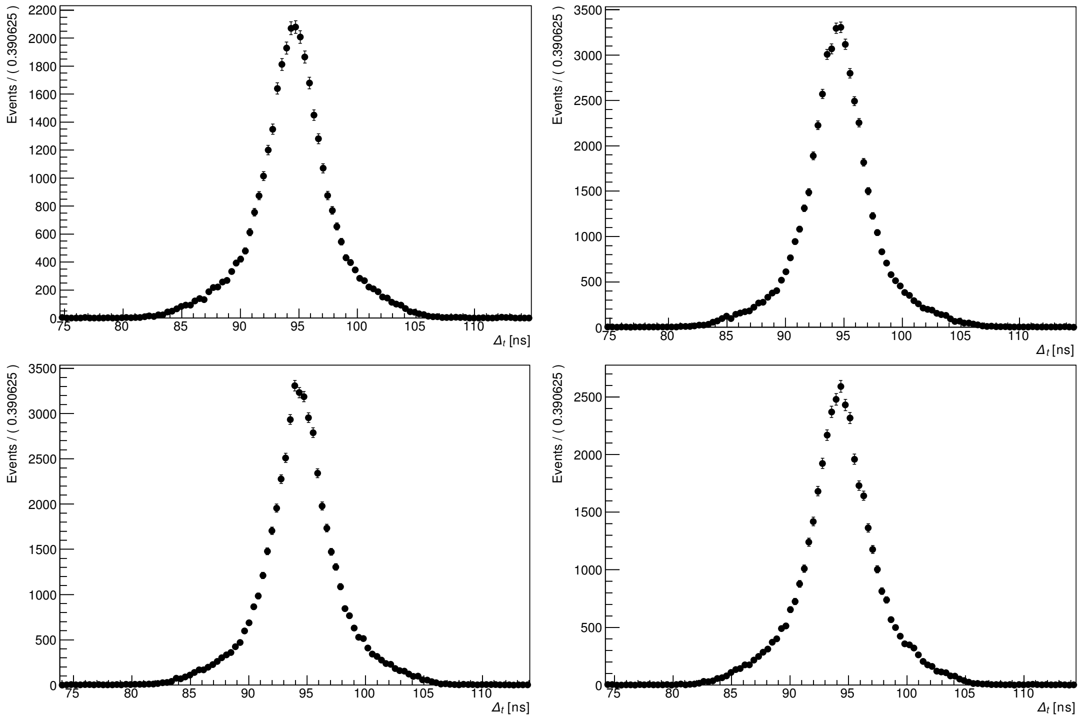

Figure 6.23: Time difference between the left and the right fiber end with at least 1 photons, lab Sr source.

Table 6.9: Time difference between the left and the right fiber end with at least 1 photons, lab Sr source.

fiber	FWHM [ns]	σ_{Δ_t} [ns]	σ_{se} [ns]	σ_{be} [ns]
1	5.1	2.2	1.5	1.1
2	4.6	2.0	1.4	1.0
3	4.9	2.1	1.5	1.0
4	5.2	2.2	1.6	1.1

Two Photon Time Resolution

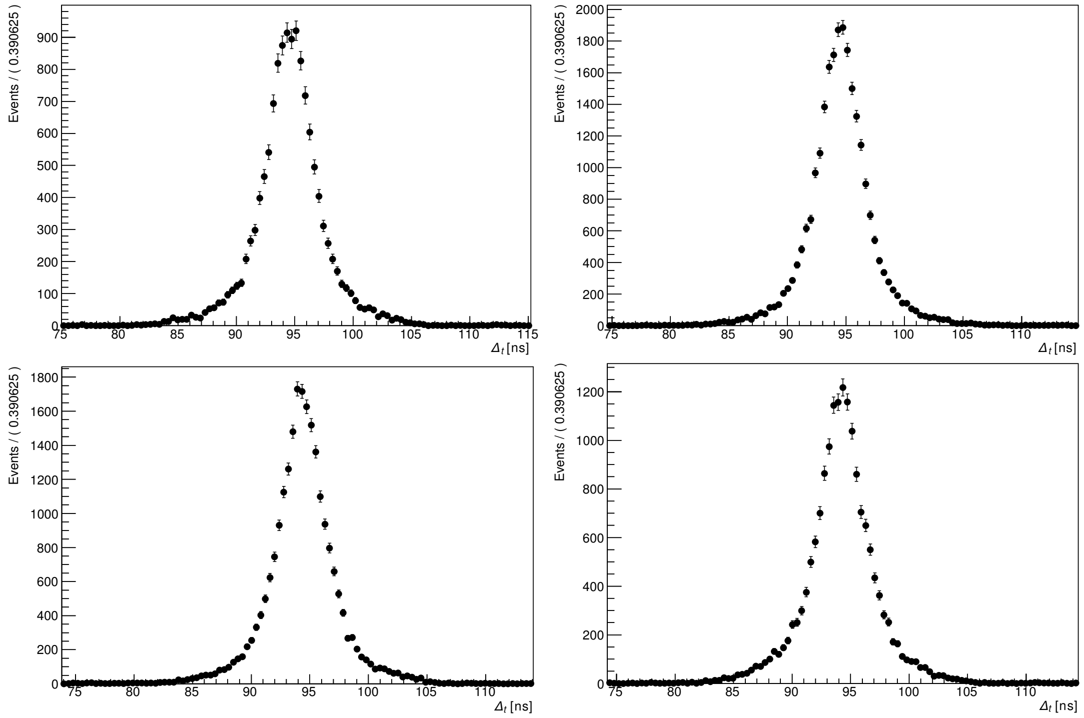

Figure 6.24: Time difference between the left and the right fiber end with at least 2 photons, lab Sr source.

Table 6.10: Time difference between the left and the right fiber end with at least 2 photons, lab Sr source.

fiber	FWHM [ns]	σ_{Δ_t} [ns]	σ_{se} [ns]	σ_{be} [ns]
1	4.2	1.8	1.3	0.9
2	3.9	1.7	1.2	0.8
3	4.0	1.7	1.2	0.9
4	4.2	1.8	1.2	0.9

Three Photon Time Resolution

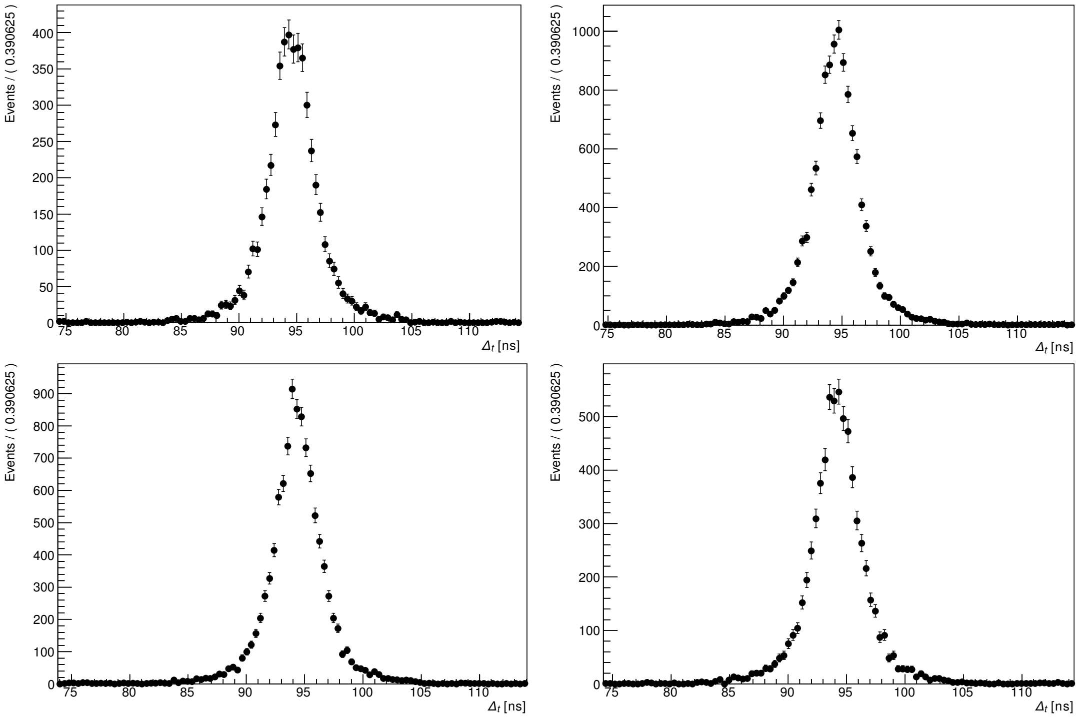

Figure 6.25: Time difference between the left and the right fiber end with at least 3 photons, lab Sr source.

Table 6.11: Time difference between the left and the right fiber end with at least 3 photons, lab Sr source.

fiber	FWHM [ns]	σ_{Δ_t} [ns]	σ_{se} [ns]	σ_{be} [ns]
1	3.8	1.6	1.1	0.8
2	3.6	1.5	1.1	0.8
3	3.6	1.5	1.1	0.8
4	3.7	1.6	1.1	0.8

6.6.3 Summary on the Time Resolution

The results show the same time resolution in the lab as measured at the PSI. The signal post-processing and especially the timing algorithm is able to produce the same results under noisy conditions. On the other hand the measurements show that even though the simulation tries to simulate realistic conditions it overestimates the accuracy of the fibers by 0.2 ns to 0.3 ns.

Errors coming from the DAQ system are excluded and also there is no impact of external electrical noise. One contribution that can broaden the distribution of the time difference would be an additional source of photons. It is known for SiPMs that they produce light by themselves in case of an avalanche [76, 77]. Usually this phenomenon is known as optical crosstalk within a SiPM (not to be confused with optical crosstalk within the fibers). In first preliminary measurements with the STiC chip it has been shown that these photons can be mediated by a fiber from one SiPM to the opposing one on the other side of the same fiber [37].

Figure 6.26 shows the temporal distribution of events triggered on a threshold of two photons between two SiPMs connected with a fiber and between two SiPMs that are attached to two different fibers. As the fibers were not exposed to a radioactive source or in a beam, one expects a flat distribution of uncorrelated dark-counts produced by both SiPMs. For the two SiPMs on the same fiber two peaks are visible. In this case the fiber acts like a classic optical transmission fiber. The impact of this effect on the overall time-resolution of the fiber system has not been studied yet. As such effects are not included in the simulation they are one possible reason to explain the better results compared to the measurements.

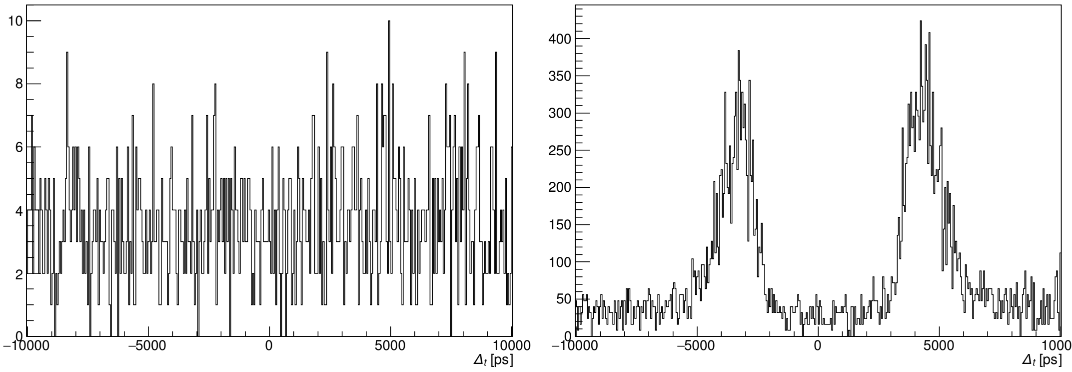

Figure 6.26: Time difference between signals of two SiPMs. The left graph shows the time distribution of two SiPM connected to different fibers, while in the right graph the two SiPMs are connected to both sides of the same fiber. The fibers were not exposed to a source. The peaks are not symmetric around zero because of a wrong absolute zero setting of the STiC chip [37].

7

Conclusion

The content in this thesis aims to provide on the one hand a general simulation package that can be used to get a better understanding of the fiber response in the proposed Mu3e experiment and on the other hand a realistic proposal for the scintillation fiber detector is investigated. The results will be used to describe the round fiber detector for the technical design report that is expected by the end of 2016.

7.1 SIMULATION

7.1.1 PHOTON YIELD

The comparison between the simulation and the measurements show that the simulation shows good agreement in the description of the transport losses along the fiber. Measurements show a reduced number of photons down to a factor of 63 %. Systematic errors in the measurements, in particular too many events with only one photon measured, lead to an underestimation in the photon yield. These errors can originate from dark-counts produced by the SiPM and optical crosstalk effects. It could also not been excluded that photon losses between the fiber and the SiPM have an impact on the measurements. Experiments with such low photon yields are extremely sensitive to noise and the coupling of the fibers to the sensors. Therefore the parametrization of the dedicated fiber simulation has not been adapted to the results from the measurement done at PSI.

7.1.2 Time Resolution

The time resolution that is achievable with such a system is simulated with a high accuracy level. In the comparison between the simulation and the measurements gives a discrepancy of 300 ps, even under the realistic noisy conditions in the test-beam area which is similar to the proposed location of the final experiment. Up to now no results of the timing study have been implemented in the main simulation of the experiment. In the current simulation the time signal is generated only by using the time when the particle deposits energy within the fiber. This time is then smeared with a Gaussian distribution at a fixed width. Effects of how many photons are measured are not taken into account. For a conservative measurement the timing resolution for events at a single photon level are suggested to implement.

7.2 Feasibility for the Mu3e Experiment

7.2.1 Phase I

The proposed fiber detector shows a single fiber time resolution of 1.0 ns to 1.1 ns. With a design goal of < 1 ns [5] the performance is at the upper limit for single fibers. Only measurements demanding two or more photons on each end of the fibers lead to a time resolution below 1 ns. As a consequence a column wise readout of the fiber ribbons is envisaged for the phase I of the experiment to increase the light yield. This can be achieved by using cluster algorithms that find the corresponding hits of one track within several fibers. Which fibers are passed by the electrons depends on the position where the particle crosses the fiber ribbon and on the angle relative to the ribbon (fig. 7.1). For a high efficiency three layers are needed at the minimum to achieve an efficiency up to (97 ± 1) %. Increasing the thickness of the fibers would lead to an increased light yield. Fibers with a diameter of 500 µm would already lead to an efficiency of about 91 %. Ribbons built with two layers of such thicker fibers that could also be read out column wise will therefore have a better time resolution. But due to the fact that such ribbons will be thicker ($\sim$ 933 µm, compared to three layer ribbons with thinner fibers that have a thickness of $\sim$ 683 µm) the impact on the

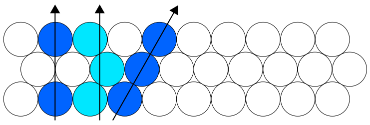

Figure 7.1: Schematic of the scintillation light produced in different fibers depending on the track position and angle. Dark blue indicates more light than bright blue.

overall momentum resolution of the experiments needs to be investigated as there is more material that causes multiple scattering. The TiO coating of the ribbons could not be tested as there were no functional ribbons available for this work. An increased trapping efficiency due to this additional reflector leads to a higher photon yield. The impact of the TiO coating on the light yield and time resolution is currently being investigated.

7.2.2 Phase II

Whether or not the proposed fiber detector can be used for the phase II of the experiment is currently under investigation by the collaboration. Detailed results of the impact of the fiber time resolution on the background suppression is expected to be published in the technical design report. Especially the time resolution that is not better than 1 ns will be a possible weak point of the current fiber design.

Prototyping with the alternative option of squared fibers, as mentioned in section 2.3.7 has also started at PSI [78]. The first prototype has a length of about 25 cm and each fiber is coated with an additional aluminum layer of 100 nm thickness. The aluminum acts as a mirror and improves the trapping efficiency (cf. fig. 3.3 in section 3.1.2) as photons that are emitted under an angle where no total reflexion happens can also be trapped. The fibers have been attached to the SiPMs by using optical glue to achieve a better coupling. With the short fibers a time resolution of 540 ps at single photon level is claimed. A similar prototype where the fibers have an total length of 50 cm shows a time resolution of 750 ps. The main reason for a better time resolution in these tests is most probably the increased photon yield. Even without the aluminum coating the fibers produce under ideal conditions, as how they were tested, more light due to the fact that a particle crosses always 250 µm of material. But this is only given by a perpendicular crossing of such a ribbon. As there is not only a perpendicular crossing of the ribbon (cf. fig. 4.19) the light yield in squared fibers will be less and therefore the time resolution will be worsened. Studies with complete ribbons of squared fibers that can be tested under different crossing angles are currently ongoing.

References

[1] G. Aad *et al.*, "Observation of a new particle in the search for the Standard Model Higgs boson with the ATLAS detector at the LHC," *Physics Letters B*, vol. 716, pp. 1–29, sep 2012.

[2] S. Chatrchyan *et al.*, "Observation of a new boson at a mass of 125 GeV with the CMS experiment at the LHC," *Physics Letters B*, vol. 716, pp. 30–61, sep 2012.

[3] "Wikipedia Standard Model Article." `https://en.wikipedia.org/wiki/Standard_Model`.

[4] F. Zwicky, "Die Rotverschiebung von extragalaktischen Nebeln," *Helvetica Physica Acta*, vol. 6, pp. 110–127, 1933.

[5] A. Blondel *et al.*, "Research Proposal for an Experiment to Search for the Decay $\mu \to eee$," *ArXiv e-prints*, Jan. 2013.

[6] N. Berger, "A novel experiment searching for the lepton flavour violating decay $\mu \longrightarrow$ eee," *Journal of Physics: Conference Series*, vol. 408, p. 012070, feb 2013.

[7] A. de Gouvêa and P. Vogel, "Lepton flavor and number conservation, and physics beyond the standard model," *Progress in Particle and Nuclear Physics*, vol. 71, pp. 75–92, 2013.

[8] R. Bernstein and P. S. Cooper, "Charged lepton flavor violation: An experimenter's guide," *Physics Reports*, vol. 532, pp. 27–64, nov 2013.

[9] Y. Fukuda *et al.*, "Evidence for oscillation of atmospheric neutrinos," *Phys. Rev. Lett.*, vol. 81, pp. 1562–1567, Aug 1998.

[10] Q. R. Ahmad *et al.*, "Measurement of the Rate of $\nu_e + d \to p + p + e^-$ Interactions Produced by ^8B Solar Neutrinos at the Sudbury Neutrino Observatory," *Phys. Rev. Lett.*, vol. 87, p. 071301, Jul 2001.

[11] K. Eguchi *et al.*, "First results from kamland: Evidence for reactor antineutrino disappearance," *Phys. Rev. Lett.*, vol. 90, p. 021802, Jan 2003.

[12] J. C. Pati and A. Salam, "Lepton number as the fourth color," *Phys. Rev. D*, vol. 10, pp. 275–289, Jul 1974.

[13] H. Georgi and S. L. Glashow, "Unity of all elementary-particle forces," *Phys. Rev. Lett.*, vol. 32, pp. 438–441, Feb 1974.

[14] P. Langacker, "Grand unified theories and proton decay," *Physics Reports*, vol. 72, no. 4, pp. 185 – 385, 1981.

[15] H. Haber and G. Kane, "The search for supersymmetry: Probing physics beyond the standard model," *Physics Reports*, vol. 117, no. 2, pp. 75 – 263, 1985.

[16] R. N. Mohapatra and J. C. Pati, "A natural left-right symmetry," *Phys. Rev.*, vol. D11, p. 2558, 1975.

[17] R. N. Mohapatra and J. C. Pati, "Left-right gauge symmetry and an isoconjugate model of cp violation," *Phys. Rev.*, vol. D11, pp. 566–571, 1975.

[18] G. Senjanovic and R. N. Mohapatra, "Exact left-right symmetry and spontaneous violation of parity," *Phys. Rev.*, vol. D12, p. 1502, 1975.

[19] M. Kakizaki, Y. Ogura, and F. Shima, "Lepton flavor violation in the triplet higgs model," *Physics Letters B*, vol. 566, no. 3–4, pp. 210 – 216, 2003.

[20] M. L. Brooks *et al.*, "New Limit for the Lepton-Family-Number Nonconserving Decay $\mu^+ \rightarrow e^+\gamma$," *Phys. Rev. Lett.*, vol. 83, pp. 1521–1524, Aug 1999.

[21] J. Adam *et al.*, "New Limit on the Lepton-Flavor-Violating Decay $\mu^+ \rightarrow e^+\gamma$," *Phys. Rev. Lett.*, vol. 107, p. 171801, Oct 2011.

[22] J. Adam *et al.*, "New constraint on the existence of the $\mu^+ \rightarrow e^+\gamma$ decay," *Phys. Rev. Lett.*, vol. 110, p. 201801, May 2013.

[23] U. Bellgardt *et al.*, "Search for the decay $\mu^+ \rightarrow e^+e^+e^-$," *Nuclear Physics B*, vol. 299, no. 1, pp. 1 – 6, 1988.

[24] W. Bertl *et al.*, "A search for μ-e conversion in muonic gold," *The European Physical Journal C - Particles and Fields*, vol. 47, no. 2, pp. 337–346, 2006.

[25] Y. Kuno and Y. Okada, "Muon decay and physics beyond the standard model," *Rev. Mod. Phys.*, vol. 73, pp. 151–202, 2001.

[26] W. J. Marciano, T. Mori, and J. M. Roney, "Charged Lepton Flavor Violation Experiments*," *Annual Review of Nuclear and Particle Science*, vol. 58, pp. 315–341, nov 2008.

[27] K. Olive, "Review of Particle Physics," *Chinese Physics C*, vol. 38, p. 090001, aug 2014.

[28] P. Eckert, *The Mu3e Tile Detector.* PhD thesis, Heidelberg University, 5 2015.

[29] N. Berger, "Simulation & reconstruction status." PSI Review Meeting, feb 2015.

[30] Mu3e Collaboration. Internal Wiki.

[31] "High Intensity Proton Accelerators (HIPA)." `https://www.psi.ch/ltp/facilities`.

[32] P.-R. Kettle, "Mu3e beam line status." PSI Review Meeting, Feb 2015.

[33] P.-R. Kettle. Internal Discussion.

[34] M. Hildebrandt, "Mu3e muon stopping target." Mu3e Collaboration Meeting, Sept 2014.

[35] I. Perić, "A novel monolithic pixelated particle detector implemented in high-voltage CMOS technology," *Nuclear Instruments and Methods in Physics Research Section A: Accelerators, Spectrometers, Detectors and Associated Equipment*, vol. 582, pp. 876–885, dec 2007.

[36] H. Augustin *et al.*, "The MuPix System-on-Chip for the Mu3e Experiment," Mar 2016.

[37] S. Corrodi. Internal Discussion.

[38] T. Harion *et al.*, "STiC — a mixed mode silicon photomultiplier readout ASIC for time-of-flight applications," *Journal of Instrumentation*, vol. 9, pp. C02003–C02003, feb 2014.

[39] W. Shen *et al.*, "STiC2 - characterization results of a SiPM readout ASIC for time-of-flight applications," in *2013 IEEE Nuclear Science Symposium and Medical Imaging Conference (2013 NSS/MIC)*, pp. 1–5, IEEE, oct 2013.

[40] D. Wiedner *et al.*, "The proposed trigger-less TBit/s readout for the Mu3e experiment," *Journal of Instrumentation*, vol. 9, pp. C01011–C01011, jan 2014.

[41] Y. T. Didenko, W. B. McNamara, and K. S. Suslick, “Effect of noble gases on sonoluminescence temperatures during multibubble cavitation,” *Phys. Rev. Lett.*, vol. 84, pp. 777–780, Jan 2000.

[42] G. Destriau, “AC electroluminesence in ZnS,” *J. Chem. Phys.*, vol. 33, p. 587, 1936.

[43] C. G. Camara, J. V. Escobar, J. R. Hird, and S. J. Putterman, “Correlation between nanosecond X-ray flashes and stick–slip friction in peeling tape,” *Nature*, vol. 455, pp. 1089–1092, oct 2008.

[44] C. W. E. van Eijk, “Inorganic scintillators in medical imaging,” *Physics in Medicine and Biology*, vol. 47, pp. R85–R106, apr 2002.

[45] C. W. van Eijk, “Inorganic scintillators in medical imaging detectors,” *Nuclear Instruments and Methods in Physics Research Section A: Accelerators, Spectrometers, Detectors and Associated Equipment*, vol. 509, pp. 17–25, aug 2003.

[46] J. Birks, *The Theory and Practice of Scintillation Counting*. Elsevier, 1964.

[47] J. Birks, “Scintillations from Organic Crystals: Specific Fluorescence and Relative Response to Different Radiations,” *Proceedings of the Physical Society. Section A*, vol. 64, pp. 874–877, oct 1951.

[48] B. D. Leverington, M. Anelli, P. Campana, and R. Rosellini, *A 1 mm Scintillating Fibre Tracker Readout by a Multi-anode Photomultiplier*, vol. 21. 2011.

[49] C. Grupen and I. Buvat, *Handbook of Particle Detection and Imaging*. Springer Berlin Heidelberg, 2012.

[50] C. Zorn, “Plastic and Liquid Organic Scintillators,” in *Instrumentation in High Energy Physics*, vol. 9 of *Advanced Series on Directions in High Energy Physics*, pp. 218–279, World Scientific, jun 1992.

[51] W. R. Leo, *Techniques for Nuclear and Particle Physics Experiments*. Springer Berlin Heidelberg, 1994.

[52] K. Kleinknecht, *Detektoren für Teilchenstrahlung*. Vieweg+Teubner Verlag, 2005.

[53] M. Krammer, “Detektoren in der hochenergiephysik.” University Lecture at Institut für Hochenergiephysik der ÖAW, 2009.

[54] “Wikipedia Benzene Article.” `https://en.wikipedia.org/wiki/Benzene`.

[55] Kuraray Co., Ltd., *Plastic Scintillating Fibers.*

[56] "Britney Spears' Guide to Semiconductor Physics." `http://britneyspears.ac/lasers.htm`.

[57] "What is a silicon photomultiplier?." `http://www.hamamatsu.com/jp/en/community/optical_sensors/sipm/what_is_sipm/index.html`.

[58] N. Otte, "The Silicon Photomultiplier-A new device for High Energy Physics, Astroparticle Physics, Industrial and Medical Applications," *Proceedings to SNIC symposium (SLAC, Stanford, ...*, no. April, pp. 1–9, 2006.

[59] J. Allison *et al.*, "Geant4—a simulation toolkit," *Nuclear Instruments and Methods in Physics Research Section A: Accelerators, Spectrometers, Detectors and Associated Equipment*, vol. 506, pp. 250–303, jul 2003.

[60] J. Allison *et al.*, "Geant4 developments and applications," *IEEE Transactions on Nuclear Science*, vol. 53, pp. 270–278, feb 2006.

[61] "Geant4 Material Database." `http://geant4.web.cern.ch/geant4/workAreaUserDocKA/Backup/Docbook_UsersGuides_beta/ForApplicationDeveloper/html/apas08.html`.

[62] "NIST database of elements and isotope compositions." `http://physics.nist.gov/PhysRefData/Compositions/index.html`.

[63] Saint-Gobain Ceramics & Plastics, Inc, *Scintillating Optical Fibers.*

[64] A. Levin and C. Moisan, "A more physical approach to model the surface treatment of scintillation counters and its implementation into DETECT," vol. 2, pp. 702–706, IEEE, 1996.

[65] M. Janecek and W. W. Moses, "Simulating Scintillator Light Collection Using Measured Optical Reflectance," *IEEE Transactions on Nuclear Science*, vol. 57, pp. 964–970, jun 2010.

[66] M. Janecek and W. W. Moses, "Measuring Light Reflectance of BGO Crystal Surfaces," *IEEE Transactions on Nuclear Science*, vol. 55, pp. 2443–2449, oct 2008.

[67] M. Janecek and W. W. Moses, "Optical Reflectance Measurements for Commonly Used Reflectors," *IEEE Transactions on Nuclear Science*, vol. 55, pp. 2432–2437, aug 2008.

[68] HAMAMATSU PHOTONICS K.K., *Hamamatsu S12571-050P technical sheet.*

[69] NXP Semiconductors, *BFR520, NPN 9 GHz wideband transistor.*

[70] HAMAMATSU PHOTONICS K.K., *How does a silicon photomultiplier work?*

[71] S. Ritt, "Design and performance of the 6 GHz waveform digitizing chip DRS4," in *2008 IEEE Nuclear Science Symposium Conference Record*, pp. 1512–1515, IEEE, oct 2008.

[72] S. Ritt, Paul Scherrer Institute, *DRS4 Evaluation Board Users Manual.*

[73] A. Gadola, *Towards the First Imaging Atmospheric Cherenkov Telescope Camera with Continuous Signal Digitization.* PhD thesis, Universität Zürich, 2013.

[74] Laser system provided by the Prof. Osterwalder Group. University of Zurich.

[75] "piM1 beam line." `http://aea.web.psi.ch/beam2lines/beam_pim1.html`.

[76] R. Newman, "Visible Light from a Silicon p − n Junction," *Physical Review*, vol. 100, pp. 700–703, oct 1955.

[77] E. Garutti, "Silicon photomultipliers for high energy physics detectors," *Journal of Instrumentation*, vol. 6, pp. C10003–C10003, oct 2011.

[78] A. Papa and G. Rutar. Internal Discussion.

Curriculum Vitae

Personal Information

Name: Gredig, Roman

Date of birth: 18. Januar 1982

Hometown: Schwändi GL / Safien GR

Education

2011 – 2016	Dissertation in Physics, University of Zurich “Scintillating Fiber Detector for the Mu3e Experiment” Supervisor: Prof. Dr. Ulrich Straumann
2011	Master of Science in Physics UZH “Design and Development of an Automatic Mirror Segment Alignment System for the CTA Telescopes” Supervisor: Prof. Dr. Ulrich Straumann, Dr. Achim Vollhardt
2009 – 2011	Master Program Particle Physics UZH
2008 – 2009	Master Program Condensed Matter Physics UZH
2008	Bachelor of Science in Physics UZH “Wireless Short Range Network for the Active Mirror Control of the CTA Experiment” Supervisor: Prof. Dr. Ulrich Straumann, Dr. Achim Vollhardt
2005 – 2008	Bachelor Program Physics UZH
2002 – 2004	Bachelor Program Interdisciplinary Sciences ETHZ
2002	Maturität naturwissenschaftlich-mathematische Ausrichtung, Kantonsschule Schaffhausen